

AD-A254 021



RL-TR-92-47

Final Technical Report
May 1992



2

MULTIDIMENSIONAL DETERMINISTIC ELECTRON TRANSPORT CALCULATIONS

University of Arizona

W. L. Filippone, B. D. Ganapol, S. P. Monahan



APPROVED FOR PUBLIC RELEASE; DISTRIBUTION UNLIMITED.

This effort was funded totally by the Laboratory Director's fund.

92-22308



Rome Laboratory
Air Force Systems Command
Griffiss Air Force Base, NY 13441-5700

92 8 7 030

REPORT DOCUMENTATION PAGE

Form Approved
OMB No. 0704-0188

Public reporting burden for this collection of information is estimated to average 1 hour per response, including the time for reviewing instructions, searching existing data sources, gathering and maintaining the data needed, and completing and reviewing the collection of information. Send comments regarding this burden estimate or any other aspect of this collection of information, including suggestions for reducing this burden, to Washington Headquarters Services, Directorate for Information Operations and Reports, 1215 Jefferson Davis Highway, Suite 1204, Arlington, VA 22202-4302, and to the Office of Management and Budget, Paperwork Reduction Project (0704-0188), Washington, DC 20503.

1. AGENCY USE ONLY (Leave Blank)		2. REPORT DATE May 1992		3. REPORT TYPE AND DATES COVERED Final Nov 85 - Nov 88	
4. TITLE AND SUBTITLE MULTIDIMENSIONAL DETERMINISTIC ELECTRON TRANSPORT CALCULATIONS				5. FUNDING NUMBERS C - F30602-81-C-0185 PE - 61102F PR - LDFF TA - 10 WU - P6	
6. AUTHOR(S) W. L. Filippone, B. D. Ganapol, S. P. Monahan					
7. PERFORMING ORGANIZATION NAME(S) AND ADDRESS(ES) University of Arizona Department of Nuclear and Energy Engineering Tucson AZ 85721				8. PERFORMING ORGANIZATION REPORT NUMBER	
9. SPONSORING/MONITORING AGENCY NAME(S) AND ADDRESS(ES) Rome Laboratory (ERT) Griffiss AFB NY 13441-5700				10. SPONSORING/MONITORING AGENCY REPORT NUMBER RL-TR-92-47	
11. SUPPLEMENTARY NOTES Rome Laboratory Project Engineer: John C. Garth/ERT(617)377-2360 This effort was funded totally by the Laboratory Director's fund.					
12a. DISTRIBUTION/AVAILABILITY STATEMENT Approved for public release; distribution unlimited.				12b. DISTRIBUTION CODE	
13. ABSTRACT (Maximum 200 words) Fast and accurate techniques for determining electron fluxes and energy deposition profile in complex multidimensional microcircuits have been developed. The multidimensional Spencer-Lewis Transport equation is solved deterministically using several special numerical techniques. We begin with the derivation of the Spencer-Lewis equation. Then we discuss SMART scattering theory that enables us to replace the highly anisotropic electron scattering kernel by one that is more amenable to numerical treatment. Next, we describe several transport and diffusion theory solution algorithms. Finally, we present new analytical benchmarking methods that will prove useful in generating more comprehensive benchmarks.					
14. SUBJECT TERMS Electron transport; multidimensional transport; Spencer-Lewis equation				15. NUMBER OF PAGES 100	
				16. PRICE CODE	
17. SECURITY CLASSIFICATION OF REPORT UNCLASSIFIED	18. SECURITY CLASSIFICATION OF THIS PAGE UNCLASSIFIED	19. SECURITY CLASSIFICATION OF ABSTRACT UNCLASSIFIED	20. LIMITATION OF ABSTRACT U/L		

NON 70401-880-0000

Standard Form 298 (Rev. 2-89)
Prescribed by ANSI Std. Z39-18
298-102

TABLE OF CONTENTS

	Page
I Derivation of the Spencer-Lewis Equation	1
A. Homogeneous Media	3
B. Inhomogeneous Media	4
II Numerical Transport Methods	6
A. SMART Scattering Theory	6
1. The SMART Scattering Matrix	8
2. SMART First Collision Sources	15
B. Extension of the Streaming Ray (SR) Method to Two-Dimensional Homogeneous Media	18
C. The Two-Dimensional Multiregion S_N /Diamond Difference Algorithm	19
1. Theory	20
2. Results	22
3. Description of the SN2D Code	23
D. The Super Computer S_N (SCS $_N$) Method	25
III Numerical Diffusion Theory	30
A. 1-D Diffusion Theory	31
1. Point Spatial Finite Difference Scheme	32
2. Continuous Analytical Continuation	34
3. Path Length Discretization	35
4. Numerical Implementation and Test Case Result	37
5. Dose Calculation	40
B. 2-D Diffusion Theory	41
1. Two-Step Alternating Direction Implicit (ADI)	43
2. Iterative Methods	44
3. Test Results and Discussion	44
4. Transport/Diffusion Coupling	45
IV Development of Analytical Benchmark Methods	46
A. Benchmarks from Laplace Transform Inversion	46
B. Moments by Continuous Analytical Continuation	48
References	51

DTIC QUALITY INSPECTED 5

Accession For	
NTIS GRA&I	<input checked="" type="checkbox"/>
DTIC TAB	<input type="checkbox"/>
Unannounced	<input type="checkbox"/>
Justification	
By	
Distribution/	
Availability Codes	
Dist	Avail and/or Special
A-1	

MULTIDIMENSIONAL DETERMINISTIC ELECTRON TRANSPORT CALCULATIONS

W. L. Filippone, B. D. Ganapol, S. P. Monahan

Introduction

This report summarizes research carried out for the US Air Force Rome Air Development Center under contracts F 30602-81-C-0185 (P. R. No. S-6-7548) and E-21-669-S6 (P. R. No. S-7-7522). The object of this work was to develop fast and accurate techniques for determining electron fluxes and energy deposition profiles in complex multidimensional microcircuits, for use in radiation hardness studies. Our approach was to use deterministic solutions of the multidimensional Spencer-Lewis electron transport equation. To do this it was necessary to develop several special numerical techniques which we describe below.

We begin with the derivation of the Spencer-Lewis equation. Then we discuss SMART scattering theory that enables us to replace the highly anisotropic electron scattering kernel by one that is more amenable to numerical treatment. Next, we describe several transport and diffusion theory solution algorithms. Finally in Section IV we present several new analytical benchmarking methods that will prove useful in generating more comprehensive benchmarks.

I. Derivation of the Spencer-Lewis Equation

When continuous slowing down theory is valid, electron transport in homogeneous media is governed by the Spencer-Lewis equation,

$$\left[\frac{\partial}{\partial s} + \hat{\Omega} \cdot \vec{\nabla} + \sigma(s) \right] \Phi(r, s, \hat{\Omega}) = \int d\hat{\Omega}' \sigma(s, \hat{\Omega}' \rightarrow \hat{\Omega}) \Phi(r, s, \hat{\Omega}') + Q(r, s, \hat{\Omega}) \quad (1)$$

where

$\Phi(r, s, \hat{\Omega})$ = electron density (electrons per unit volume per unit solid angle) at position r , direction $\hat{\Omega}$ and path length s ,

$\alpha(s)$ = total (scattering) cross section, and

$Q(\vec{r}, s, \hat{\Omega})$ = electron source density (electrons per unit volume per unit path length per unit solid angle).

According to the continuous slowing down approximation (CSDA) there is a one-to-one correspondence between distance traveled and energy lost, and the path length s plays the role of an energy variable. We prefer the Spencer-Lewis equation to the multigroup Boltzman equation, because the latter is not particularly efficient at modeling electron energy loss. To obtain good results normally requires an exceedingly large number of groups^{1,2} (or other high resolution energy discretization technique³), while coarse path length mesh solutions of the Spencer-Lewis equation are normally sufficient,^{1,4} probably because the CSDA is built into the equation. Equation (1) was presented by Lewis⁵ in 1950 without proof, and its first practical solutions for the infinite medium case were obtained by Spencer⁶ in 1955 using the method of moments. We have derived⁷ Eq. (1) and a time-dependent generalized Spencer-Lewis equation valid for inhomogeneous media from the Boltzmann equation,

$$\left[\frac{\partial}{\partial t} + \vec{v} \cdot \vec{\nabla} + \alpha(\vec{r}, \vec{v}) v \right] N(\vec{r}, \vec{v}, t) = \int d^3v' \alpha(\vec{r}, \vec{v}' \rightarrow \vec{v}) v' N(\vec{r}, \vec{v}', t) + q(\vec{r}, \vec{v}, t) \quad (2)$$

where

N = electron density (electrons per unit volume per unit velocity) at position \vec{r} , velocity \vec{v} and time t ,

$\alpha(\vec{r}, v)$ = total (scattering) cross section

$\alpha(\vec{r}, \vec{v}' \rightarrow \vec{v})$ = differential scattering cross section

$q(\vec{r}, \vec{v}, t)$ = electron source density (electrons per unit volume per unit velocity per unit time)

A. Homogeneous Media

To derive Eq. (1) from Eq. (2) we assume that

1. Scattering changes direction but not energy, that is,

$$\sigma(\vec{v}' \rightarrow \vec{v}) = \delta(v-v') \sigma(v, \hat{\Omega}' \rightarrow \hat{\Omega})/v^2. \quad (3)$$

2. Energy loss is completely determined by the stopping power $|\frac{dE}{ds}|$.

3. The medium is homogeneous.

4. The fixed source is of the form

$$q(\vec{r}, \vec{v}, t) = Q(\vec{r}, \vec{v}) \delta[t - T(v)] \quad , \quad (4)$$

where $T(v)$ is the time it takes for an electron to slow down to speed v from some reference speed v_0 , such as the largest speed in the system. (This source form is needed so that at time t all electrons will have the same speed $V(t)$.)

It can then be shown that

$$N(\vec{r}, \vec{v}, t) = N(\vec{r}, \hat{\Omega}, t) \delta[v - V(t)]/v^2 \quad , \quad (5)$$

and Eq. (1) results from the substitution $\frac{1}{v} \frac{\partial}{\partial t} \rightarrow \frac{\partial}{\partial s}$ in Eq. (2) where

$$S(E) = \int_E^{E_0} \frac{dE}{\left| \frac{dE}{ds} \right|} \quad , \quad (6)$$

and $E_0 = E(v_0)$. The details of this derivation are given in Ref. 7.

If the source restriction [Eq. (4)] is relaxed, then the one-to-one correspondence between t and v and therefore between t and s is lost; however, Eq. (1) remains valid as is evident by the alternative derivation discussed below.

B. Inhomogeneous Media

To obtain a Spencer-Lewis type equation for inhomogeneous media we assume that

1. Energy loss and angular deflection are unconnected, that is that $\sigma(\vec{r}, \vec{v}' \rightarrow \vec{v})$ is of the form

$$\sigma(\vec{r}, \vec{v}' \rightarrow \vec{v}) = \delta(E' - E) \sigma_{\Omega}(\vec{r}, E, \hat{n}' \rightarrow \hat{n}) + \delta(\hat{n}' - \hat{n}) \sigma_E(\vec{r}, E' \rightarrow E) \quad (7)$$

2. An electron loses exactly the quantity of energy ΔE with each collision while preserving the correct stopping power so that

$$\sigma_E(\vec{r}, E' - E) = \frac{1}{\Delta E} \left| \frac{dE}{ds}(\vec{r}, E) \right| \delta(E' - E - \Delta E) \quad (8)$$

Inserting Eqs. (7) and (8) into Eq. (1), taking the limit $\Delta E \rightarrow 0$, and making the substitution

$$\frac{\partial}{\partial E} \rightarrow - \frac{1}{\left| \frac{dE}{ds}(\vec{r}, E) \right|} \frac{\partial}{\partial s}, \quad (9)$$

we obtain after considerable manipulation [See Ref. 7]

$$\begin{aligned} & \left[\frac{1}{v(\vec{r}, \vec{s})} \frac{\partial}{\partial t} + \hat{n} \cdot \vec{\nabla} + \sigma(\vec{r}, \vec{s}, \hat{n}) + \tilde{l}(\vec{r}, s) \frac{\partial}{\partial s} \right] \phi(\vec{r}, \vec{s}, \hat{n}, t) \\ &= \int d\tilde{n} \sigma(\vec{r}, \vec{s}, \hat{n}' \rightarrow \hat{n}) \phi(\vec{r}, \vec{s}, \hat{n}', t) + q(\vec{r}, \vec{s}, \hat{n}, t) \quad (10) \end{aligned}$$

where

$$\alpha(\vec{r}, \vec{s}, \hat{n}) = \alpha(\vec{r}, \vec{s}) - \frac{\hat{n} \cdot \vec{\nabla} \left| \frac{dE}{ds}(\vec{r}, E) \right|}{\left| \frac{dE}{ds}(\vec{r}, \vec{s}) \right|} \quad (11)$$

$$\tilde{I}(\vec{r}, \vec{s}) = 1 + \frac{\hat{n} \cdot \vec{\nabla} E(\vec{r}, \vec{s})}{\left| \frac{dE}{ds}(\vec{r}, \vec{s}) \right|} \quad (12)$$

Equation (10) is a generalization of the Spencer-Lewis equation valid for spatially varying stopping powers. If the medium is homogeneous then

$$\vec{s} \rightarrow s, \quad (13)$$

$$\alpha(\vec{r}, \vec{s}, \hat{n}) \rightarrow \alpha(s) \quad (14)$$

$$\tilde{I}(\vec{r}, \vec{s}) \rightarrow 1 \quad (15)$$

and Eq. (10) becomes

$$\left[\frac{1}{v} \frac{\partial}{\partial t} + \hat{n} \cdot \vec{\nabla} + \alpha(s) + \frac{\partial}{\partial s} \right] \phi(\vec{r}, s, \hat{n}, t) = \int d\hat{n}' \alpha(s, \hat{n}' \rightarrow \hat{n}) \phi(\vec{r}, s, \hat{n}', t) q(\vec{r}, s, \hat{n}, t) \quad (16)$$

Equation (16) is not simply the time-dependent form of Eq. (1). The variable Φ in the later equation is a number density (electrons/cm³) while ϕ in the former equation is a flux (cm traveled/cm²/second). Integrating Eq. (16) over all time and putting

$$\Phi(r, s, \hat{n}) = \int_0^\infty dt \phi(\vec{r}, s, \hat{n}, t) \quad (17)$$

and

$$Q(\vec{r}, s, \hat{n}) = \int_0^{\infty} dt \, q(\vec{r}, s, \hat{n}, t) \quad (18)$$

we obtain Eq. (1). This derivation of Eq. (1) does not require the source restriction specified by Eq. (4).

An independent verification⁷ of Eq. (10) was obtained for the one-dimensional case using particle balance considerations.

II. Numerical Transport Methods

A. SMART Scattering Theory

Electrons interact via long-range electric forces, and therefore their cross sections tend to be enormous and extremely forward peaked as compared to those of neutral particles. As a consequence, electron transport is characterized by a large number of minute deflections in the velocities of the electrons. This virtually rules out the possibility of direct modeling either through Monte Carlo or discrete ordinates techniques.

Most Monte Carlo codes use condensed histories^{8,9} because the large value of the scattering cross section makes it impractical to follow each individual scattering event for a sufficient number of histories.

The large scattering cross sections also cause trouble for discrete ordinates codes by making the spectral radius (without acceleration) for the source iteration nearly equal to unity. Furthermore, the anisotropy of the scattering kernel can require a large number of discrete ordinates for an adequate numerical treatment. Because of these problems, discrete ordinates solvers normally replace the true transport model by one that is more easily simulated. This is done through the use of effective cross sections. These sections have three important properties that make them suitable for numerical calculations:

- They are much smaller than the true cross sections they replace.

- They are much less anisotropic.
- They yield good results in discrete ordinates codes.

With effective cross sections a few large angle deflections are used to model the combined effect of many small angle deflections.

Effective scattering matrices are most often generated using Fokker-Planck^{10,11} methods or the extended transport (delta function) correction.^{11,13} The major drawback with these techniques is that they lead to nonpositive and therefore nonphysical scattering matrices.

We describe a special type of effective scattering matrix that we refer to as SMART (simulation of many accumulative Rutherford trajectories). The acronym is somewhat appropriate (although not in the precise artificial intelligence sense) because the matrix elements are defined such that they cancel errors due to angular discretization. It is this property that enables electron discrete ordinates calculations to be performed with relatively few (typically 12) discrete directions. It is also possible to refine the definition of these scattering matrices such that they cancel path length in addition to angular discretization errors. We refer to such scattering matrices as very SMART.

The theory of SMART scattering matrices is based on the conjecture that a scattering kernel should be independent of the problem geometry. In particular, a scattering matrix that performs well in an infinite medium should also perform well in a finite medium. Using the Goudsmit-Saunderson¹⁴ theory of multiple scattering, exact infinite medium solutions are easily obtained. Working backward from such results, we are able to deduce a suitable scattering matrix for the discrete ordinates equation. In contrast to the Fokker-Planck kernel and the extended transport corrected kernel (which is SMART with Gauss quadrature sets but not positive), positive SMART scattering matrices are easily generated.

Positive scattering matrices have three important advantages:

- They guarantee positive solutions when used in conjunction with positive spatial differencing schemes.

-They enable the use of negative flux fixups. (Such fixups are justified when negative angular fluxes result from spatial differencing errors, but not when they result from negative scattering matrix elements.)

-They can be used in single collision Monte Carlo codes that require positive cross sections.

There are infinitely many ways to discretize the electron transport equation, an infinite subset of which leads to the discrete ordinates equations. Corresponding to each discretization scheme is a different SMART scattering matrix. In fact, if Gauss quadrature points are used, then one of these schemes leads to the extended transport corrected scattering matrix. Fortunately, it is easy to find discretization methods that lead to discrete ordinates equations and to positive SMART scattering matrices as well.

1. The SMART Scattering Matrix

To illustrate the discretization possibilities, we begin with a weighted residual derivation of the S_N equations. (This section is condensed from Ref. 15.)

The Weighted Residual Derivation of the S_N Equations

Let the flux in Eq. (1) be approximated by

$$\phi(\vec{r}, s, \hat{\Omega}) \approx \phi_T(\vec{r}, s, \hat{\Omega}) = \sum_{m=1}^M \phi_T^m(\vec{r}, s) B^m(\hat{\Omega}) \quad , \quad (19)$$

where the B^m are a set of M basis functions. The residual associated with ϕ_T is defined as

$$\begin{aligned} R(\vec{r}, s, \hat{\Omega}) &= \left[\frac{\partial}{\partial s} + \hat{\Omega} \cdot \nabla + \sigma(s) \right] \phi_T(\vec{r}, s, \hat{\Omega}) \\ &\quad - \int d\Omega' \sigma(s, \hat{\Omega}' \rightarrow \hat{\Omega}) \phi_T(\vec{r}, s, \hat{\Omega}') \\ &\quad - Q(\vec{r}, s, \hat{\Omega}) \quad . \end{aligned} \quad (20)$$

Forcing the residual to be orthogonal to a set of test functions, $(T^m(\hat{\Omega}); m = 1, 2, \dots, M)$, that satisfy the conditions

$$\int T^m(\hat{\Omega}) * B^{m'}(\hat{\Omega}) d\Omega = \delta_{mm'} , \quad (21)$$

and

$$\int T^m(\hat{\Omega}) * \hat{\Omega} B^{m'}(\hat{\Omega}) d\Omega = \tilde{\Omega}^m \delta_{mm'} , \quad (22)$$

we obtain

$$\begin{aligned} & \left(\frac{\partial}{\partial s} + \tilde{\Omega}^m \cdot \nabla \right) \phi_T^m(\vec{r}, s) \\ &= \sum_{m'=1}^M S_{mm'} \phi_T^{m'}(\vec{r}, s) \\ & \quad + Q^m(\vec{r}, s) , \quad m = 1, 2, \dots, M , \end{aligned} \quad (23)$$

where

$$S_{mm'} = S'_{mm'} - \sigma \delta_{mm'} , \quad (24)$$

$$S'_{mm'} = \iint T^m(\hat{\Omega}) * \sigma(s, \hat{\Omega} \rightarrow \hat{\Omega}') B^{m'}(\hat{\Omega}') d\Omega' d\Omega , \quad (25)$$

$$Q^m(r, s) = \int T^m(\hat{\Omega}) * Q(r, s, \hat{\Omega}) d\Omega , \quad (26)$$

and from Eq. (22),

$$\begin{aligned} \tilde{\Omega}^m &= \int T^m(\hat{\Omega}) * \hat{\Omega} B^m(\hat{\Omega}) d\Omega \\ &\approx \hat{\Omega}^m , \end{aligned} \quad (27)$$

where $\hat{\Omega}^m$ is the m 'th discrete direction. The $S'_{mm'}$ are the elements of the conventional scattering matrix S' . The matrix S defined by Eq. (24) has removal as well as scatter included in its definition. It is referred to as the net conventional scattering matrix, and is normally approximated as

$$S_{mm'} \approx \sigma(s, \hat{\Omega}^{m'} \rightarrow \hat{\Omega}^m) \omega^m - \sigma \delta_{mm'} \quad (28)$$

where

$$\omega^m = \int B^m(\hat{\Omega}) d\Omega \quad (29)$$

Because of the extreme anisotropy of $\sigma(s, \hat{\Omega}' \rightarrow \hat{\Omega})$, the major contribution to the integral of Eq. (1) comes from values of $\hat{\Omega}' \approx \hat{\Omega}$. Unless a very large value of M is used, this contribution is normally missed with conventional scattering matrices. For this reason the error, defined as

$$\epsilon^m(\vec{r}, s) = \phi_T^m(\vec{r}, s) - \phi^m(\vec{r}, s) \quad (30)$$

can be quite large. To reduce this error, we replace S with a SMART net scattering matrix \tilde{S} , which is designed to give good results when a coarse angular mesh is used. The matrix \tilde{S} is obtained by forcing $\epsilon^m = 0$ for a set of problems for which analytic solutions are available.

The Goudsmit-Saunderson Matrix

To obtain benchmark problems that are amenable to exact analytical solution, we consider an infinite source-free medium with an initial ($s = 0$) distribution $\phi(0, \hat{\Omega})$ that is independent of position \vec{r} . For this case, Eq. (1) reduces to

$$\left[\frac{\partial}{\partial s} + \sigma(s) \right] \phi(s, \hat{\Omega}) = \int \sigma(s, \hat{\Omega}' \rightarrow \hat{\Omega}) \phi(s, \hat{\Omega}') d\Omega' \quad (31)$$

We are interested in equating the discrete ordinates and exact solutions for identical initial conditions. As seen from Eq. (19), the initial condition for the discrete ordinates equations must be of the form

$$\phi_T(0, \hat{\Omega}) = \sum_{m=1}^M \phi_T^m(0) B^m(\hat{\Omega}) \quad . \quad (32)$$

With an initial distribution of this form, the exact $\phi^m(s)$ are given,¹⁵ in matrix form by

$$\vec{\phi}(s) = G(0 \rightarrow s) \vec{\phi}_T(0) \quad , \quad (33)$$

where the components of $\vec{\phi}$ and $\vec{\phi}_T$ are ϕ^m and ϕ_T^m , respectively. The elements of the Goudsmit-Saunderson matrix G are given by

$$G(s_0 \rightarrow s)_{mm'} = \iint T^m(\Omega) g(s_0 \rightarrow s, \hat{\Omega} \cdot \hat{\Omega}') B^{m'}(\hat{\Omega}') d\Omega d\Omega' \quad , \quad (34)$$

where¹⁴

$$g(s_0 \rightarrow s, \hat{\Omega} \cdot \hat{\Omega}') = \sum_{\ell=0}^{\infty} \frac{2\ell+1}{4\pi} \exp \left\{ - \int_{s_0}^s [\sigma_0(s') - \sigma_{\ell}(s')] ds' \right\} P_{\ell}(\hat{\Omega} \cdot \hat{\Omega}') \quad , \quad (35)$$

and P_{ℓ} is the ℓ th Legendre polynomial. We emphasize here that Eq. (33) represents the exact (continuous angle) solution for any source that can be expressed by Eq. (32). Although spatial effects have been eliminated, the effects of multiple scattering are present and therefore Eq. (33) should constitute a good benchmark for testing discrete scattering kernels.

The Diamond-Difference SMART Scattering Matrix

Our two-dimensional S_N code described below uses diamond differencing in both space and path length; however, only the numerical treatment of the path length variable affects the definition of the scattering matrix. With diamond differencing and a piecewise constant scattering matrix, it is easy to show¹⁵ that the S_N solution to Eq. (31) is

$$\vec{\phi}_T^{DD}(s_{i+1/2}) = \left[1 - \frac{\Delta s_i}{2} \tilde{S}_i \right]^{-1} \left[1 + \frac{\Delta s_i}{2} \tilde{S}_i \right] \vec{\phi}_T(s_{i-1/2}) ,$$

where the $s_{i\pm 1/2}$ are the edges, Δs_i the size, and \tilde{S}_i the SMART scattering matrix for the i 'th path length step.

To define the \tilde{S}_i we force Eq. (36) to agree with the exact solution [Eq. (33)] at each value of $s_{i+1/2}$. It is shown in Ref. 15 that the required scattering matrix is

$$\begin{aligned} \tilde{S}_i = & \frac{2}{\Delta s_i} [I + G(0 \rightarrow s_{i+1/2}) G(0 \rightarrow s_{i-1/2})^{-1}]^{-1} \\ & \times [G(0 \rightarrow s_{i+1/2}) G(0 \rightarrow s_{i-1/2})^{-1} - I] . \end{aligned} \quad (37)$$

This scattering matrix cancels errors due to

- angular discretization
- diamond differencing in s
- the piecewise constant (in s) approximation.

An example of a diamond difference SMART scattering matrix is given in Table III of Ref. 15.

Positivity

We demonstrate in Ref. 15 that the \tilde{S}'_i will be positive provided that the Δs_i are sufficiently small, and the basis functions [the $B^m(\hat{\Omega})$] are chosen positive.

Although the delta function corrected scattering matrix is SMART if Gauss quadrature points are used (this is only possible in one-dimensional geometries) it is not positive. (Compare Table V with Table III of Ref. 15.) As shown in Ref. 15, this is due to the fact that the basis functions that yield the delta function corrected scattering matrix are the Lagrange interpolation polynomials, which are not positive functions. With positive SMART scattering matrices problems of negative fluxes do not occur. See Fig. 1 of Ref. 15.

SMART scattering matrices have produced excellent results in one-dimensional single collision Monte Carlo¹⁶ calculations (see Fig. 2 of Ref. 15) in two-dimensional SR calculations (see Table I of Ref. 17) and in two-dimensional S_N calculations (See Figs. 3 and 4 of Ref. 15 and Fig. 2 of Ref. 18).

It appears that SMART scattering theory can be used to eliminate or reduce several of the classic problems associated with electron transport, namely,

- miniscule mean-free-paths that imply

- a. slowly converging source iterations in S_N and SR codes
- b. many collisions per history in Monte Carlo codes
- c. relatively large ratios of cell-collided to cell-uncollided fluxes, which reduces the accuracy of SR calculations⁴

- large angular discretization errors in S_N and SR codes

- nonpositive scattering matrices that

- a. cannot be used in Monte Carlo codes
- b. should not be used in S_N codes with negative flux fixups

- the relatively minor problem of path length discretization errors.

SMART scattering matrices have performed well in SR, S_N , and single collision Monte Carlo computer codes. They appear to be an attractive alternative to Fokker-Planck and extended transport correction techniques for S_N and SR calculations and to the condensed history approach for Monte Carlo calculations.

Fokker-Planck methods give a good representation of narrow angle scattering but are inappropriate for wide angle collisions.

Extended transport corrected cross sections can simulate both narrow and wide angle collisions, and are in fact SMART if Gauss quadrature points are used. However, they are nonpositive.

With the condensed history approach, direction change is determined by sampling the Goudsmit-Saunders distribution. Since this distribution is the solution of the space-independent Spencer-Lewis equation, it is not valid near material interfaces and special techniques must be used.⁸ As speculated above, the validity of a SMART scattering matrix should not depend on the proximity of a boundary. If this is indeed true, then the SMART scattering matrices should prove useful in Monte Carlo codes at least in the vicinity of interfaces. To date, our test problems have involved only media with vacuum boundaries. To obtain a more stringent test of SMART scattering theory, calculations with several closely spaced material interfaces will soon be carried out.

It may appear that the method for generating SMART scattering matrices is analogous to the flux-weighting procedure used to determine effective neutron cross sections. Indeed, both techniques use infinite media solutions to determine appropriate cross sections. However, the SMART scattering matrix is by no means an angular flux-weighted average of the true scattering kernel. In fact, the total cross section is much smaller and the average deflection per collision much larger than those for the true scattering kernel.

SMART scattering theory appears to have an important advantage over flux-weighting techniques. Flux-weighted cross sections are valid only for one particular spectrum, whereas the SMART scattering matrix gives exact solutions for any arbitrary angular flux (provided it is spatially independent.) Thus, flux-weighted cross sections are reliable only if the spectrum in the region to be analyzed resembles that used to generate the cross sections. SMART scattering matrices should be more versatile. Our current thinking is that these matrices will be nearly equivalent to the true scattering kernels in most problem geometries, but exactly equivalent only in infinite media. Although we cannot give a formal proof, our reasons for this assertion are as follows:

-The SMART scattering matrix is not tied to a particular angular flux distribution.

-There is considerable numerical evidence that the SMART scattering matrices work well in finite media.

-The physical model corresponding to SMART scattering theory (few relatively wide angle collisions) seems to be a reasonable equivalent to the true situation (many small angle collisions).

-Certainly one can imagine pathological geometries in which trajectories with a large number of small angle collisions could not be simulated by trajectories with a lesser number of large deflections. Thus, it is doubtful in our opinion that an exact equivalence can be demonstrated for the finite medium case.

We have observed¹⁵ that the SMART and conventional scattering matrices are in close agreement for those matrix elements that represent wide angle scattering. However, for narrow deflections the elements of \tilde{S} exceed those of S . The augmented values of these elements in \tilde{S} compensate for the large number of very narrow deflections that are too small for direct modeling on the S_N quadrature set.

The conventional scattering matrix fails in electron transport because it misses the accumulative effect of these narrow deflections.

2. SMART First Collision Sources

The material in this section is taken from Ref. 19. The use of analytic first collision sources can greatly improve the accuracy of neutral particle S_N calculations. For electrons, because of the strong anisotropy of the electron scattering kernel, many collisions are required before the flux from a beam source is smooth enough to lend itself to practical numerical treatment. Thus the use of a conventional analytic first collision source is of little value.

With SMART scattering theory¹⁵ as described above, the true electron scattering law is replaced by an equivalent one that involves many times fewer collisions but larger angular

deflections per collision. With such a scattering law, the electron transport emulates that of neutral particles. Hence, application of an analytic first collision source should be effective. However, SMART scattering cross sections are defined in terms of a scattering matrix and thus only apply for scatter from one quadrature direction to another.

We have extended the theory to include scatter from (but not to) an arbitrary beam direction. This entails the generation of one additional column \vec{S}^b of the SMART scattering matrix. The m 'th element S_m^b of the vector \vec{S}^b is a SMART cross section for transfer from the beam to direction $\hat{\Omega}^m$.

The S_m^b are determined by a procedure similar to that used to determine the SMART scattering matrix. We require that the S_N method with an analytic first collision source produce the exact solution to an appropriate benchmark problem.

Again we choose Eq. (31) to define our benchmark problem and begin with the discrete ordinates solution. We assume that the SMART scattering matrix \tilde{S} has already been determined. Then, for the first path length step it is easy to show¹⁹ that the S_N expression for the multiply scattered flux is:

$$\vec{\phi}^c(\Delta s) = \left[I - \frac{\Delta s}{2} \tilde{S} \right]^{-1} \frac{1 - \exp(-\sigma_b \Delta s)}{\sigma_b} \vec{S}^b \quad (38)$$

where

$$\sigma_b = \sum_{m=1}^M \omega_m S_m^b \quad (39)$$

ω_m = weight for direction, $\hat{\Omega}^m$

$\vec{\phi}^c(\Delta s)$ = vector whose m 'th component is the multiply scattered flux at $\hat{\Omega}^m$ and $s = \Delta s$. Let the exact (continuous angle) expression for the multiply scattered flux be denoted by $\vec{g}(\Delta s)$. Then, the exact and the S_N solution agree provided that we put

$$\vec{S}^b = \frac{\sigma_b}{1 - \exp(-\sigma_b \Delta s)} \left(I - \frac{\Delta s}{2} \tilde{S} \right) \vec{g}^c(\Delta s) \quad , \quad (40)$$

and $\vec{g}^c(\Delta s)$ must satisfy the normalization¹⁹

$$\sum_{m=1}^m \omega_m g_m^c(\Delta s) = 1 - \exp(-\sigma_b \Delta s) \quad . \quad (41)$$

These results require careful interpretation. Equations (40) and (41) are insufficient to determine both \vec{S}^b and σ_b because the maximum component(s) of $\vec{g}^c(\Delta s)$ is (are) not defined. Here $\vec{g}^c(\Delta s)$ represents the multiscattered rather than the total flux. Ordinarily, these two fluxes differ only by a delta function of negligible strength [$\exp(-\sigma \Delta s)$, where σ is the true cross section] centered at the beam direction. However, as explained above, it is necessary that $\sigma_b \ll \sigma$. This amounts to broadening the definition of the uncollided beam to include some narrowly scattered electrons, thereby reducing the maximum element(s) of $\vec{g}^c(\Delta s)$.

The amount of broadening is determined by σ_b , which remains a free parameter. Once σ_b is chosen, the maximum element(s) of $\vec{g}^c(\Delta s)$ can be determined from normalization Eq. (41) and \vec{S}^b from Eq. (40). This choice of \vec{S}^b guarantees that the S_N method will reproduce the exact benchmark result, that is, the normalized $\vec{g}^c(\Delta s)$.

Unlike σ_b , the attenuation factors for travel along any of the quadrature directions are uniquely determined by SMART scattering theory,¹⁸ and they all have comparable values. Our S_N code selects one of these (corresponding to $m = k$, for example) for σ_b . Because of this choice and the corresponding broadened meaning of the uncollided flux, the beam is not modeled by a monodirectional ray; instead it is modeled by a cluster of rays with an angular spread commensurate with ω_k .

Figure 1a of Ref. 19 shows the result of the application of the S_N method with the SMART first collision source to a two-dimensional problem. A beam of 200-KeV electrons is assumed incident on a 0.01×0.02 g/cm² aluminum slab. The beam obliquity (in the x-y plane) is 45 deg,

and the point of incidence is located at $x = 0$, $y = 0.01$ (as shown on the inset). The rectangular slab is divided into 50 square zones (0.002×0.002), and the histogram displays the energy (in kilo-electron-volts) deposited in each zone as obtained using an S_4 calculation. Figure 1b of Ref. 19 shows the result of the application of the ACCEPT (Ref. 20) Monte Carlo code to the same problem. The two methods agree well. The S_4 calculation consumed $\frac{1}{30}$ 'th of the computer time required by the Monte Carlo code (100,000 case histories). It is anticipated that better agreement would be achieved with a higher order calculation such as S_8 , which would run approximately three to four times slower than the S_4 .

B Extension of the Streaming Ray (SR) Method To Two-Dimensional Homogeneous Media

This section is condensed from Ref. 17. The method of streaming rays (SRs) has been shown previously⁴ to be an effective algorithm for one-dimensional electron transport studies. The Spencer-Lewis equation⁵⁻⁷ is solved for the electron distribution in direction μ , position x , and path length s , and the continuous slowing down approximation is used to relate energy loss to distance traveled, so that path-length-dependent cross sections can be defined. The SR algorithm for electron transport calculations is advantageous because it facilitates modeling of the continuous energy loss.

We have extended the SR method to two spatial dimensions (three phase-space dimensions, x , y , and s).

In contrast to its one-dimensional predecessor,⁴ the SR2D code accommodates nonuniform cell dimensions in x and y and allows for arbitrary discrete ordinates quadrature sets (S_2 , S_4 , S_6 , S_8 , S_{12} , or S_{16}). Families of streaming rays originate in the $x = 0$ plane with a uniform spacing and overlay the three-dimensional Eulerian grid in x,y,s phase space. Each ray is defined by its direction m and the coordinates of its origination point in the y,s plane. With this arrangement and with Δs , the path length step equal to an integer multiple of DS , the spacing between streaming ray

origination points, each slab of thickness Δs has an identical pattern of interlacing streaming rays and path lengths need to be computed only once.

The SR2D code uses SMART cross sections¹⁸ that significantly reduce angular discretization errors. This allows the highly anisotropic electron scattering to be modeled with relatively few discrete directions.

The code was used to calculate the energy deposition profile for an isotropic point source at the periphery of a two-dimensional aluminum medium with dimensions 0.01 g/cm² thick \times 0.02 g/cm² wide. The computational grid was 5 \times 10 uniform cells, respectively. The path-length increment was 0.002 g/cm² with 25 path-length increments chosen. An S_8 quadrature set was used. The isotropic point source was normalized to one incident particle with an energy of 200 KeV.

To validate the SR2D results, the test problem was also solved using the electron/photon Monte Carlo code TIGER (Ref. 9). The total energy deposited in the medium and peak cell energies was selected to facilitate the comparison. Results for SR2D and TIGER are provided in Table I of Ref. 17. For this problem, the calculated values of the total energy deposited in the aluminum were within 1%, but peak cell energies varied by 4%. The largest relative error was <30%, and this occurred where numerical values were small, well away from the area of peak energy deposition. The TIGER results came from an evaluation of 50,000 case histories and were within $\pm 9\%$. Other problems have been compared, particularly a monodirectional point source, with equally good results.

C. The Two-Dimensional Multiregion S_N /Diamond Difference Algorithm

Although the SR2D code gives good results, the algorithm would be significantly more complicated for multiregion problems. We therefore decided to use initially the somewhat less complicated S_N method for our multiregion code.

1. Theory

Extending from homogeneous to multiregions introduces a complication. In the Spencer-Lewis equation s is used to specify the electron's energy. For homogeneous media, the CSDA implies a one-to-one correspondence between E and s . However, with multiregion problems this one-to-one correspondence is lost (since the stopping power is spatially dependent) and s no longer determines E .

Therefore, we redefine s to mean the path length that would be required to reach energy E in an infinite homogeneous medium of the composition occurring at the electron's location. That is, we let

$$s = \int_0^E \frac{dE'}{\left| \frac{dE}{ds}(E') \right|_r}, \quad (42)$$

where $\left| \frac{dE}{ds}(E) \right|_r$ is the stopping power in region r . Thus s is not the true path length for an electron that has traveled in more than one region.

With this definition, E is determined by s and the electrons location. However, the electron flux at a particular value of s is no longer continuous across material interfaces. Thus, the S_N equations cannot be formulated in the conventional manner. However, the flux integrated over a path length step will be continuous provided that the path length steps represent the same energy intervals in each region. By substituting integrated quantities for cell center fluxes and some of the edge fluxes we are able to use the standard S_N algorithm.

We consider first the standard discrete ordinates from ^{18,20} of Eq. (1) in x - y - s geometry, for mesh cell $\Delta s_i^r \Delta x_j \Delta y_k$ in region r .

$$\begin{aligned} & \frac{1}{\Delta s_i^r} \left(\phi_{i+\frac{1}{2},jk}^m - \phi_{i-\frac{1}{2},jk}^m \right) + \frac{\Omega x}{\Delta x_j} \left(\phi_{ij+\frac{1}{2},k}^m - \phi_{ij-\frac{1}{2},k}^m \right) \\ & + \frac{\Omega y}{\Delta y_k} \left(\phi_{ijk+\frac{1}{2}}^m - \phi_{ijk-\frac{1}{2}}^m \right) = \sum_{m'=1}^M \tilde{S}_{imm'}^r \phi_{ijk}^{m'} + Q_{ijk}^m \end{aligned} \quad (43)$$

In this equation whole indices i,j,k are used for quantities that have been averaged over Δs_i^r , Δx_j and Δy_k respectively, while half indices represent cell edge values. (The need for the superscript r on Δs_i^r is explained below). To better model the extreme anisotropy of the scattering kernel the $\tilde{S}_{imm'}^r$ are determined using SMART scattering theory.

The S_N algorithm cannot be applied directly to Eq. (43) because the edge fluxes $\phi_{ij\pm\frac{1}{2},k}^m$ and $\phi_{ijk\pm\frac{1}{2}}^m$ are not continuous at material interfaces. However, these same edge fluxes when multiplied by Δs_i^r are continuous provided that the Δs_i^r define the same energy interval in each region, that is, provided that

$$\Delta s_i^r = \int_{E_{i-\frac{1}{2}}}^{E_{i+\frac{1}{2}}} \frac{dE'}{\left| \frac{dE}{ds}(E') \right|_r} \quad (44)$$

where the energies $E_{i\pm\frac{1}{2}}$ defining the edges of the i 'th path length step are identical in each material region. Multiplying Eq. (43) by Δs_i^r we obtain

$$\begin{aligned} \phi_{i+\frac{1}{2}jk}^m - \phi_{i-\frac{1}{2}jk}^m + \frac{\Omega_x}{\Delta x_j} \left(\bar{\phi}_{ij+\frac{1}{2}k}^m - \bar{\phi}_{ij-\frac{1}{2}k}^m \right) \\ + \frac{\Omega_y}{\Delta y_k} \left(\bar{\phi}_{ijk+\frac{1}{2}}^m - \bar{\phi}_{ijk-\frac{1}{2}}^m \right) = \sum_{m'=1}^M \tilde{S}_{imm'}^r \bar{\phi}_{ijk}^m + \bar{Q}_{ijk}^m \end{aligned} \quad (45)$$

where the bar (-) is used to indicate quantities that have been multiplied by Δs_i^r . All edge fluxes in Eq. (45) are continuous, and except for the numerical treatment of the scattering term, the equation is exact. However there are four unknowns, the cell center flux and the three cell exit fluxes. In order to obtain a solvable system of equations we use the diamond difference approximation,²¹ which here takes the form

$$\begin{aligned} 2\bar{\phi}_{ijk} &= \left(\phi_{i+\frac{1}{2}jk} + \phi_{i-\frac{1}{2}jk} \right) \Delta s_i^r \\ &= \bar{\phi}_{ij+\frac{1}{2}k} + \bar{\phi}_{ij-\frac{1}{2}k} \\ &= \bar{\phi}_{ijk+\frac{1}{2}} + \bar{\phi}_{ijk-\frac{1}{2}} \end{aligned} \quad (46)$$

Except for the appearance of Δs_i^r in Eq. (46) and its absence from Eq. (45), these last two equations are identical in form to the conventional S_N /Diamond Difference equations.^{18,20} Making a minor adjustment for Δs_i^r we solve these equations using the usual S_N /Diamond Difference algorithm.

2. Results

We have performed many two-dimensional multiregion problems. The results are qualitatively correct and the calculations conserve particles to at least four significant figures. This is encouraging, however we have not yet compared the multiregion results to accurate benchmark solutions.

The code has been verified with several single region problems. Figures 3 and 4 and Table VII of Ref. 15 show a comparison of S_N and Monte Carlo calculations of the energy deposition profile due to a 200 KeV isotropic point source of electrons incident on a two-dimensional aluminum slab. Similar comparisons for both isotropic and monodirectional beam sources are shown in Figs. 1 and 2 of Ref. 18. The two methods are in very good agreement.

3. Description of the SN2D Code

a. Input

The user may select

- Number of regions (1 to 15)
- Number of elements per region (1 to 10)
- Number of energy/path length mesh cells
- Number of x-mesh cells
- Number of y-mesh cells
- S_N number (2, 4, 6, 8, 12 or 16)
- Input in centimeters or micrometers
- Maximum number of source iterations per path length step
- Reduced or full printout option
- Type of source
 1. Spatially distributed isotropic
 2. Spatially distributed monodirectional along one of the quadrature directions
 3. Point source at user specified location in user specified direction
- Energy of source particles
- Negative flux fix-up option
 1. No fix-up

2. Negative flux fix-up
3. Negative flux fix-up and reduce Δs until scattering matrix is positive
4. Negative flux and negative source fix-up
5. Start with 2 and convert to 1 if the scattering matrix goes negative at some path length step (we recommend option 3)

-Beam source representation

1. Monodirection
2. Cluster of four nearly monodirectional beams. (This better represents the slight spreading of a SMART "uncollided" beam as explained in Section II.A.2)

-Cross section option

1. Screened Rutherford
2. Riley (not fully debugged)

-Maximum order of Legendre cross section expansion for determining the Goudsmit-Saunderson matrix. (The suggested value is 200)

-The energy mesh intervals (arbitrary spacing)

-The x-mesh intervals (arbitrary spacing)

-The y-mesh intervals (arbitrary spacing)

b. Output

The output from the code includes

-Angular fluxes for each cell

-The spatially integrated angular flux in each energy step

-The total flux for each mesh cell

-The total leakage currents (electrons per second) from each surface

-The energy deposited in each spacial mesh cell.

D. The Super Computer S_N (SCS $_N$) Method

The material in this section is taken from Ref. 21. When developed in the '50s and '60s, the discrete ordinates method²⁰ was tailored for optimum efficiency on the computers of the day. Computation speeds and the available memory of those first computers were extremely poor by today's standards. Nevertheless, the S_N algorithm was and continues to be the method of choice for many transport problems. However, S_N calculations have been plagued by two serious problems, numerical diffusion and ray effects; the first arises from spatial discretization, and can be quite severe²³ near flux discontinuities; the second results from angular discretization and is very pronounced for low scattering media. Although the SR method^{4,23} eliminates the former problem it does not eliminate the latter. We have developed a new discrete ordinates method specifically designed for today's large memory, vector and/or parallel processing computers that sharply reduces numerical diffusion and eliminates observable ray effects.

The method has been tested with excellent results on one-dimension homogeneous slab problems. For these problems the Spencer Lewis equation [Eq. (1)] for discrete direction μ^m becomes

$$L_m \phi(x, \mu^m, s) = \sum_{m'=1}^M S_{mm'} \phi(x, \mu^{m'}, s) + Q(x, \mu^m, s) \quad , \quad (47)$$

where

$$L_m = \frac{\partial}{\partial s} + \mu^m \frac{\partial}{\partial x} + \sigma \quad (48)$$

Discretizing path length and space yields the following equation that is solvable by the standard source iteration method,

$$\vec{\phi}_m^{(p+1)} = (L_m)^{-1} \vec{q}_m^{(p)} \quad , \quad (49)$$

where

$$\vec{q}_m^{(p)} = \sum_{m'=1}^m S_{mm'} \vec{\phi}_{m'}^{(p)} + \vec{q}_m \quad , \quad (50)$$

$\vec{\phi}_m^{(p)}$ and \vec{Q}_m^p have components $\phi_m^{(p)}(x_j, \mu^m, s_i)$ and $Q(x_j, \mu^m, s_i)$, j and i are the x and s discretization indices, and L_m is now the matrix representation of the original operator. It is evident from Eq. (3) that each matrix element of $(L_m)^{-1}$ represents the uncollided flux in a particular cell due to a monodirectional unit source in another. Therefore $(L_m)^{-1}$ is a very large and sparse matrix. The conventional S_N algorithm enables Eq. (49) to be implemented without explicitly determining the matrix elements of $(L_m)^{-1}$, or explicitly executing the implied multiplications by zero. This is an enormous advantage for low memory scalar computers, but it is also the major source of the numerical errors. Although the matrix elements corresponding to adjacent cells are determined accurately (implicitly), those corresponding to distant cells are not, because they are obtained (implicitly) through the repeated application of a spatial differencing approximations. Some elements which should be zero turn out positive (or even negative if no fix-up is used) resulting in numerical diffusion. Matrix elements for cells lying along a discrete direction tend to be over-estimated causing ray effects. Since scattering tends to reduce the magnitude of the matrix elements for the distant cells it also reduces the severity of these two errors.

The fundamental ideas of our method are simple:

- Calculate the elements of $(L_m)^{-1}$ explicitly and accurately.
- Implement Eq. (49) in matrix form.

Item 2 above allows us to take advantage of vector and or parallel processing and thereby compensate for the many multiplications by zero.

Since $(L_m)^{-1}$ represents an operator for uncollided transport, its elements can be calculated to any degree of accuracy. However, this would require the evaluation of tedious integrals, and instead we have adopted the following simple scheme.

The first step is to calculate the uncollided flux contribution from a monodirectional unit source in cell i' , j' to the target path length cell i by:

$$\phi_T^0 = \frac{1}{\sigma_1} - \frac{1.0 - e^{-\sigma_1 \Delta s_1}}{\Delta s_1 (\sigma_1)^2}, \quad i = i', \quad (51)$$

$$\frac{\exp \left[- \sum_{k=i'+1}^{i-1} \sigma_k \Delta s_k \right] (1.0 - e^{-\sigma_1 \Delta s_1}) (1.0 - e^{-\sigma_1 \Delta s_1})}{\Delta s_1 \sigma_1^2}, \quad i > i'.$$

Although our code is more general, for simplicity in Eq. (51) we have assumed that the mesh cells are square. Both expressions are derived by performing an uncollided electron balance over the i 'th path length cell. The uncollided flux is then distributed to the individual spatial cells in proportion to the area subtended on the target cell by an angular cone, originating from the source cell.

For this angular cone we use one of two forms, depending on the relative distance of the target path length from the path length of the source cell.

Figure 1 illustrates the construction of the angular cone for the discrete direction m , used for target path lengths when $i > i' + 1$. The angular cone is generated by extending the region of influence of the discrete direction m to include half of the angular distance to each of the $m+1$ and $m-1$ directions. The area created by the intersection of this angular cone and the $i \pm \frac{1}{2}$ boundaries of the target path length cell defines a region over which ϕ_0^T is to be distributed. The individual elements of $[L^m]^{-1}$ are then calculated based on the ratio of area contained within a particular mesh cell to this total area,

$$\phi_{ij,j'}^{m-1} = \phi_0^T \left(\frac{\text{Area}_{ij}}{\text{Area}_i} \right) \quad (52)$$

where

Area_{ij} = area of intersection within cell ij

and

Area_i = total area of intersection within path length cell i

If a cell within the target path length is not intercepted by the angular cone the matrix element for that target cell is zero. In fact the majority of these elements are zero, as is clearly evident from Fig. 1.

Figure 2 illustrates the construction of the angular cone for target path length cells for which $i \leq i' + 1$. Whereas the angular cone originated from the center of the source cell for the target path length steps above, it is now constructed so that the $m \pm \frac{1}{2}$ boundaries of the cone, originate from the centers of the spatial edges of the source cell. Once the area is defined Eq. (52) is again used for calculating the individual elements.

The distinction between these two cases is made based on physical arguments. If the previous cell centered scheme were used throughout the discrete ordinates grid, the elements of $[L_m]^{-1}$ for adjacent cells would be underestimated. In fact, a simple examination of Fig. 1 shows that for this scheme, regardless of the discrete direction, the elements of $[L_m]^{-1}$ for the cells immediately above and below the source cell, $i'j'$, would be zero.

On the other hand, if the above cell edge center scheme (Fig. 2) were applied to the entire grid, the extended regions of adjacent discrete directions would overlap for distant cells overcompensating for the use of discrete ordinates.

This semi-analytic geometric scheme described above for computing the elements $[L_m]^{-1}$ is the fundamental mechanism whereby both ray effects and numerical diffusion are removed. The use of discrete ordinates is compensated for by extending the region of influence of each discrete direction to include a portion of the previously 'unseen' space between adjacent directions. In this manner the streaming particles are allowed access to the entire phase space. The numerical diffusion has been reduced by explicitly setting to zero those elements of $[L_m]^{-1}$ which should be zero.

The use of cones (instead of discrete directions) is not a new idea,²³ however here they are used to determine all of the matrix elements directly, and not just those corresponding to cells immediately adjacent to the source cell. It is the use of cones for uncollided transport to distant cells that eliminates ray effects. Unlike other ray effect mitigation techniques this new method is

quite efficient, being 2.6 times slower than conventional S_N on scalar machines, but only 1.2 times slower on vector machines.

Because of the many zeros in the matrix $[L^m]^{-1}$ the SCS_N method does not make efficient use of computer memory nor does it make efficient use of the computational resources of a scalar machine (due to the many unnecessary multiplications by zero). However with the large memory machines now available the former inefficiency is often irrelevant and the fact that the source iteration is cast in matrix form enables extensive use of vector and/or parallel processing that can compensate for the latter inefficiency.

The SCS_N method was tested using a 200 KeV isotropic point source incident on aluminum slabs. With coarse mesh cells (37 mfp squares) the new and conventional S_N methods were in close agreement (see Fig. 3). However, with fine mesh cells (3.7 mfp squares) the new method was not subject to the ray effects evident with the conventional solution (see Fig. 4).

To demonstrate the lack of numerical diffusion obtained with the SCS_N method we have calculated the electron flux due to a monodirectional source ($\mu = .30$) incident on the $s = 0$ surface of a vacuum. The results are shown in Table I along with those obtained from the conventional S_N method with and without a negative flux fix-up, and in Table II along with those obtained using the SR method with and without a ray effect mitigation routine.

The SCS_N results are clearly superior to either of the conventional S_N solutions in representing the discontinuity along the edge of the beam. If the source particles are interpreted as a monodirectional beam, then the SR results with no ray effect mitigation represent the true solution and all particles should remain within the dotted lines shown in Table II. On the other hand, if the source particles are assumed to be distributed between $\mu = .25$ and $\mu = .35$, the edges of the cone corresponding to direction $\mu = .30$, then the flux should be contained between the solid lines shown in Tables I and II, and the results are best calculated by the SCS_N method. For this interpretation of the source, the SR method does better with the ray effect mitigation routine turned on, however, it is evident that this routine is only partially successful, as the flux still peaks along the source direction.

III. Numerical Diffusion Theory

The mathematical/numerical description of how electrons interact with electronic devices can be classified into three fundamental calculational categories. The probabilistic approach embodied in the Monte Carlo method is simply a numerical simulation of the collision interactions and subsequent streaming of electrons and requires considerable computational resources to use effectively. The deterministic transport methods as described in Sections the previous sections offer a viable alternative to the Monte Carlo method but may, in some cases, provide more detailed information than is necessary for an adequate description. In particular, at the low end of the electron energy spectrum when the electrons have experienced many collisions, the complete angular flux variation in angle is not always necessary since the flux is nearly isotropic. For this reason, an effort has been initiated to develop a diffusion theory description in parallel with the transport theory description. The diffusion equation is a macroscopic deterministic description of electron motion and involves far less computational effort than either Monte Carlo or transport theory methods.

The main goal of the diffusion theory component is to generate a reliable three-dimensional algorithm that will be coupled to a 2-D or 3-D S_N algorithm at an appropriately low energy. In this way, we hope to treat both the high and low energy regions with the greatest efficiency.

In the following, the progression toward the completion of the 3-D algorithm is documented. We begin with a 1-D development which establishes an adequate foundation for the multidimensional algorithms to follow. From this initial study, a proper understanding of how the multidimensional algorithm is obtained. Many of the numerical features of the 1-D treatment have been incorporated into the multidimensional algorithms making the 1-D study invaluable. An alternative approach would have been to use an "off-the-shelf" diffusion code with enough flexibility to accommodate electron motion in condensed matter; however, the benefit of the very worthwhile learning experience would have been lost.

A. 1-D Diffusion Theory

The generic diffusion equation describing electron transport as modeled by the Spencer-Lewis equation (1) can be written in one-dimension as

$$\frac{\partial \phi}{\partial s}(x,s) = \frac{\partial}{\partial x} p(x,s) \frac{\partial}{\partial x} \phi(x,s) - q(x,s) \phi(x,s) + S(x,s) \quad (53a)$$

where

$\phi(x,s)$ = electron angularly integrated density (simply called density) for electrons having transversed a total path length s to arrive at position x

p = diffusion coefficient

q = absorption cross section

S = external source.

The density is subject to the following initial and general mixed boundary conditions

$$\phi(x,0) = f(s) \quad (53b)$$

$$\gamma_0(s) \frac{\partial \phi}{\partial x}(x,s) + \gamma_1(s) \phi(x,s) = \sigma(x) \text{ at } x = a, b \quad (53c)$$

at the boundaries a and b where γ_0, γ_1 are known functions. Equations (53) can be obtained from Eq. (1) in many ways. The simplest method is to integrate Eq. (1) over μ (in one dimension) and define the density as

$$\phi(x,s) = \int_{-1}^1 d\mu \phi(x,\mu,s)$$

and current as

$$J(x,s) = \int_{-1}^1 d\mu \mu \phi(x,\mu,s)$$

and then invoke Fick's law

$$J(x,s) \approx - \frac{\partial}{\partial x} p(x,s) \frac{\partial}{\partial x} \phi(x,s) .$$

The absorption term is included for generality and the boundary conditions result from partial current considerations. Implicit in the derivation of Eqs. (53) is the assumption of a linear angular dependence of the angular flux on the electron direction μ in one dimension. This is true only after many collisions and a distance of at least three mean free paths from discontinuities such as material boundaries and spatially localized sources. For these reasons, Eqs. (53) are anticipated to be applicable when the electrons have traversed a relatively large path length at (low energy) and in large homogeneous regions. Nevertheless, a reasonable approximation can be obtained from diffusion theory at material boundaries of scattering materials.

1. Point Spatial Finite Difference Scheme²⁷

To derive a numerical algorithm to solve Eqs. (53), we first partition the x variable into discrete intervals as shown in Fig. 5. The interval midpoint is designated as i and the cell right and left boundaries by $i - \frac{1}{2}$ and $i + \frac{1}{2}$ respectively. Next Eq. (53a) is integrated over cell i to give

$$\begin{aligned} \frac{\partial}{\partial s} \int_{x_{i-\frac{1}{2}}}^{x_{i+\frac{1}{2}}} dx \phi(x,s) &= \int_{x_{i-\frac{1}{2}}}^{x_{i+\frac{1}{2}}} dx \frac{\partial}{\partial x} p \frac{\partial \phi}{\partial x}(x,s) - \\ &- \int_{x_{i-\frac{1}{2}}}^{x_{i+\frac{1}{2}}} dx q(x,s) \phi(x,s) + \int_{x_{i-\frac{1}{2}}}^{x_{i+\frac{1}{2}}} dx S(x,s) . \end{aligned}$$

Then integrating the second term exactly and using the approximations

$$\int_{x_{i-\frac{1}{2}}}^{x_{i+\frac{1}{2}}} dx \, h(x,s) \phi(x,s) \simeq \frac{h_i \Delta x_i + h_{i+1} \Delta x_{i+1}}{2} \phi_i(s)$$

$$\left. \frac{\partial \phi(x,s)}{\partial x} \right|_{x_{i-\frac{1}{2}}} \simeq (\phi_i(s) - \phi_{i-1}(s)) / \Delta x_i$$

$$\left. \frac{\partial \phi(x,s)}{\partial x} \right|_{x_{i+\frac{1}{2}}} \simeq (\phi_{i+1}(s) - \phi_i(s)) / \Delta x_{i+1} ,$$

we arrive at the spatially differenced equation

$$\frac{d}{ds} \phi_i(s) = a_i(s) [\phi_{i-1}(s) - \phi_i(s)] + c_i(s) [\phi_{i+1}(s) - \phi_i(s)] - \Gamma_i(s) \phi_i(s) + Q_i(s) \quad (54a)$$

where

$$a_i(s) = \frac{2 p_i(s)}{\Delta x_i (\Delta x_i + \Delta x_{i+1})} \quad (54b)$$

$$c_i(s) = \frac{2 p_{i+1}(s)}{\Delta x_{i+1} (\Delta x_i + \Delta x_{i+1})} \quad (54c)$$

$$\Gamma_i(s) = (q_i(s) \Delta x_i + q_{i+1}(s) \Delta x_{i+1}) / (\Delta x_i + \Delta x_{i+1}) \quad (54d)$$

$$Q_i = (S_i(s) \Delta x_i + S_{i+1}(s) \Delta x_{i+1}) / (\Delta x_i + \Delta x_{i+1}) . \quad (54e)$$

At this point there are several ways the path variable s could be handled and in the following sections we discuss two of these.

2. Continuous Analytical Continuation

A theoretically simple and computationally efficient method for effecting the s integration of Eqs. (54) is found by using Taylor series.²⁸ This method has been rediscovered recently and it is quite surprising that it has not found more widespread use.

To begin with, we assume that $p_i(s)$, $q_i(s)$ and $S_i(s)$ are given functions of s in a homogeneous cell i and these functions can be expanded in Taylor series in $s_{r-1} \leq s \leq s_r$ to give

$$a_i(s) = \sum_{k=0}^{\infty} \frac{a_{i,k}^r}{k!} (s-s_{r-1})^k \quad (55a)$$

$$c_i(s) = \sum_{k=0}^{\infty} \frac{c_{i,k}^r}{k!} (s-s_{r-1})^k \quad (55b)$$

$$\Gamma_i(s) = \sum_{k=0}^{\infty} \frac{\Gamma_{i,k}^r}{k!} (s-s_{r-1})^k \quad (55c)$$

$$Q_i(s) = \sum_{k=0}^{\infty} \frac{Q_{i,k}^r}{k!} (s-s_{r-1})^k \quad (55d)$$

According to Eqs. (54b-e) the expansion coefficients a_{ik} , c_{ik} , Γ_{ik} and Q_{ik} are related to the expansion coefficients of p_i , q_i and S_i around an arbitrary point s_{r-1} . When $\phi_i(s)$ is similarly expanded in $s_{r-1} \leq s \leq s_r$

$$\phi_i(s) = \sum_{k=0}^{\infty} \frac{\phi_{i,k}^r}{k!} (s-s_{r-1})^k, \quad (56)$$

a recurrence relation results for ϕ_{ik}^r when Eq. (56) is introduced into Eq. (54a)

$$\begin{aligned} \phi_{i,k}^r = & \sum_{j=0}^{k-1} \frac{k!}{(k-j)!} a_{i,k-j}^r [\phi_{i-1,j}^r - \phi_{i,j}^r] + \\ & + \sum_{j=0}^{k-1} \frac{k!}{(k-j)!} c_{i,k-j}^r [\phi_{i+1,j}^r - \phi_{i,j}^r] - \sum_{j=0}^{k-1} \frac{k!}{(k-j)!} \Gamma_{i,k-j}^r \phi_{i,j}^r + Q_{i,k-1}^r \end{aligned} \quad (57a)$$

with

$$\phi_{i,0}^r = \phi_i(s_{r-1}) \quad (57b)$$

Thus, we have an explicit two-dimensional recurrence relation for $\phi_{i,k}^r$ which when introduced into Eq. (56) provides the solution $\phi_i(s)$. The advantage of this formulation is that round off error can be controlled by the choice of the interval boundaries s_r . These points are chosen such that the series in Eq. (56) is convergent and requires less than about ten terms for convergence to a desired accuracy. By using the previously calculated value $\phi_i(s_{r-1})$ as the initial condition in the interval $s_{r-1} \leq s \leq s_r$, we are continually analytically continuing the Taylor series representation to the subsequent intervals--hence the name of the method. This approach has been shown to be very accurate in other areas of application such as neutron slowing down theory, extended gas kinetics and radioactive decay. A second major advantage of the method (not used here) is in application to nonlinear ordinary differential equations.

The method can equally be applied to the multidimensional diffusion equation and its numerical implementation will be discussed for the 3-D application in a future report.

3. Path Length Discretization

Following along more conventional lines, the path length derivative can be discretized as follows:

$$\frac{\phi_i^{n+1} - \phi_i^n}{\Delta s} \simeq (\phi_i^{n+1} - \phi_i^n) / \Delta s$$

In addition, if $\phi_1(s)$ is composed of fractions of ϕ_1^n and ϕ_1^{n+1} in the form

$$\phi_1(s) = \alpha \phi_1^{n+1} + (1-\alpha) \phi_1^n, \quad 0 \leq \alpha \leq 1,$$

Eq. (54a) becomes

$$\begin{aligned} \left[\frac{1}{\Delta s} - \alpha \bar{b}_1^n \right] \phi_1^{n+1} &= \alpha \bar{c}_1^n \phi_{1+1}^{n+1} + \alpha \bar{a}_1^n \phi_{1+1}^{n+1} + (1-\alpha) \bar{a}_1^n \phi_{1-1}^n + \left[(1-\alpha) \bar{b}_1^n + \frac{1}{\Delta s} \right] \phi_1^n + \\ &+ (1-\alpha) \bar{c}_1^n + \bar{Q}_1^n \end{aligned} \quad (58a)$$

where

$$\bar{a}_1^n = (a_1^n + a_1^{n+1})/2 \quad (58b)$$

$$\bar{c}_1^n = (c_1^n + c_1^{n+1})/2 \quad (58c)$$

$$\bar{\Gamma}_1^n = (\Gamma_1^n + \Gamma_1^{n+1})/2 \quad (58d)$$

$$\bar{b}_1^n = -\bar{a}_1 - \bar{c}_1 - \bar{\Gamma}_1 \quad (58e)$$

$$\bar{Q}_1^n = (Q_1^n + Q_1^{n+1})/2 \quad (58f)$$

In matrix form, Eq. (58a) can be written as

$$\begin{aligned} \frac{\vec{\phi}^{n+1} - \vec{\phi}^n}{\Delta s} &= \alpha \underline{A}^n \vec{\phi}^{n+1} + (1-\alpha) \underline{A}^n \vec{\phi}^n + \vec{Q}^n \\ \phi^n &= \vec{\phi}(s_n) \end{aligned} \quad (59)$$

where A^n is the classic tridiagonal matrix which will be exploited below.

By varying the value of α , one obtains the following well-known discretization schemes

$$\alpha = 1 \quad , \quad \text{implicit}$$

$$\alpha = 0 \quad , \quad \text{explicit}$$

$$\alpha = \frac{1}{2} \quad , \quad \text{Crank-Nicolson.}$$

4. Numerical Implementation and Test Case Results

a. Iteration

Iteration is commonly used to solve Eqs. (58) in lieu of the more costly direct inversion methods. The scheme can be represented as follows:

$$(0) \phi_1^{n+1} = \phi_1^n \tag{60a}$$

$$(j) \phi_1^{n+1} = F[(j-1) \phi_{i+1}^{n+1}, (j) \phi_{i-1}^{n+1}, \phi_{i+1}^n, \phi_i^n, \phi_{i-1}^n] \tag{60b}$$

where j is the iteration index. To test the iteration procedure, the volume source driven analytical benchmark with constant properties

$$\frac{\partial \phi(x,s)}{\partial s} = \frac{\partial^2 \phi(x,s)}{\partial x^2} - \phi(x,s) + 1 \tag{61a}$$

$$\phi(x,0) = 0, \quad \phi(\pm 1/2, 0) = 0 \tag{61b}$$

was used with the solution

$$\phi(x,s) = \sum_{n=0}^{\infty} \frac{(-1)^n}{B_n(1+\beta_n^2)} \left[1 - e^{-(1+B_n^2)s} \right] \cos(B_n x) \tag{62}$$

where

$$B_n = (2n+1)\pi$$

Also of note is the approach to the "steady state" or equilibrium solution

$$\phi(x) = 1 - \cosh(x)/\cosh(1/2) \quad (63)$$

as s approaches infinity.

Table 3 displays the relative error for increasing iteration index with $\alpha=0.5$ at several points within the slab and for a uniformly distributed source emitting electrons at all path lengths. A rather large number of iterations are required to achieve acceptable accuracy which is considered to be 10^{-3} for the electron studies presented here. The approach to the equilibrium solution is shown in Figs. 6a,b with a graphical comparison of the exact and finite difference (FD) solution given in Fig. 6c for $\Delta s = 0.01$ and $\Delta x = 0.05$. Again acceptable agreement is noted. Table 4 gives the relative error variation with Δs at large values of s as $\phi(s)$ approaches the equilibrium solution for $\Delta x = 0.05$. There is some indication that refining Δs without refining Δx does not improve the results. This is an indication of a limitation resulting from the iteration procedure. Figures 7a,b demonstrate that in general the best choice of α is $\frac{1}{2}$. This choice of α apparently combines the accuracy of the explicit method and the stability of the implicit formulation. A comparison of results for different Δs 's is shown in Figs. 8a,b. The accuracy is apparently limited by Δx as was similarly found in analyzing the approach to the equilibrium solution (see Table 4). Figure 9 shows the improvement as Δx is reduced for a fixed Δs . Again the results are not expected to improve as Δx is further reduced unless Δs is also reduced.

b. Direct Matrix Inversion

The iteration process can be avoided altogether by utilizing a tridiagonal solver (TDS) to perform the required matrix inversion of Eq. (59) in the form

$$\left(\frac{1}{\Delta s} - \alpha \underline{A}^n \right) \vec{\phi}^{n+1} = (1-\alpha) \underline{A}^n \vec{\phi}^n + \vec{Q}^n \quad (64)$$

That the iteration is responsible for an apparent instability when Δx is reduced with Δs fixed is clearly demonstrated in Figs. 10a,b. In this figure and those to follow, L_x is the number of interval partitions of the slab length. The iterative solution oscillates widely about the exact solution for small values of Δs ; whereas, the TDS solution does not and consistently provides accurate results for all values of Δx . Thus there is a compelling argument to abandon the iterative procedure in favor of the TDS.

For the comparisons to follow, a global figure of merit to measure the error,

$$E_{GL}(s) = \frac{1}{b-a} \int_a^b dx |\phi(x,s) - \phi_E(x,s)| \approx \frac{1}{b-a} \sum_{i=1}^{L_x} \Delta x_i |\phi_i(s) - \phi_{Ei}(s)| \quad (65)$$

has been found to give a reliable characterization of solution. L_x is the total number of spatial intervals between a,b and ϕ_E represents the exact solution. The variation of E_{GL} with s for several L_x is displayed in Figs. 11a,b again effectively indicating the increased stability of the tridiagonal matrix inversion.

To further demonstrate the superiority of the TDS, several additional test problems with analytical solutions have been considered. The test cases have been designed to span the types of situations anticipated to occur when evaluating electron penetration in actual electronic devices.

The second problem considered is for a slab with constant properties p and q and is driven by a boundary source ϕ_T . The analytical solution is

$$\phi(x,s) = \phi_T \left[\frac{\sinh \left(\sqrt{\delta} x \right)}{\sinh \left(\sqrt{\delta} a \right)} + 2 \sum_{n=1}^{\infty} \frac{e^{-p\gamma_n^2 s}}{a\gamma_n} \sin(\gamma_n x) \right] \quad (66)$$

$$\gamma_n = n\pi/a, \delta = q/p$$

Figures 12 again show unphysical behavior of the iterative solution as Δx is reduced. The more well behaved solution obtained by the tridiagonal solver is shown in Fig. 12b. The density near the source boundary seems to become less accurate as Δx decreases. This inaccuracy can be eliminated if a finer mesh is specified near the boundary than for the interior. Figure 12c shows the improvement when only a single small additional interval is introduced at the boundaries--the discrepancy is completely eliminated. Figures 13a,b,c give the corresponding global errors for the second benchmark. The global errors for the variation of Δs in the iteration and matrix solutions are shown in Fig 14a,b. Again the improvement provided by the tridiagonal solver is clearly evident.

As a final demonstration, the diffusion coefficient p in problem 1 was varied from 0.1 to 50 and the global error for the TDS is presented in Fig. 15. The accuracy decreases as p increases most likely resulting from the increased emphasis of the discrete approximations used for the spatial derivatives as p increases. These results indicate that variable electron properties can easily be accommodated with acceptable accuracy.

5. Dose Calculation

In an attempt to apply the discretized solution to a realistic problem, the dose in thick aluminum was determined. The diffusion equation describing the collided density f_c is

$$\left[\frac{\partial}{\partial s} - \rho D \frac{\partial^2}{\partial x^2} \right] f_c(x,s) = \frac{1}{\lambda^* \rho} f_c(x,s) \quad (67a)$$

$$f_c(x,0) = 0 \quad , \quad f_c(r_0,s) = 0 \quad (67b)$$

where r_0 is the electron range in aluminum and all properties are assumed constant with

$$D = \lambda^*/3 \quad .$$

The uncollided electron density for normal incidence is given by

$$f_0(x,s) = \rho\eta \frac{e^{-s/\lambda^*}}{s} \theta(s-x) \quad , \quad \eta \equiv x/s \quad . \quad (68)$$

The electron density is therefore

$$\phi(x,s) = f_0(x,s) + f_c(x,s) \quad (69)$$

yielding the dose

$$D(x) = \int_0^{r_0} ds \left| \frac{dE}{ds} \right| \phi(x,s) \quad . \quad (70)$$

for a constant stopping power and the dose normalized at $x = 0$, the results are shown in comparison with other theories in Fig. 16. Surprisingly good agreement is achieved which is most probably fortuitous given the crude nature of the dose approximation. The results, however, are encouraging.

B. 2-D Diffusion Theory

The diffusion equation in two-dimensions is

$$\begin{aligned} \frac{\partial \phi}{\partial s}(x,y,s) = & \frac{\partial}{\partial x} p(x,y,s) \frac{\partial}{\partial x} \phi(x,y,s) + \\ & + \frac{\partial}{\partial y} p(x,y,s) \frac{\partial}{\partial y} \phi(x,y,s) - q(x,y,s) \phi(x,y,s) + S(x,y,s) \end{aligned} \quad (71a)$$

with boundary and initial conditions

$$\phi(a,y,s) = \sigma_L, \quad \phi(b,y,s) = \sigma_R \quad (71b)$$

$$\phi(x,c,s) = \sigma_T, \quad \phi(x,d,s) = \sigma_B \quad (71c)$$

$$\phi(x,y,0) = f(x,y) \quad (71d)$$

Integrating over cell (i,j) depicted in Fig. 17 and employing the approximations

$$\int_{A_{ij}} dx dy \phi(x,y,s) = \frac{\phi_{i,j}}{4} (\Delta y_j + \Delta y_{j+1}) (\Delta x_i + \Delta x_{i+1})$$

$$\int_{\bar{A}\bar{B}} dA p \frac{\partial \phi}{\partial n} \approx \frac{\phi_{i,j} - \phi_{i,j-1}}{\Delta y_i} \left[\frac{\Delta x_i - \Delta x_{i+1}}{2} \right] p_{i,j}$$

results in

$$\begin{aligned} \frac{d \phi_{i,j}}{ds} = & [a_{i,j} \phi_{i-1,j} + c_{i,j} \phi_{i+1,j} + b_{i,j} \phi_{i,j}] + \\ & + [d_{i,j} \phi_{i,j-1} + f_{i,j} \phi_{i,j+1} + e_{i,j}] - \tilde{q}_{i,j} \phi_{i,j} + \tilde{Q}_{i,j} \end{aligned} \quad (72)$$

where $a_{i,j}$, $b_{i,j}$, $c_{i,j}$, $d_{i,j}$, $e_{i,j}$, $f_{i,j}$, $\tilde{q}_{i,j}$ and $\tilde{Q}_{i,j}$ are cell constants. Several differencing schemes for the path length variable will now be discussed: Note that one could, in addition, apply the continuous analytical continuation technique (§III.A.2), however, that approach will only be applied in the 3-D study.

1. Two-Step Alternating Direction Implicit (ADI)

In this scheme, the path length derivative is split in the interval Δs and the resultant set of equations is first solved in the x direction and then in the y direction. In step 1,

$$\frac{d \phi_{i,j}}{ds} \approx \frac{\phi_{i,j}^{n+\frac{1}{2}} - \phi_{i,j}^n}{\Delta s/2}$$

yielding

$$\begin{aligned} \phi_{i,j}^{n+\frac{1}{2}} = & \phi_{i,j}^n + \frac{\Delta s}{2} \left[a_{i,j} \phi_{i-1,j}^{n+\frac{1}{2}} + c_{i,j} \phi_{i+1,j}^{n+\frac{1}{2}} + \right. \\ & \left. + b_{i,j} \phi_{i,j}^{n+\frac{1}{2}} \right] + \frac{\Delta s}{2} \left[d_{i,j} \phi_{i,j-1}^n + f_{i,j} \phi_{i,j+1}^n + e_{i,j} \phi_{i,j}^n \right] - \\ & - \tilde{a}_{i,j} \frac{\Delta s}{2} \phi_{i,j}^{n+\frac{1}{2}} + \frac{\Delta s}{2} \tilde{Q}_{i,j}^{n+\frac{1}{2}} \end{aligned} \quad (73)$$

Eq. (73) is solved using the TDS in the i direction. The second step consists of the approximation

$$\frac{d \phi_{i,j}}{ds} \approx \frac{\phi_{i,j}^{n+1} - \phi_{i,j}^{n+\frac{1}{2}}}{\Delta s/2}$$

giving

$$\begin{aligned} \phi_{i,j}^{n+1} = & \phi_{i,j}^{n+\frac{1}{2}} + \frac{\Delta s}{2} \left[\quad \right]^{(n+\frac{1}{2})} + \\ & + \frac{\Delta s}{2} \left[\quad \right]^{(n+1)} - \tilde{a}_{i,j}^{n+1} \frac{\Delta s}{2} \phi_{i,j}^{n+1} - \frac{\Delta s}{2} \tilde{Q}_{i,j}^{n+1} \end{aligned} \quad (74)$$

where the terms in the brackets are the same as in Eq. (73) evaluated at the indicated discrete path length. The TDS is then applied in the j direction giving the final solution at s_{n+1} .

2. Iterative Methods

As in the 1-D case, there exists an iterative formulation of the solution to Eq. (72) when the backward finite difference approximation to the path length derivative is employed. The formulation becomes

$$\phi_{i,j}^{n+1} = F[\phi_{i-1,j}^{n+1}, \phi_{i,j-1}^{n+1}, \phi_{i+1,j}^{n+1}, \phi_{i,j+1}^{n+1}] \quad (75a)$$

with

$$\phi_{i,j}(s) = \alpha \phi_{i,j}^{n-1} + (1-\alpha) \phi_{i,j}^n, \quad 0 \leq \alpha \leq 1 \quad (75b)$$

In the following, several of the many possible ways of solving for $\phi_{i,j}^{n+1}$ are indicated:

a. Line-Jacobi (LJ) with TDS

$$^{(0)}\phi_{i,j}^{n+1} = ^{(0)}\phi_{i,j}^n \quad (76)$$

$$^{(k)}\phi_{i,j}^{n+1} = F(^{(k)}\phi_{i-1,j}^{n+1}, ^{(k)}\phi_{i+1,j}^{n+1}, ^{(k-1)}\phi_{i,j-1}^{n+1}, ^{(k-1)}\phi_{i,j+1}^{n+1})$$

b. Successive Overrelaxation (SOR) with Iteration

$$^{(k)}\phi_{i,j}^{n+1} = \omega F(^{(k)}\phi_{i-1,j}^{n+1}, ^{(k)}\phi_{i+1,j}^{n+1}, ^{(k-1)}\phi_{i,j-1}^{n+1}, ^{(k-1)}\phi_{i,j+1}^{n+1}) + (1-\omega) ^{(k-1)}\phi_{i,j}^{n+1} \quad (77a)$$

$$0 < \omega < 1 \quad (77b)$$

c. Successive Line Overrelaxation (SLOR) with TDS

$$^{(k)}\bar{\phi}_{i,j}^{n+1} = F(^{(k)}\bar{\phi}_{i-1,j}^{n+1}, ^{(k)}\bar{\phi}_{i,j-1}^{n+1}, ^{(k)}\phi_{i+1,j+1}^{n+1}, ^{(k-1)}\phi_{i,j+1}^{n+1}) \quad (78a)$$

$$^{(k)}\phi_{i,j}^{n+1} = \omega ^{(k)}\bar{\phi}_{i,j}^{n+1} + (1-\omega) ^{(k-1)}\phi_{i,j}^{n+1} \quad (78b)$$

$$0 < \omega < 1 \quad (78c)$$

3. Test Results and Discussion

A source driven test problem with constant properties and a uniform source of the form

$$s(s) = Q_0 e^{-\beta s}$$

will be used to test the various solution procedures described above. For zero density on the boundary, the solution is

$$\phi(x,y,s) = \frac{16 Q_0}{ab} \sum_{m,n} A_{m,n} \quad (79a)$$

with

$$A_{m,n} = e^{\beta s} - e^{-(q+p(B_{mx}^2 + B_{ny}^2))s} \cos(B_{mx} x) \cos(B_{ny} y) \quad (79b)$$

$$B_{mx} = (2n+1) \pi/a$$

$$B_{ny} = (2m+1) \pi/b$$

A more numerically amenable solution is obtained by rearranging the series in Eq. (79a) in the form

$$\phi(x,y,s) = \frac{16 Q_0}{ab} \sum_{n=0}^{\infty} \sum_{m=0}^n A_{m,n-m} \quad (80)$$

Figures 18a,b,c show comparisons of the ADI, LJ and SOR solution at $y = 0$ and $s = 0.5$ to the benchmark solution for the variation of Δx and Δy . L_x and L_y are the number of intervals in the x and y directions respectively. All methods seem to give comparable accuracy. The ADI and SOR methods require the largest computational time with the LJ technique requiring the least. Further testing will determine the final selection of the best method for the anticipated vulnerability studies.

4. Transport/Diffusion Coupling

To demonstrate the coupling of a transport and diffusion calculation, Fig. 19 shows a simulated two dimensional approximation to a one-dimensional transport result. For this calculation,

the density profile at $s = 5$ was taken from an analytical transport theory calculation²⁹ and used as the initial condition to the 2-D LJ diffusion solution. Both the analytical and diffusion theory calculations were then run to $s = 15$ and Fig. 19 shows the comparison for several L_x , L_y . Acceptable agreement is seen except possibly near the peak. The comparison can be improved, however, by taking a finer mesh in region of the peak. Additional studies have been performed indicating that the coupling of transport theory and diffusion theory in the above manner is a viable calculational method. It is this coupling that will serve as the basis for future development of the diffusion theory model.

IV. Development of analytical Benchmark Methods

The trademark of the electron transport theory methods development at the University of Arizona has been and will continue to be the pursuit of analytical benchmarks while in the process of forming numerical algorithms.³⁰⁻³¹ The interaction of these two components has proved to be invaluable in the development of reliable and efficient numerical methods.

The benchmark methods to be presented below represent an entirely new concept in benchmarking. While the benchmarks established thus far are not directly applicable to the electron transport application, the methods will certainly prove helpful in developing new benchmarks that will be.

A. Benchmarks from Laplace Transform Inversion

The method in this section is taken from Ref. (30). Recently a highly reliable numerical Laplace transform inversion has been developed based on the transformation of the Bromwich inversion integral into a cosine integral. The cosine integral is then represented as an infinite series of integrals. These integrals are evaluated using a Romberg integration scheme and the convergence of the series is accelerated with an Euler-Knopp acceleration algorithm. In addition, the inversion is performed on several contours and agreement is required. A demonstration of the accuracy of

the inversion is shown in Fig. 20 where the algorithm accuracy ϵ was varied from 10^{-2} to 10^{-6} .

This algorithm will now be used to provide highly accurate (3-5 digit) benchmarks for the stationary one velocity Boltzmann equation.

Consider the one-group Boltzmann equation in a semi-infinite medium with isotropic scattering

$$\left[\mu \frac{\partial}{\partial x} + 1 \right] \phi(x, \mu) = \frac{c}{2} \int_{-1}^1 d\mu' \phi(x, \mu') \quad (81)$$

The flux illuminating the boundary is assumed to be isotropic

$$\phi(0, \mu) = 1 \quad , \quad \mu > 0 \quad .$$

Then from integral transport theory we have

$$\phi(0, \mu) = - \frac{c}{2\mu} \int_0^{\infty} dx' e^{x'/\mu} \phi(x') \quad (82)$$

for $\mu < 0$. By letting $\mu \rightarrow -1/s$ where s is a complex variable, we note that Eq. (82) becomes a Laplace transform. Thus upon inversion

$$\phi(x) = \frac{2}{c} \int_0^{\infty} ds \left[\frac{\phi(0, -1/s)}{s} \right] \quad (83)$$

The inversion can be performed numerically since $\phi(0, -\mu)$ is known to be

$$\phi(0, -\mu) = 1 - \sqrt{1-c} H(\mu) \quad (84)$$

where $H(\mu)$ satisfies the non-linear integral equation

$$H(\mu) = 1 + \frac{c}{2} \mu H(\mu) \int_0^1 d\mu' \frac{H(\mu')}{\mu' + \mu} \quad (85)$$

The analytical continuation of $\phi(0, -\mu)$ to the complex s plane can easily be done thus allowing the numerical inversion.

The numerical inversion is applicable to any linear transport problem in which the exiting distribution is known. Figure 21a-d show results for several basic transport problems with isotropic scattering in a semi-infinite medium including

1. beam source illuminating the boundary
2. one-half space Milne problem
3. uniform source in right half space.

The method is equally applicable to the case of anisotropic scattering.

In the future an attempt will be made to apply the numerical inversion to the discretized 2-D transport equation in order to treat the s variable continuously and provide a reasonable 2-D transport benchmark for electrons.

B. Moments by Continuous Analytical Continuation

Accurate moments of the Spencer-Lewis equation in one-dimension

$$\left[\frac{\partial}{\partial s} + \mu \frac{\partial}{\partial x} + \lambda(s) \right] \phi(x, \mu, s) = \lambda(s) \int_{-1}^1 d\mu' f(\mu', \mu) \phi(x, \mu', s) \quad (86)$$

in infinite geometry are of considerable importance in the reconstruction of the density. The moments are defined by

$$M_{\ell,k}(s) = \exp \left[- \int_0^s ds' \lambda(s') \right] \int_{-1}^1 d\mu P_{\ell}(\mu) \int_{-\infty}^{\infty} dx x^n \phi(x, \mu, s) \quad (87)$$

where P_{ℓ} is the Legendre polynomial of order ℓ . $M_{\ell,k}$ satisfies the following set of ordinary differential equations

$$\frac{dM_{\ell,k}}{ds} + a_{\ell} M_{\ell+1,k-1} + b_{\ell} M_{\ell-1,k-1} = \lambda(s) (1-\omega_{\ell}) M_{\ell,k} + Q_{\ell,k}(s) \quad (88)$$

where

$$\omega_{\ell} = \int_{-1}^1 d\mu' P_{\ell}(\mu') f(\mu', \mu)$$

and $Q_{\ell,k}$ contains boundary densities known from an independent calculation or approximated from a lower order theory. Then by expanding $Q_{\ell,k}$ and $M_{\ell,k}$ in Taylor series in the interval $s_{r-1} \leq s \leq s_r$

$$\lambda(s) = \sum_{n=0}^{\infty} \frac{\lambda_n^r}{n!} (s-s_{r-1})^n$$

$$Q_{\ell,k} = \sum_{n=0}^{\infty} \frac{Q_{n,\ell,k}^r}{n!} (s-s_{r-1})^n$$

$$M_{\ell,k}(s) = \sum_{n=0}^{\infty} \frac{M_{n,\ell,k}^r}{n!} (s-s_{r-1})^n ,$$

we find the recurrence relation

$$M_{n,\ell,k}^r = - a_{\ell} M_{n-1,\ell+1,k-1}^r - b_{\ell} M_{n-1,\ell-1,k-1}^r + \quad (89)$$

$$+ (1-\omega_\ell) \sum_{j=0}^{n-1} \frac{n!}{(n-j)!} \lambda_{n-j}^r M_{j,\ell,k}^r + Q_{n-1,\ell,k}^r M_{0,\ell,k}^r =$$

$$M_{0,\ell,k}^r = M_{n,\ell,k}^{r-1}(s_{r-1})$$

$M_{\ell,k}(s)$ can then be accurately obtained by defining as many s intervals as required for the desired convergence.

The density can be reconstructed in the usual way by an expansion in orthonormal polynomials Λ_ℓ

$$\phi(x,s) = \sum_{k=0}^{\infty} \phi_\ell(s) \Lambda_\ell(x) \quad (90a)$$

with

$$\phi_\ell(s) = \int_{-\infty}^{\infty} dx \Lambda_\ell(x) \quad (90b)$$

since

$$\Lambda_\ell(x) = \sum_{j=0}^{\ell} b_{\ell j} x^j$$

we have

$$\phi_\ell(s) = \sum_{j=0}^{\ell} b_{\ell j} M_{0,j}(s) \quad (90c)$$

One must be alert to the possibility of round off error contamination in Eqs. (89) and (90c).

Equations (90) are expected to provide accurate results away from the s,x wavefront. Acceleration techniques are then applied to Eq. (90a) in an attempt to mitigate round off error and provide more accurate solutions near the wave front discontinuity.

References

1. W. L. Filippone, S. Woolf, and J. C. Garth, "A Comparison of Two Discrete Ordinates Methods for Electron Transport Calculations," ANS Topl. Mtg. Advances in Reactor Computing, Salt Lake City, II, 649 (1983).
2. D. E. Bartine, R. G. Alsmiller, Jr., F. R. Mynott, W. W. Engle, Jr. and J. Barish, Nucl. Sci. Eng., 48, 159 (1972).
3. J. E. Morel, Nucl. Sci. Eng., 91, 324 (1985).
4. W. L. Filippone, M. S. Smith, S. Woolf and J. C. Garth, Nuc. Sci. Eng., 95, 22 (1987).
5. H. W. Lewis, Phys. Rev. 78, 526 (1950).
6. L. V. Spencer, Phys. Rev. 98, 1597 (1955).
7. W. L. Filippone, TTSP, 15(5), 629 (1986).
8. M. J. Berger, "Monte Carlo Calculations of the Penetration and Diffusion of Fast Charged Particles," Methods of Computational Physics, Vol. I, B. Adler, S. Fernbach, and M. Rotenburg, Eds., Academic Press, New York (1963).
9. J. A. Halbleib and T. A. Mehlhorn, "TTS: The Integrated TIGER Series of Coupled Electron/Photon Monte Carlo Transport Codes," SAND84-0573, Sandia National Laboratories (1984).
10. J. E. Morel, Nucl. Sci. Eng., 79, 340 (1981).
11. W. L. Filippone, M. S. Smith, S. Woolf and J. C. Garth, Nucl. Sci. Eng., 95, 22 (1987).
12. K. D. Lathrop, Nucl. Sci. Eng., 21, 498 (1965).
13. J. E. Morel, Nucl. Sci. Eng., 71, 64 (1979).
14. S. Goudsmit and J. L. Saunderson, Phys. Rev., 57, 24 (1940).
15. W. L. Filippone, Nucl. Sci. Eng., 99, 232 (1988).
16. W. L. Filippone and S. Woolf, "SMART Scattering Matrices for Single Collision Electron Monte Carlo Calculations," Proc. Int. topl. Mtg. Advances in Reactor Physics Mathematics and Computation, Vol. I, p. 389, Paris, France (1987).
17. M. Smith and W. L. Filippone, Trans. Am. Nucl. Soc., 55, 361 (1987).
18. W. L. Filippone, S. Woolf, J. C. Garth, IEEE Trans. Nucl. Sci. NS-34, 1564 (1987).
19. W. L. Filippone, S. Woolf, J. C. Garth, Trans. Am. Nucl. Soc., 55, 356 (1987).
20. B. G. Carlson and K. D. Lathrop, "Transport Theory--The Method of Discrete Ordinates," Computing Methods in Reactor Physics, Gordon and Breach Science Publishers, Inc., New York (1968).

21. Shean P. Monahan and W. L. Filippone, Trans. Am. Nucl. Soc., 56, 306 (1988).
22. W. L. Filippone, S. Woolf, and R. J. Lavigne, Nucl. Sci. Eng., 77, 119 (1981).
23. Y. Watanabe and C. W. Maynard, TTSP, 15, 135 (1986).
24. W. F. Miller, Jr. and William H. Reed, Nucl. Sci. Eng., 62, (1977).
25. K. D. Lathrop, Nucl. Sci. Eng., 45, 255 (1971).
26. W. L. Filippone and B. D. Ganapol, Trans. Am. Nucl. Soc. 41, 487 (1982).
27. S. Nakamura, Computational Methods in Engineering and Science, Wiley and Sons, 1977.
28. V. Fairen, V. Lopez and L. Cende, am. J. Phys., 1, 57, (1988).
29. B. D. Ganapol, SLEET Code Manual, to be published.
30. B. D. Ganapol, Wing Conference, to be published.
31. B. D. Ganapol, Trans. Am. Nucl. Soc. 42, 161 (1987).
32. B. D. Ganapol, Trans. Am. Nucl. Soc. 42, 165 (1987).

Table 1 Comparison of results obtained for particle streaming through a vacuum from conventional SN without a negative flux fluxup (top), conventional SN with a negative flux fluxup (middle), and the (SCSN) method (bottom).

0.5969	-1.9090	-0.8447	4.4950	3.2910	-1.8850	-5.8360	-6.2310	-3.5440	0.5879
0.0000	0.0000	0.0000	0.0000	0.0000	0.0000	0.0000	0.0000	0.0620	0.8761
0.0000	0.0000	0.0000	0.0000	0.0000	0.0000	0.0000	0.0000	0.0000	0.0000
-1.1090	2.0830	3.5290	-2.6400	-6.5200	-5.3160	-0.9185	4.0300	7.8350	9.9160
0.0000	0.0000	0.0000	0.0000	0.0000	0.0000	0.6327	2.5380	5.2670	7.4550
0.0000	0.0000	0.0000	0.0000	0.0000	0.0000	0.0000	0.4000	2.9630	5.5170
2.0590	-1.1540	-6.6130	-3.8500	2.3190	7.6590	10.6100	11.3100	10.4800	8.8650
0.0000	0.0000	0.0000	0.2299	1.8200	4.9430	7.7710	5.9880	8.7190	7.6130
0.0000	0.0000	0.0000	0.0000	0.0000	1.9050	8.2170	7.6000	7.4070	6.8970
-3.8230	-2.8990	5.7430	11.2000	12.6500	11.3800	9.4600	7.1800	5.1780	3.5970
0.0000	0.7920	3.7750	7.8660	16.0600	9.7690	8.2540	6.4090	4.6970	3.3020
0.0000	0.0000	0.6667	4.7630	8.4210	9.5240	8.6960	8.0000	7.4070	6.8970
7.1010	14.7500	13.6200	10.6100	7.4190	4.9130	3.1400	1.9570	1.1970	0.7218
4.6150	10.9900	11.7600	9.5020	6.8220	4.5920	2.9870	1.8640	1.1470	0.6948
3.6366	9.2310	12.6700	11.7600	10.5366	5.5710	6.0870	4.0000	2.2220	0.6897
15.3800	8.2840	4.4610	2.4020	1.2930	0.6964	0.3750	0.2019	0.1087	0.0585
15.3800	8.2840	4.4610	2.4020	1.2930	0.6964	0.3750	0.2019	0.1087	0.0585
16.3666	10.7700	6.6670	3.5290	1.0530	0.0000	0.0000	0.0000	0.0000	0.0000

Table 3

<u>Iteration</u>	<u>Error</u>	<u>s = 0.01</u>	<u>$\Delta x = 10$</u>
J	x_4	x_6	x_8
2	1.0000E+00	1.0000E+00	1.0000E+00
3	4.4420E-01	4.4420E-01	4.4420E-01
4	2.6199E-01	2.6199E-01	2.6199E-01
5	1.5484E-01	1.7313E-01	1.7313E-01
6	1.1012E-01	1.2155E-01	1.2155E-01
7	7.2856E-02	8.6013E-02	8.8542E-02
8	5.5023E-02	6.4320E-02	6.6086E-02
9	3.8477E-02	4.7013E-02	4.9794E-02
10	2.9833E-02	3.6212E-02	3.8272E-02
11	2.1535E-02	2.6977E-02	2.9283E-02
12	1.6919E-02	2.1105E-02	2.2867E-02
13	1.2459E-02	1.5916E-02	1.7640E-02
14	9.8593E-03	1.2560E-02	1.3902E-02
15	7.3585E-03	9.5515E-03	1.0774E-02
16	5.8465E-03	7.5758E-03	8.5373E-03
17	4.4053E-03	5.7951E-03	6.6351E-03
18	3.5083E-03	4.6101E-03	5.2748E-03
19	2.6621E-03	3.5417E-03	4.1063E-03
20	2.1231E-03	2.8226E-03	3.2710E-03
21	1.6196E-03	2.1754E-03	2.5488E-03
22	1.2928E-03	1.7356E-03	2.0328E-03
23	9.9035E-04	1.3409E-03	1.5848E-03
24	7.9087E-04	1.0705E-03	1.2650E-03
25	6.0768E-04	8.2862E-04	9.8649E-04
26	4.8558E-04	6.6180E-04	7.8778E-04
27	3.7423E-04	5.1300E-04	6.1441E-04
28	2.9900E-04	4.0983E-04	4.9080E-04
29	2.3092E-04	3.1805E-04	3.8280E-04
30	1.8452E-04	2.5412E-04	3.0584E-04
31	1.4276E-04	1.9739E-04	2.3854E-04
32	1.1408E-04	1.5773E-04	1.9061E-04
33	8.8389E-05	1.2260E-04	1.4866E-04
34	7.0365E-05	9.7975E-05	1.1880E-04
35	5.4790E-05	7.6201E-05	9.2649E-05

$\Delta x = 10$

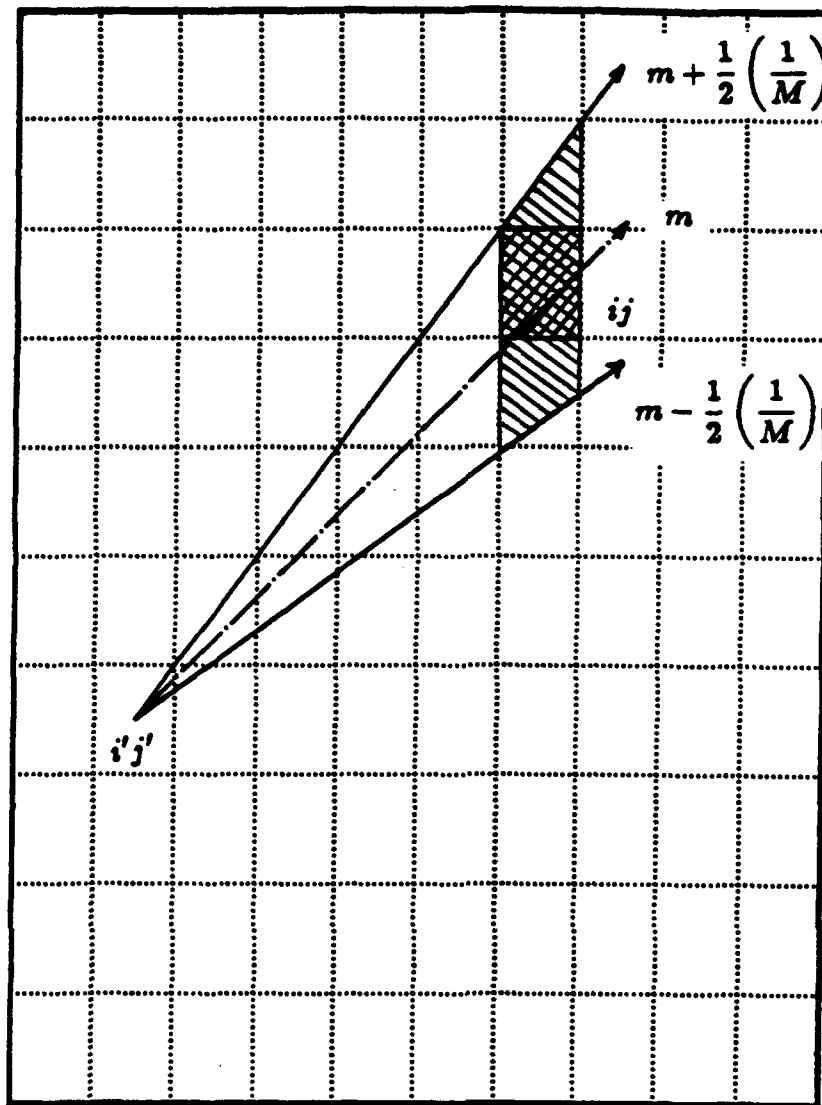


Figure 1. Angular cone construction for $i > i' + 1$. Cross hatched area is the extended region of influence for direction m . Double cross hatched area is that fraction within the target cell ij .

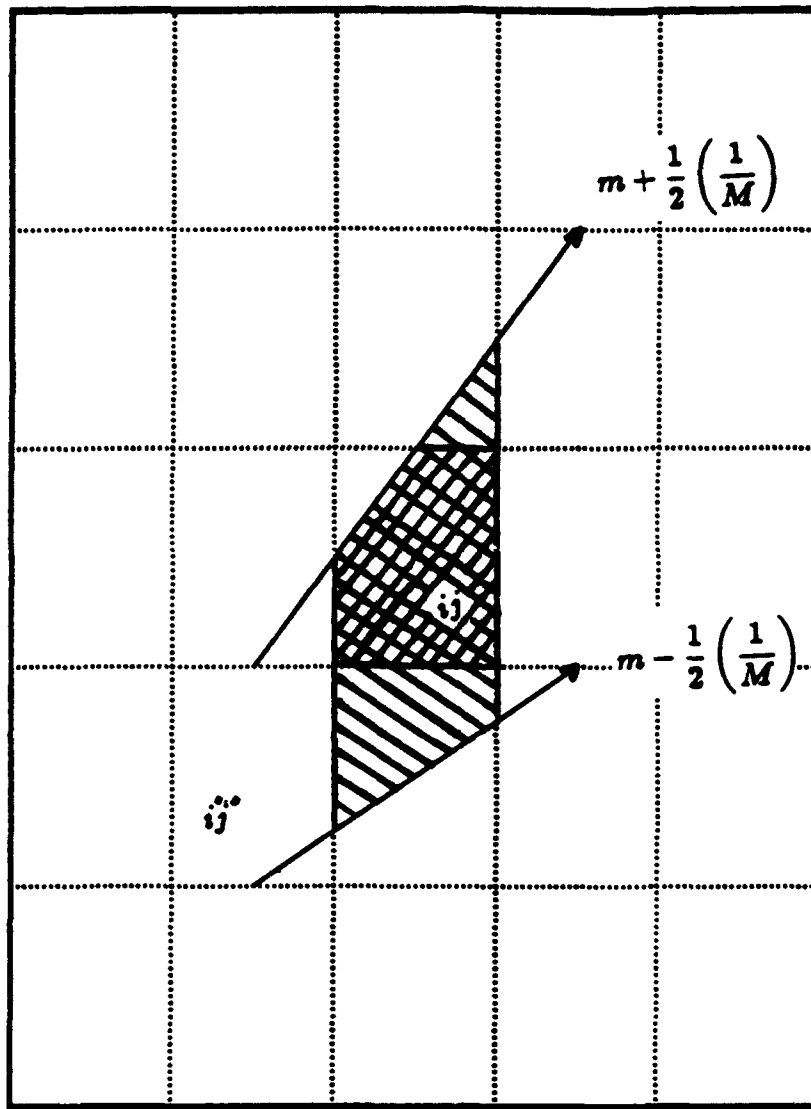


Figure 2. Angular cone construction for $i \leq i' + 1$. Cross hatched area is the extended region of influence for direction m . Double cross hatched area is that fraction within the target cell i_j .

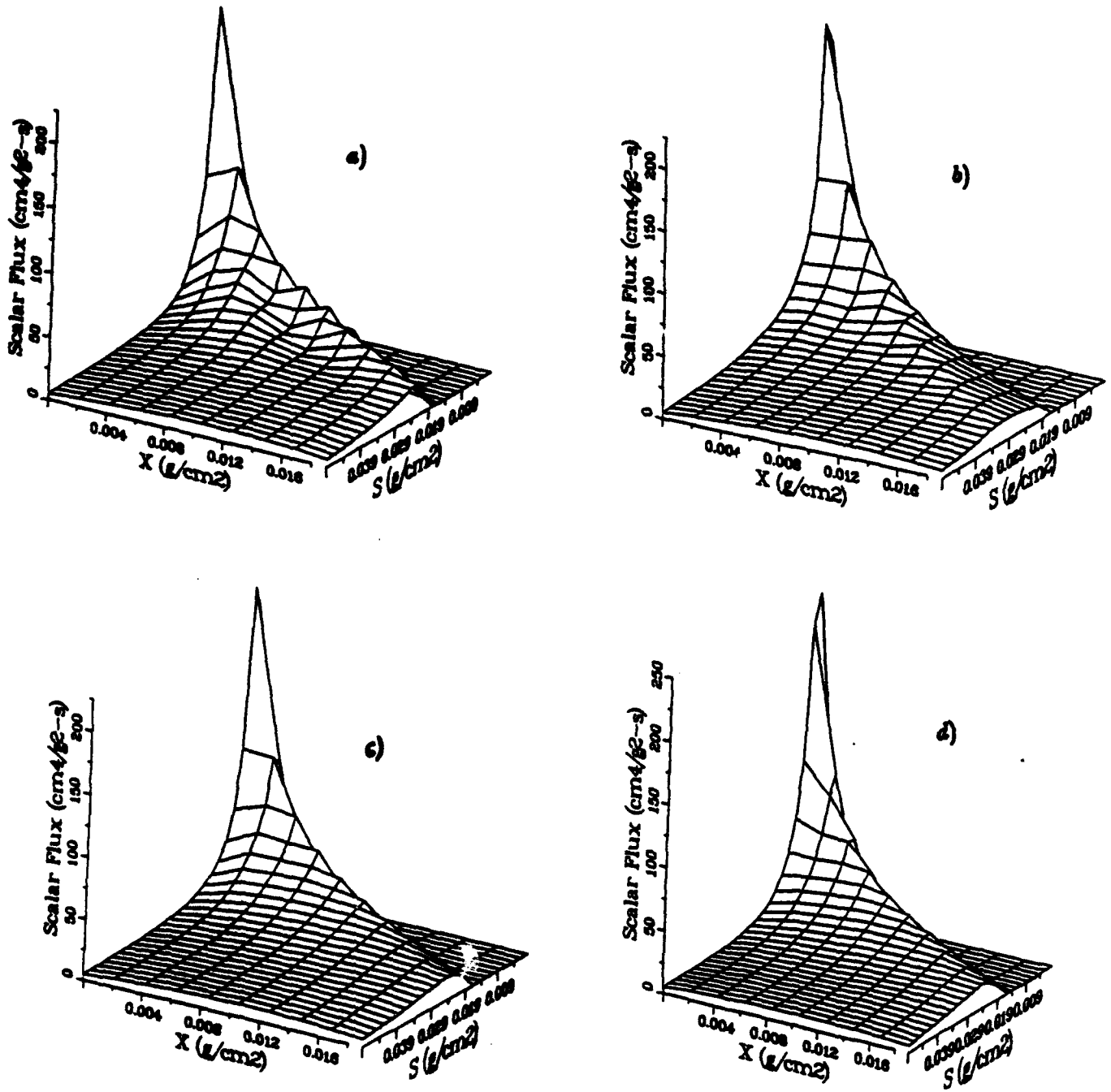


Figure 3 Comparison of solutions obtained from the conventional S_N (DD) method and the (SCSN) method for coarse (37 mfp) mesh cells. a) (DD) $M = 4$, b) (SCSN) $M = 4$, c) (DD) $M = 12$, d) (SCSN) $M = 12$.

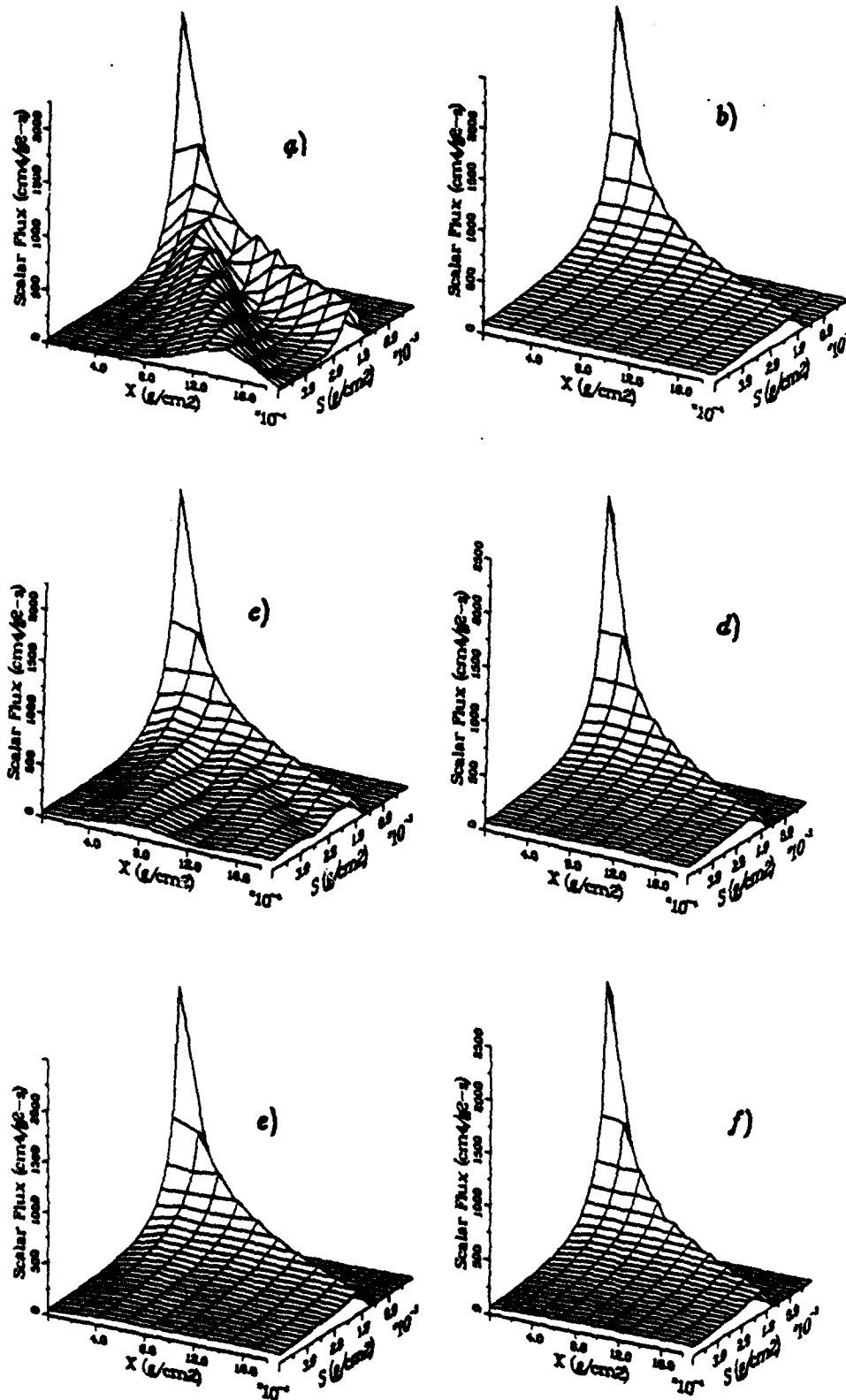


Figure 4 Comparison of solutions obtained from the conventional S_N (DD) method and the new (SCSN) method for fine (3.7 mfp) mesh cells. a) (DD) $M = 4$, b) (SCSN) $M = 4$, c) (DD) $M = 8$, d) (SCSN) $M = 8$, e) (DD) $M = 12$, f) (SCSN) $M = 12$.

Table 4

Approach to "Steady State" $\phi(x) = 0.11318$

<u>Δs</u>	<u>s</u>	<u>$\phi(0,s)$</u>	<u>ERROR</u>
0.01	0.5	0.11229	7.9×10^{-3}
0.02	1.0	0.11277	3.62×10^{-3}
0.04	2.0	0.10913	3.58×10^{-3}
0.08	4.0	0.09972	1.19×10^{-1}

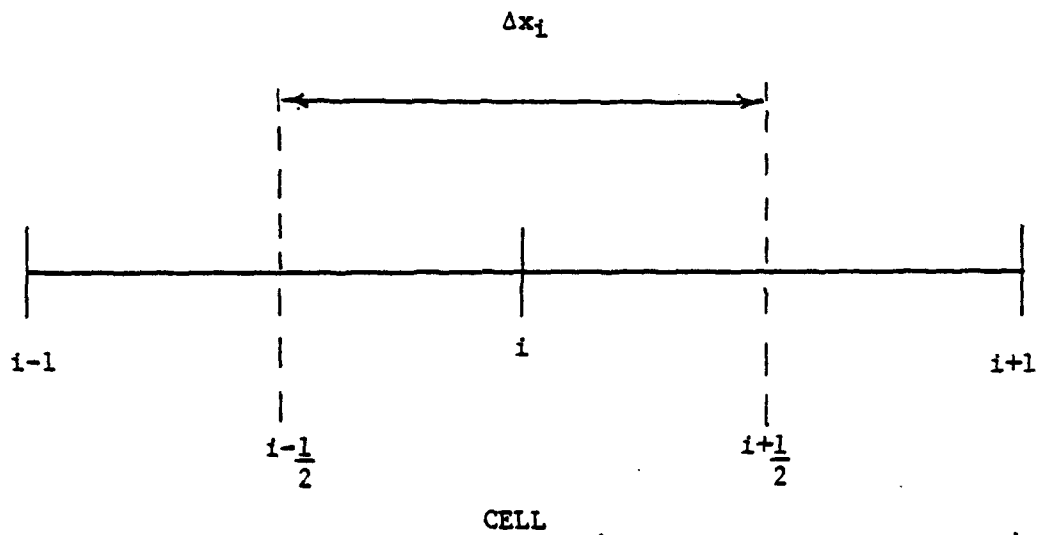


Fig. 5 1-D cell for point spatial finite difference scheme

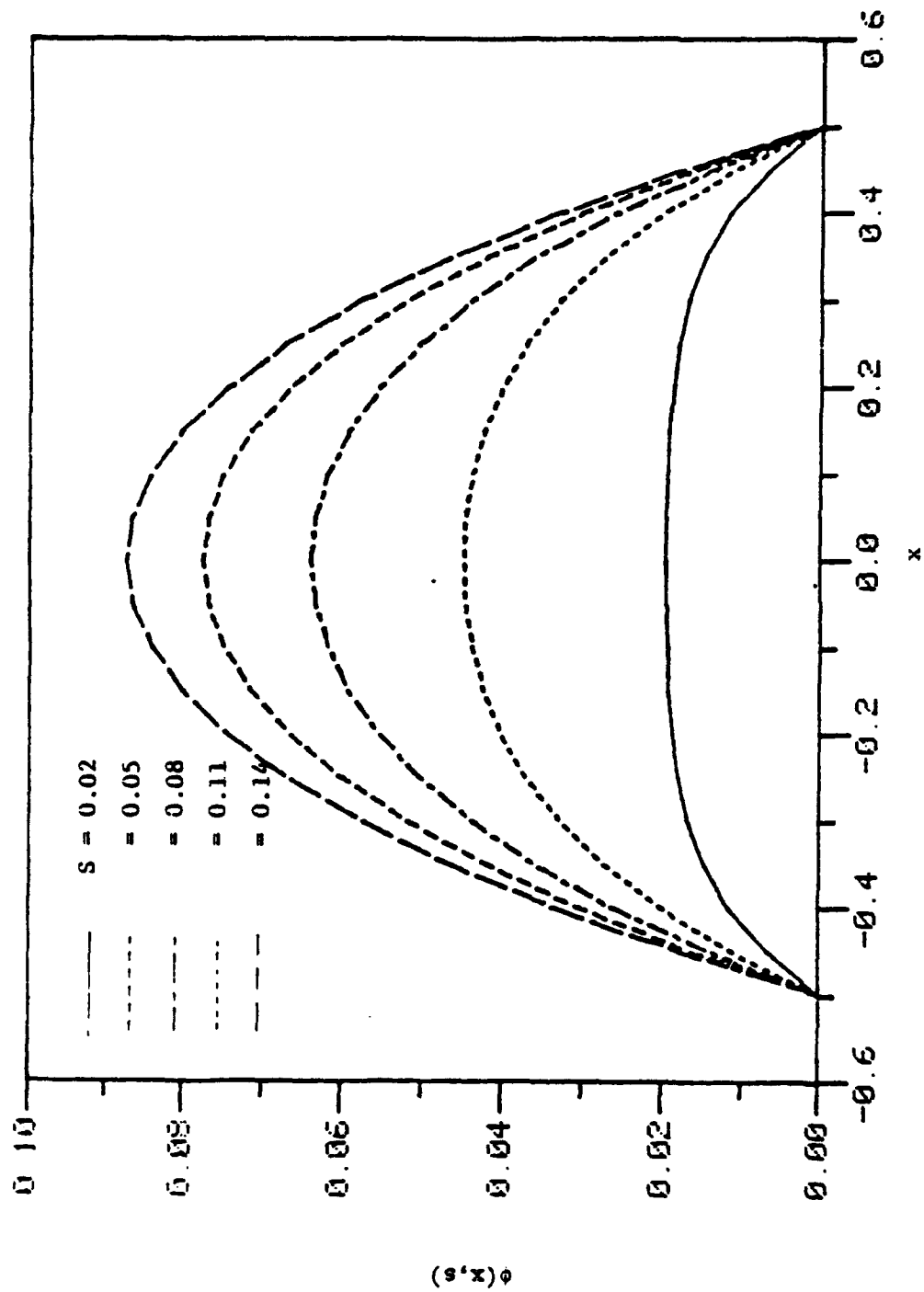


Fig. 6a Spatial flux profile development for source drive benchmark

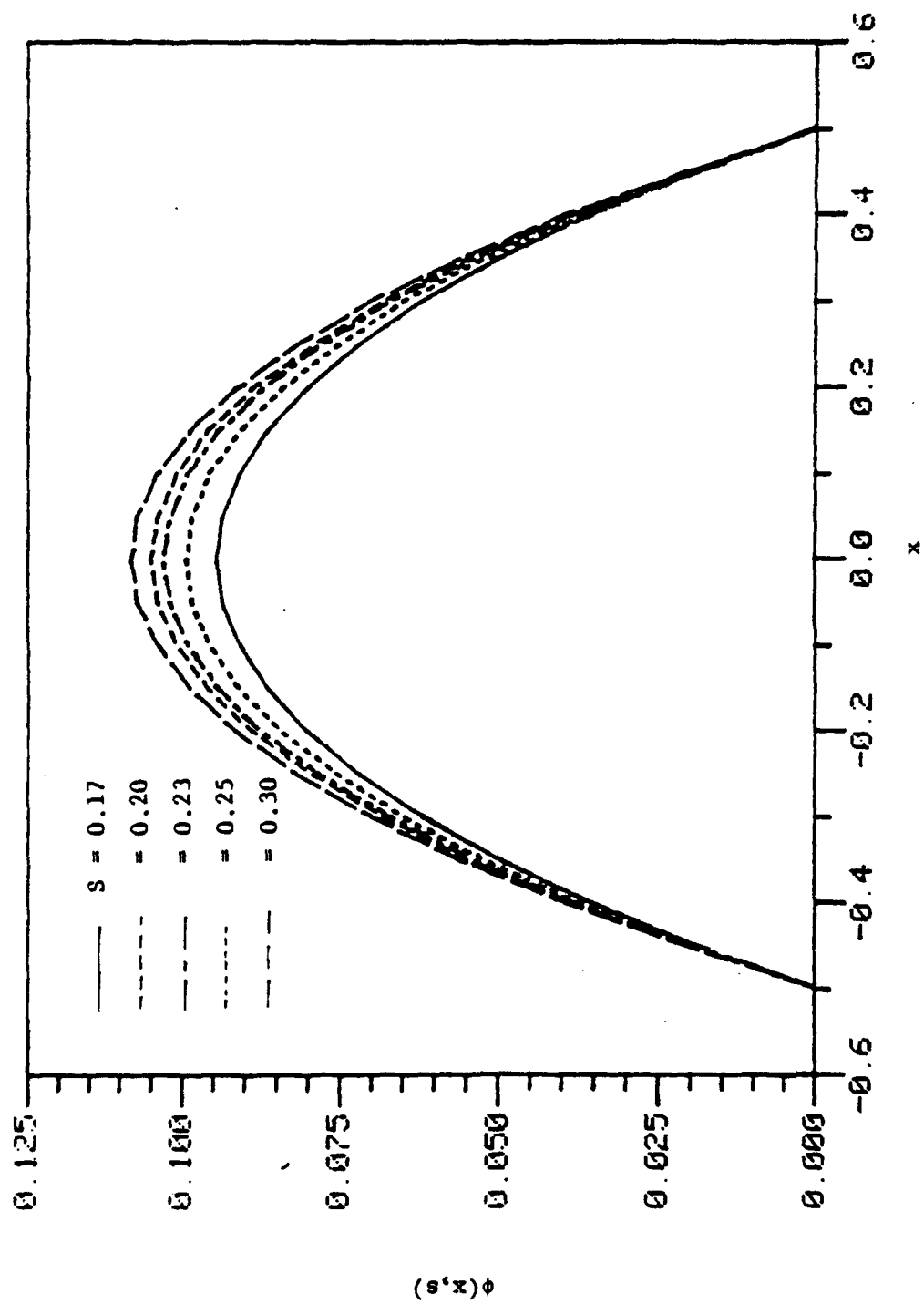


Fig. 6b Spatial profile development continued

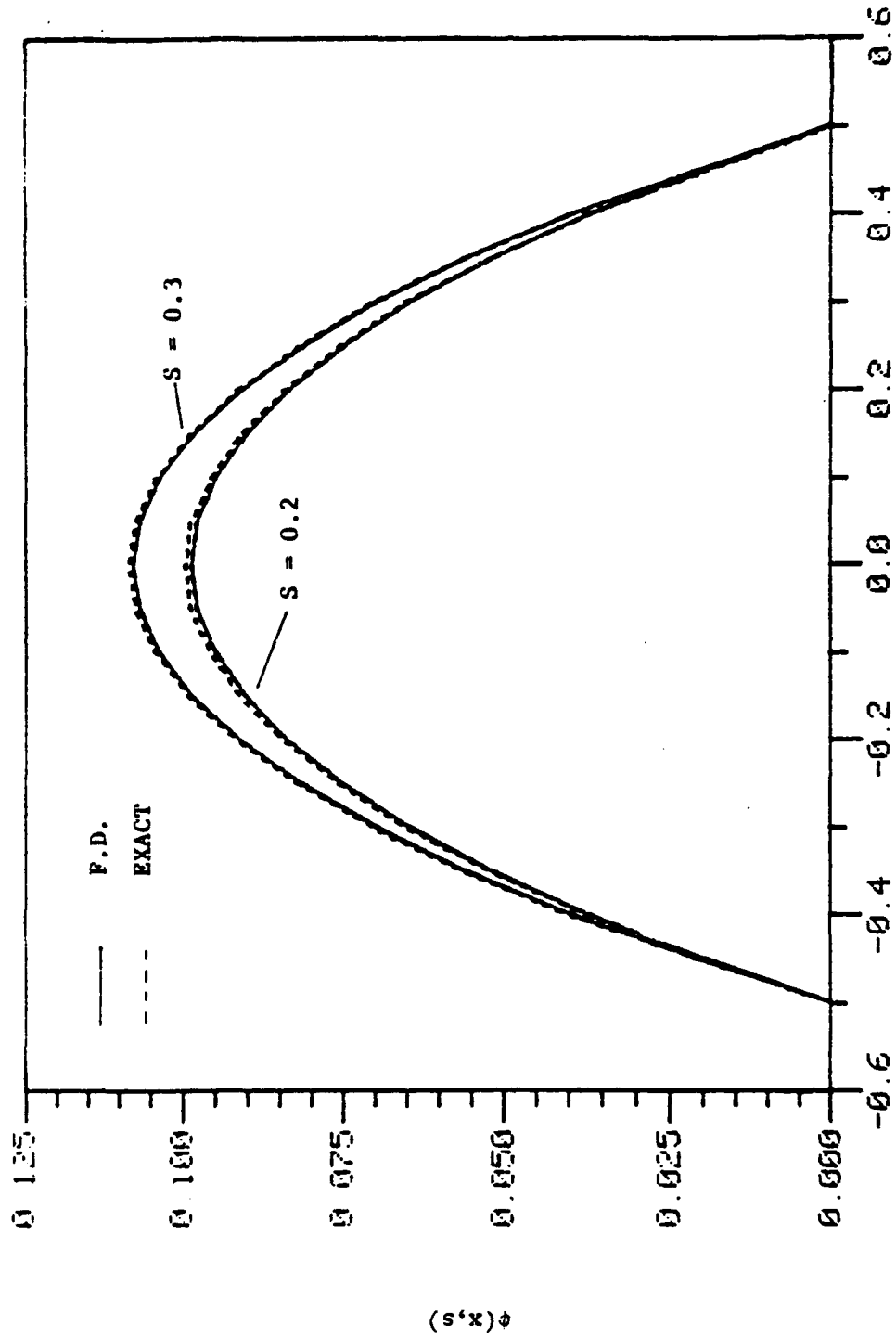


Fig. 6c Comparison with EXACT solution ($\Delta s = 0.01$, $\Delta x = 0.05$)

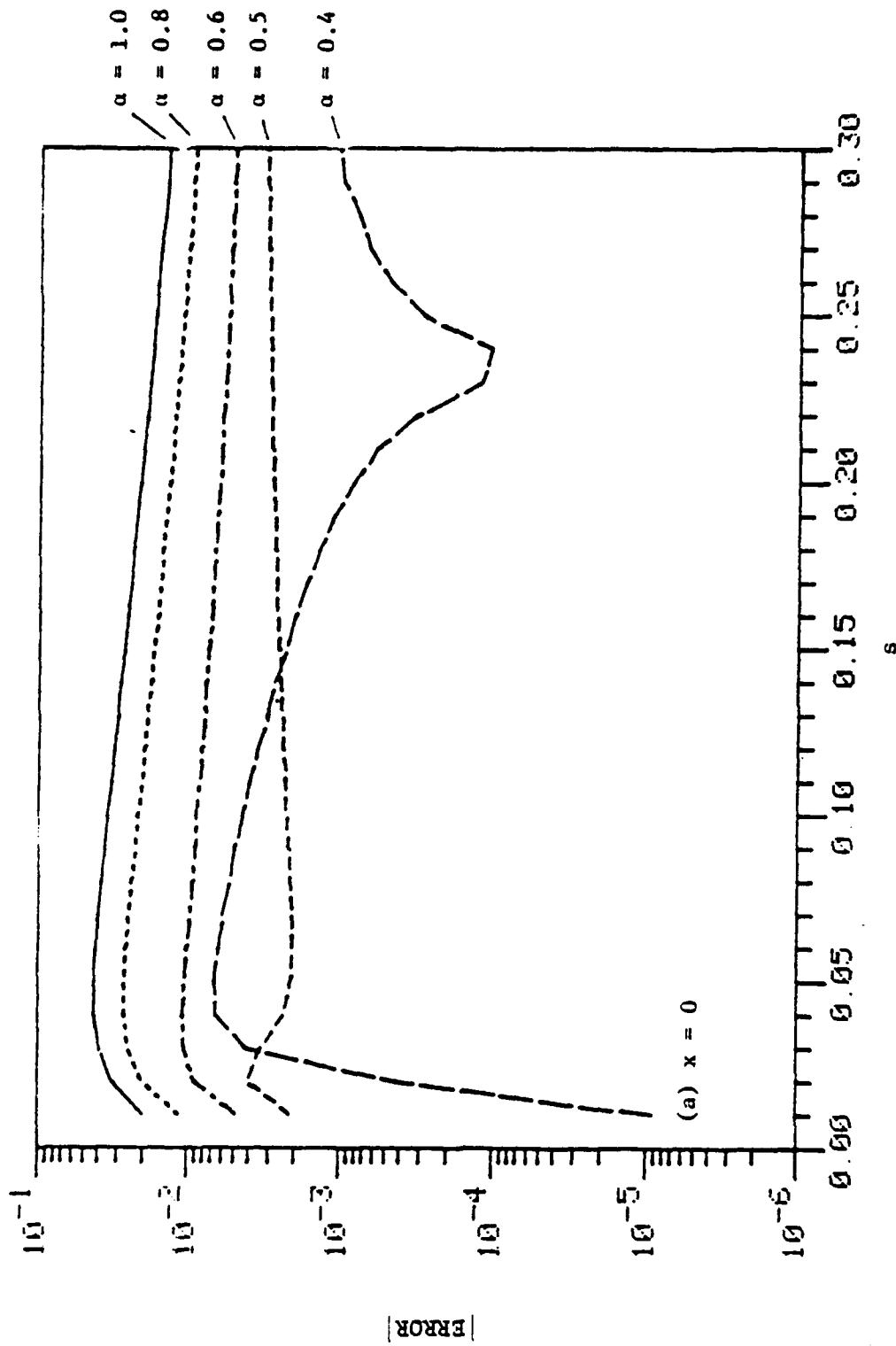


Fig. 7 a Comparison for different α 's ($\Delta s = 0.01$, $\Delta x = 0.05$) for (a) $x = 0$ and (b) $x = 0.25$

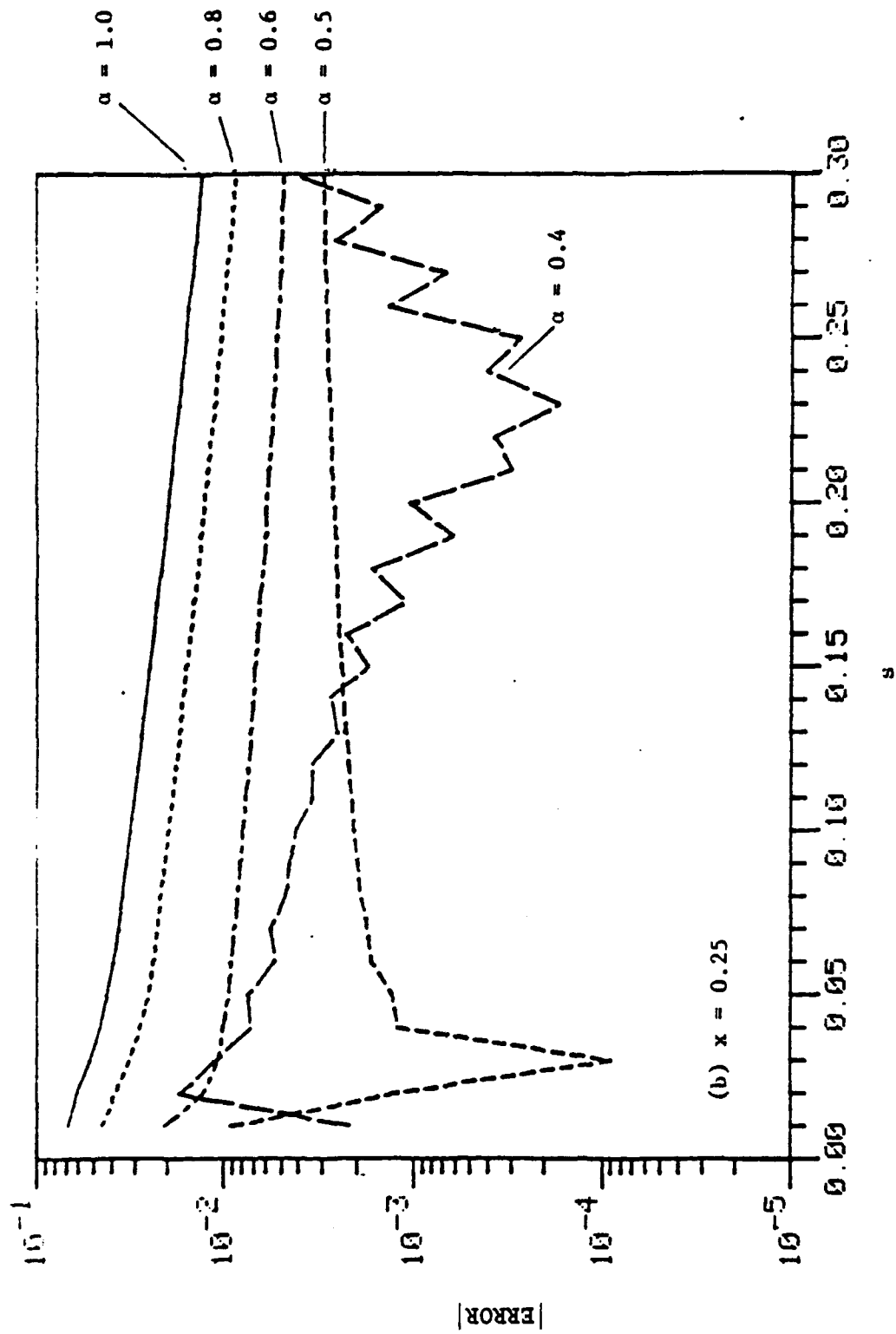


Fig. 7b $x = 0.25$

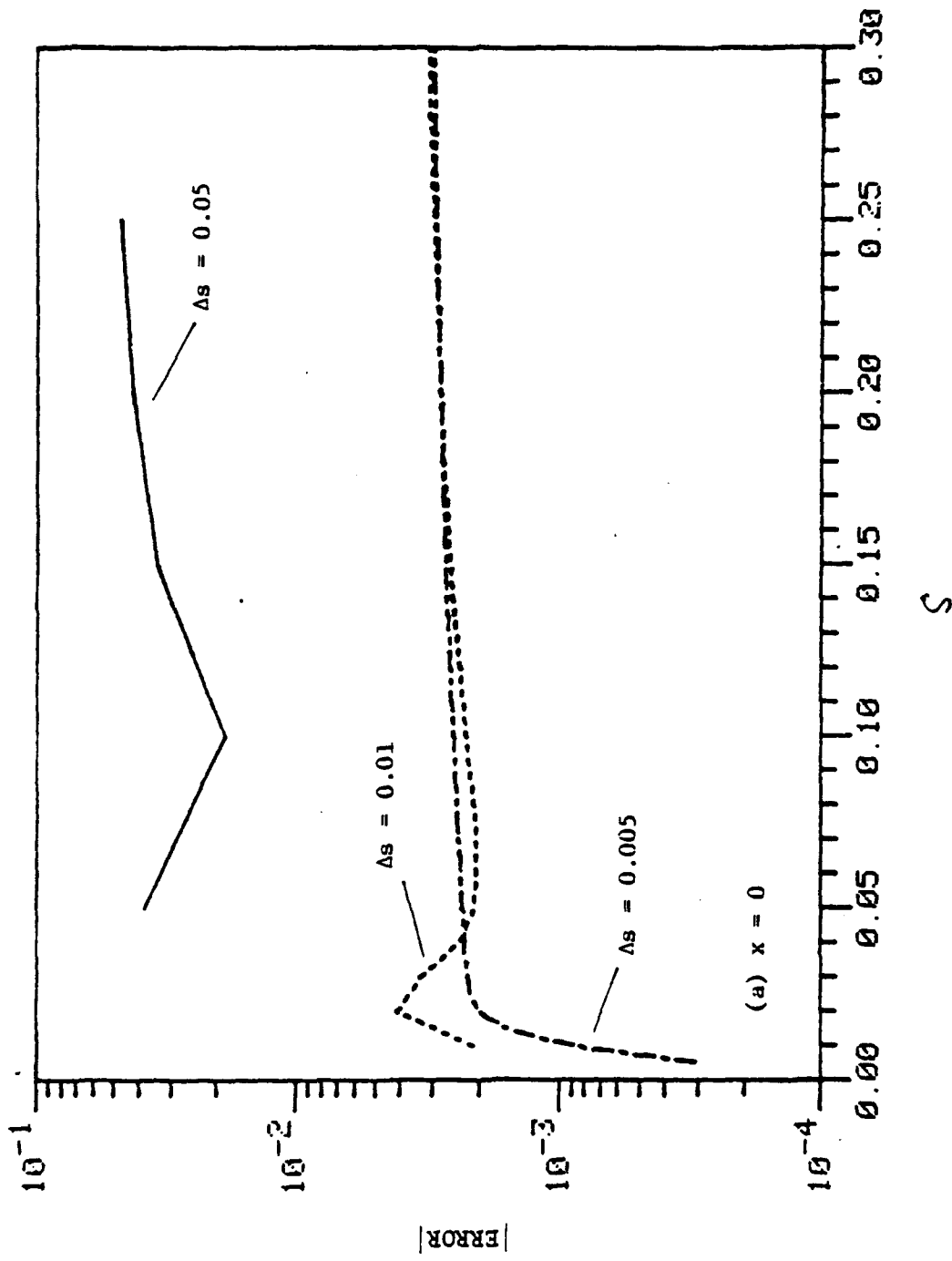


Fig. 8a Comparison for different Δs 's ($\alpha = 0.5$, $\Delta x = 0.05$) (a) $x = 0$, (b) $x = 0.25$

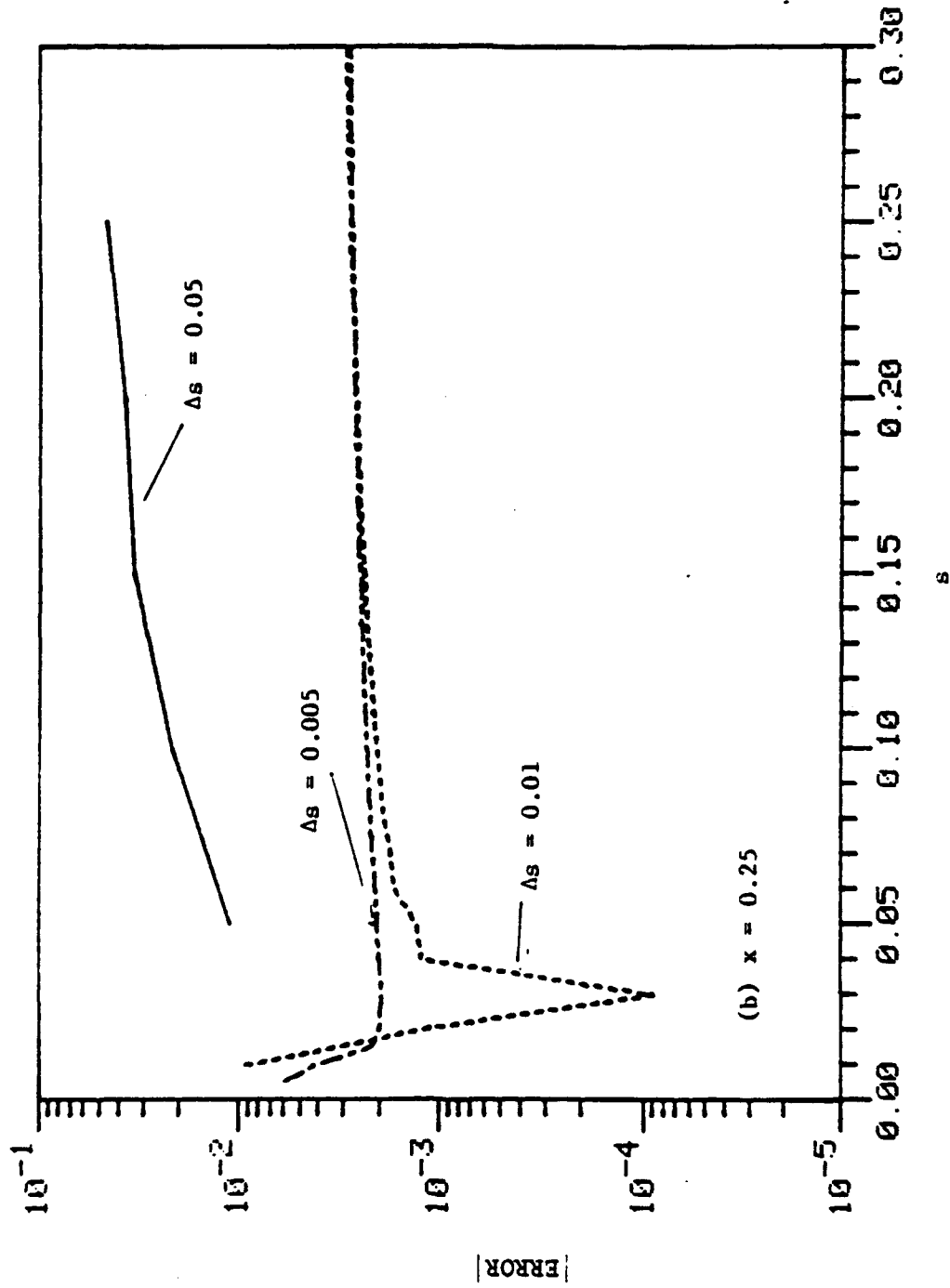


Fig. 8b $x = 0.25$

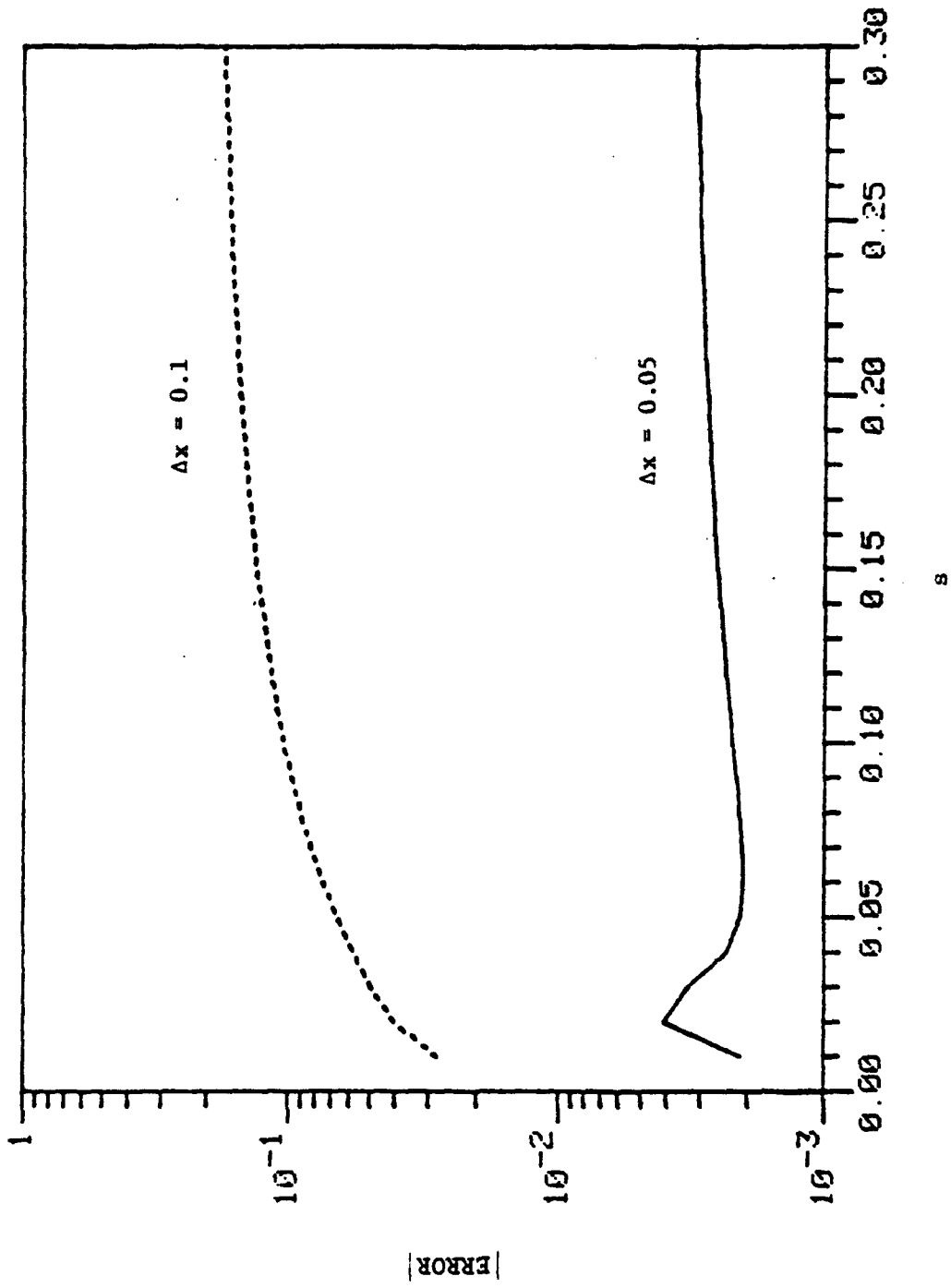


Fig. 9 Variation for different Δx 's ($\Delta s = 0.01$, $\alpha = 0.5$)

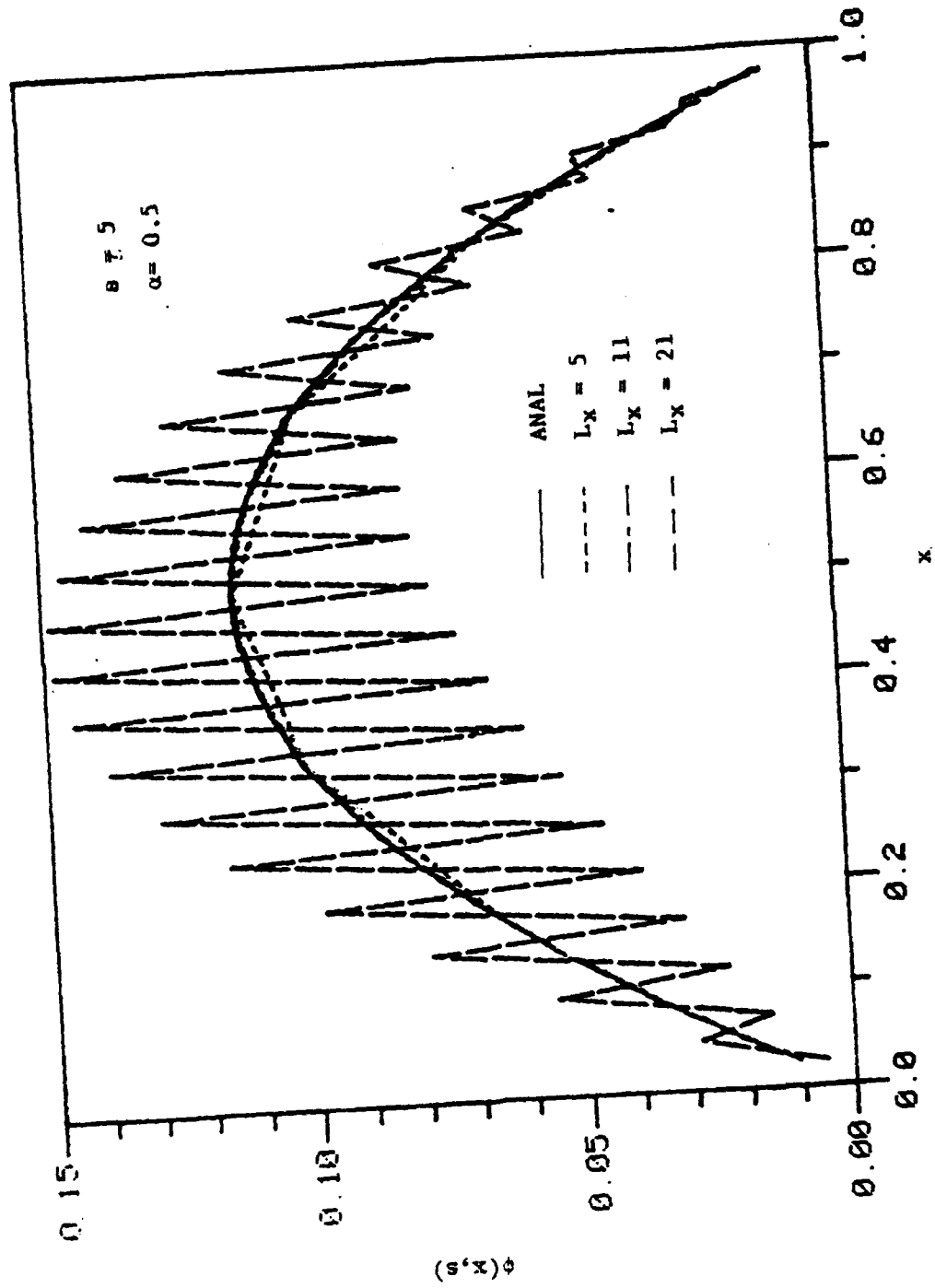


Fig. 10a Variation of Δx : Iteration - source driven benchmark

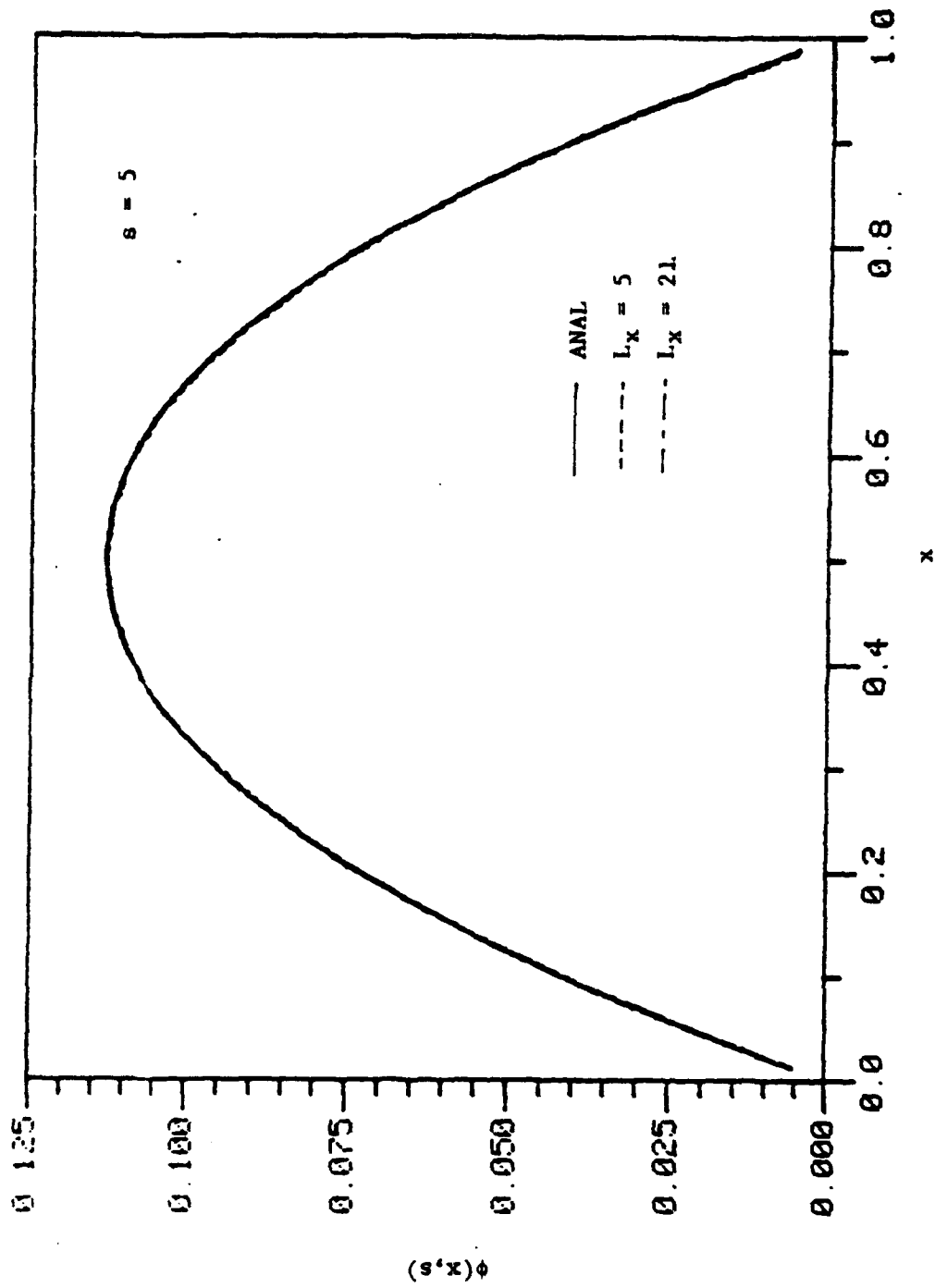


Fig. 10b Variation of Δx : Tridiagonal - source driven benchmark

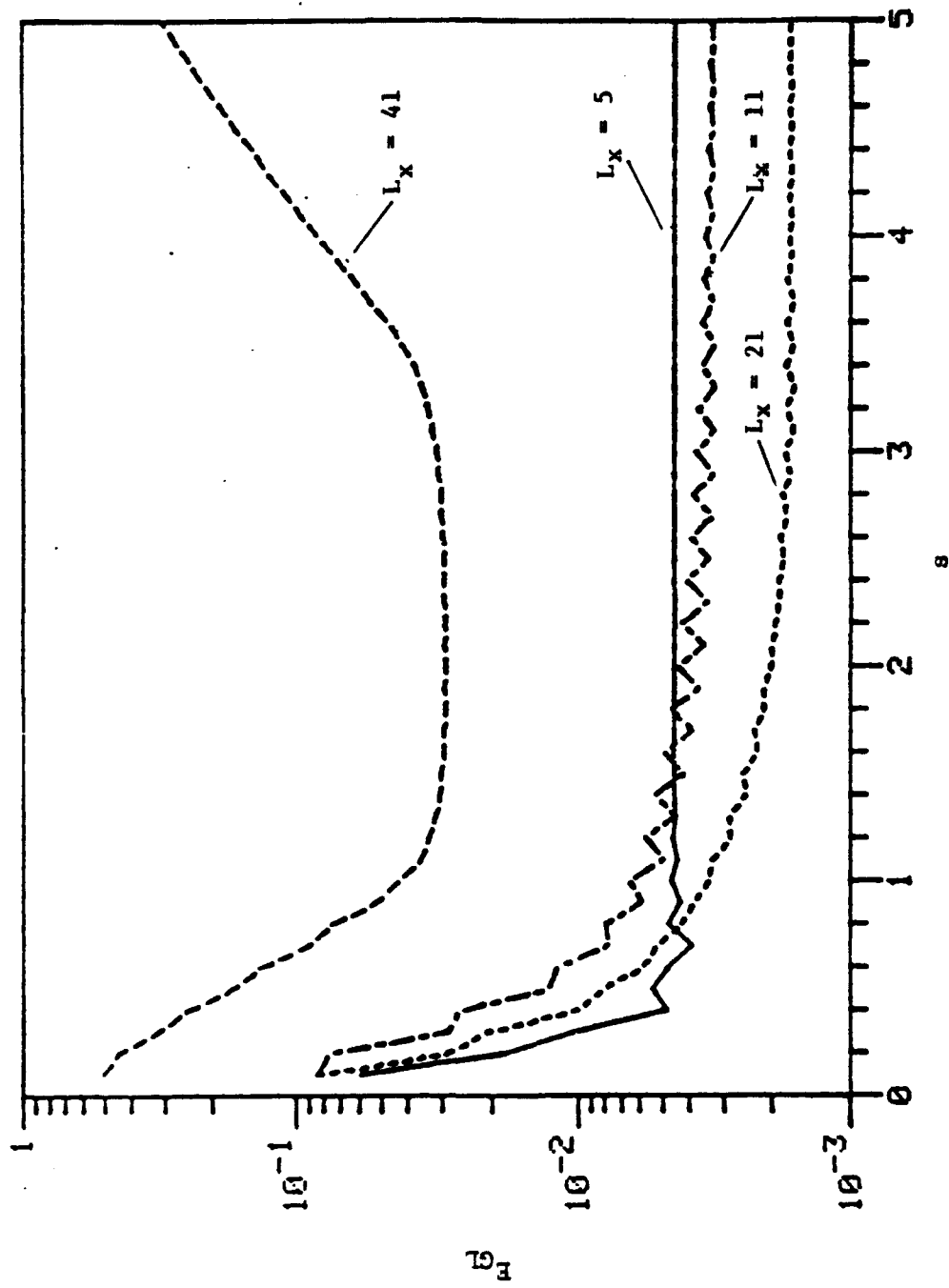


Fig. 11a Global error comparison with Prob 1: Iteration

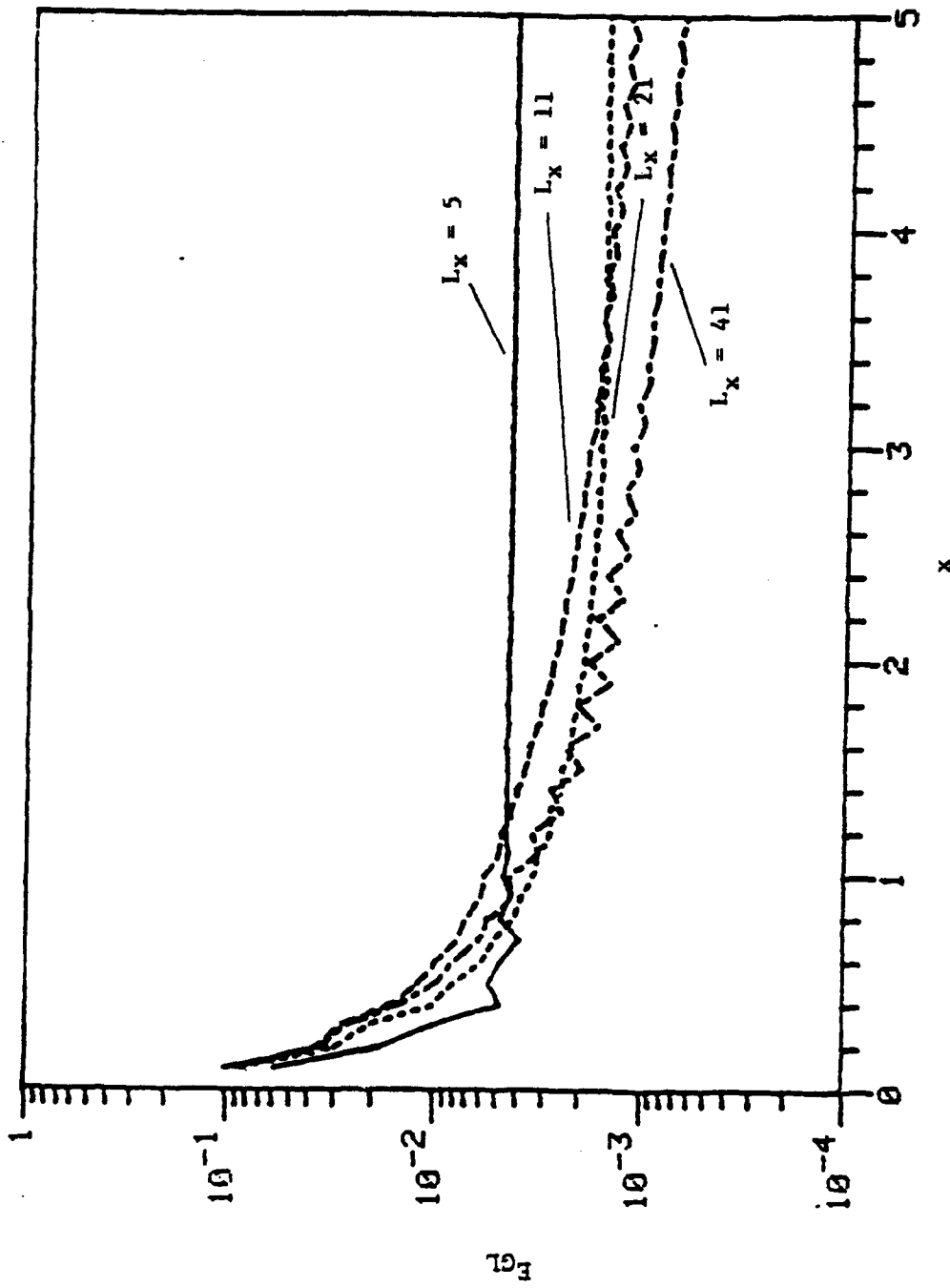


Fig. 11b Global error comparison with Prob 1: Tridiagonal

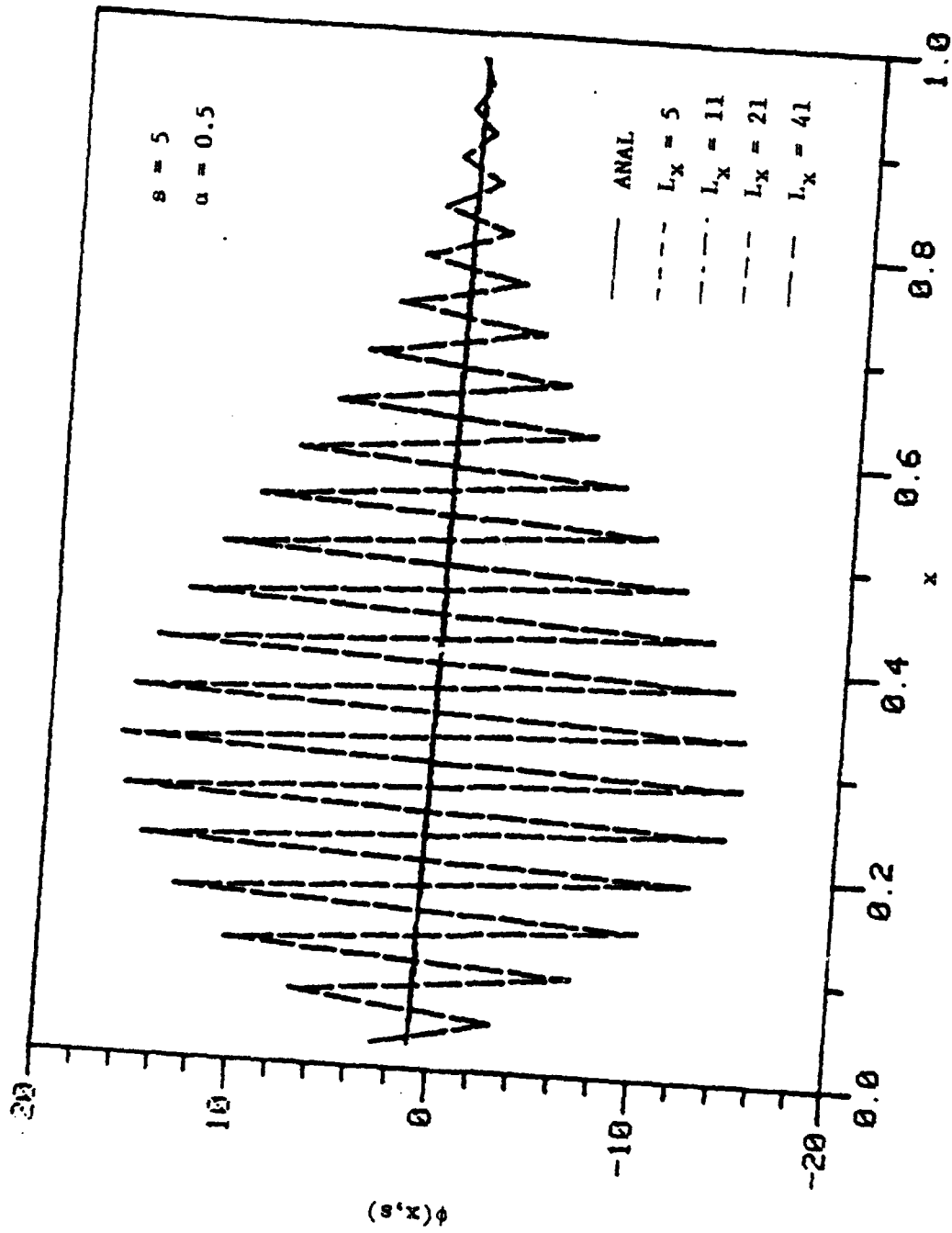


Fig. 12a Variation of Δx : Iteration - Prob 2

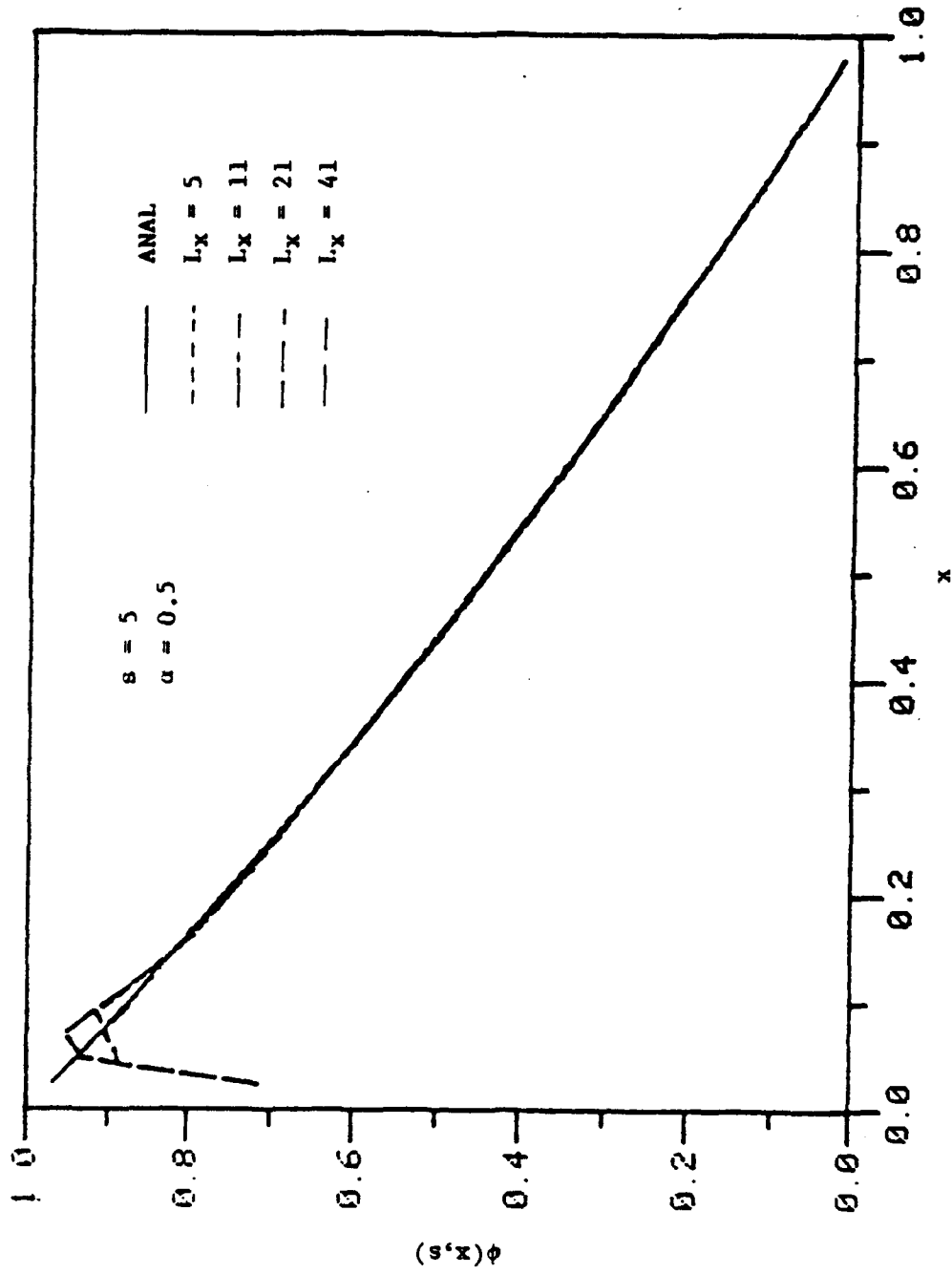


Fig. 12b Variation of Δx : Tridiagonal - Prob 2

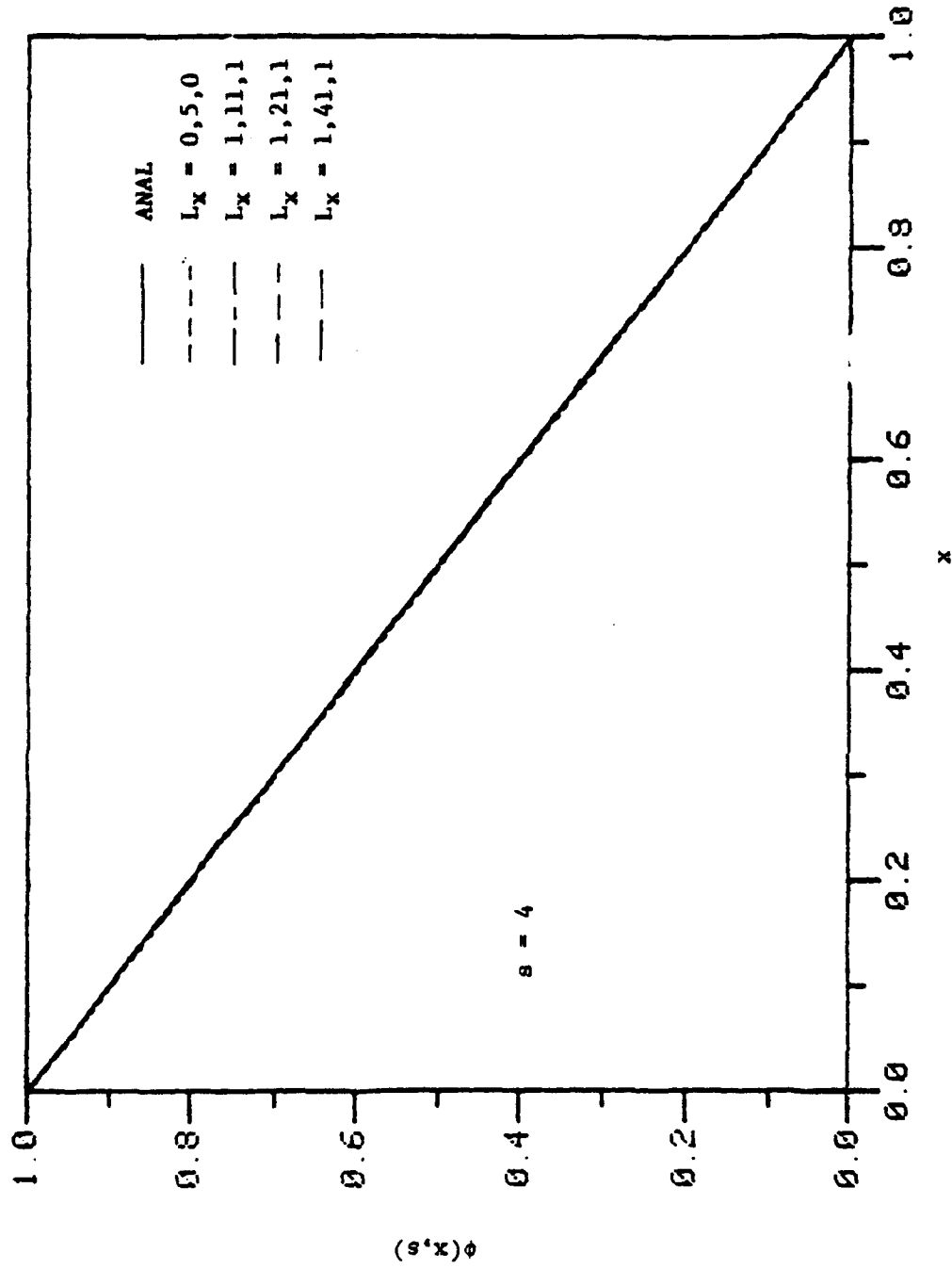


Fig. 12c Improvement with additional interval at boundary: Tridiagonal - Prob b

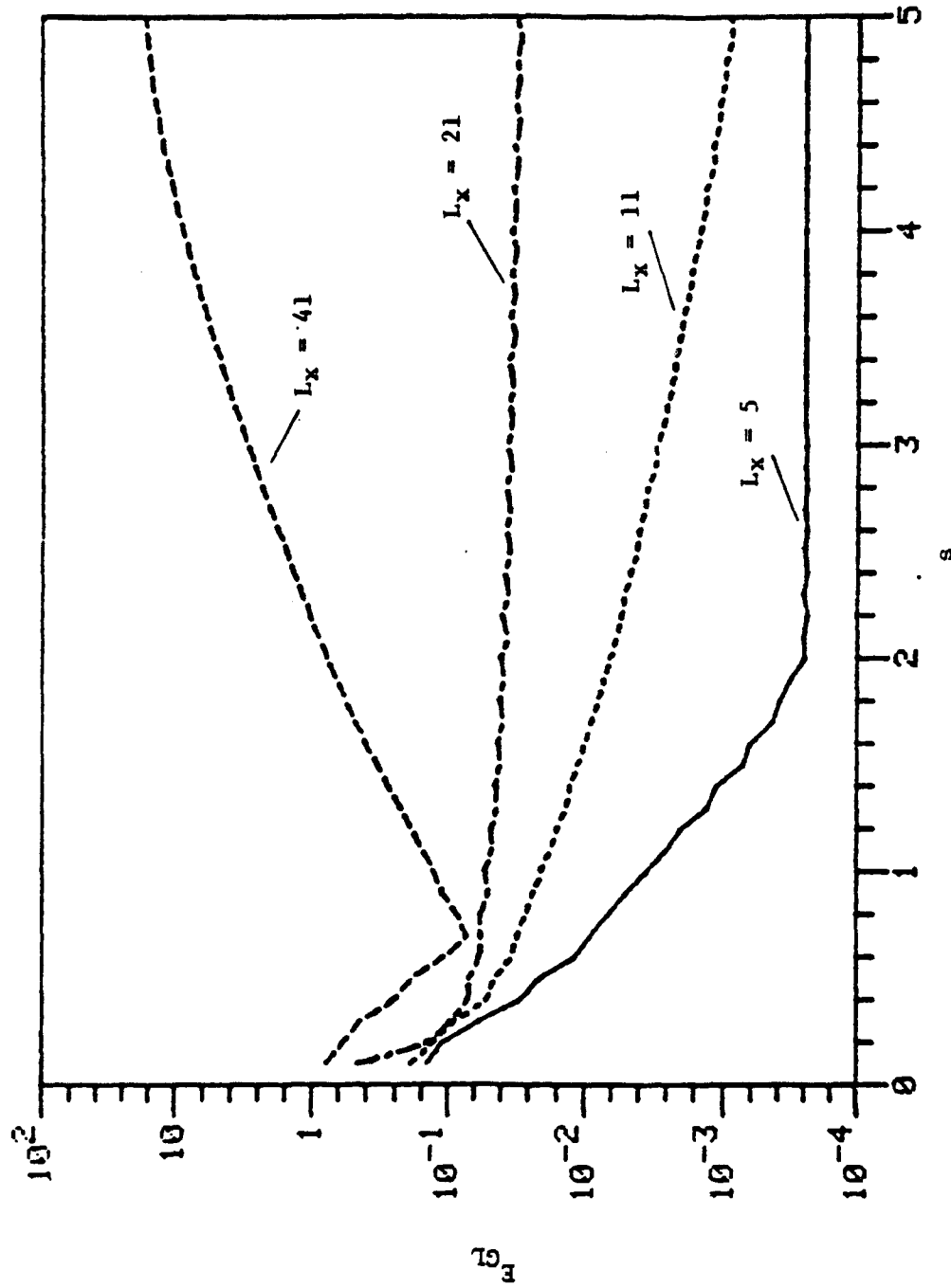


Fig. 13a Global error comparison with Prob 2: Iteration

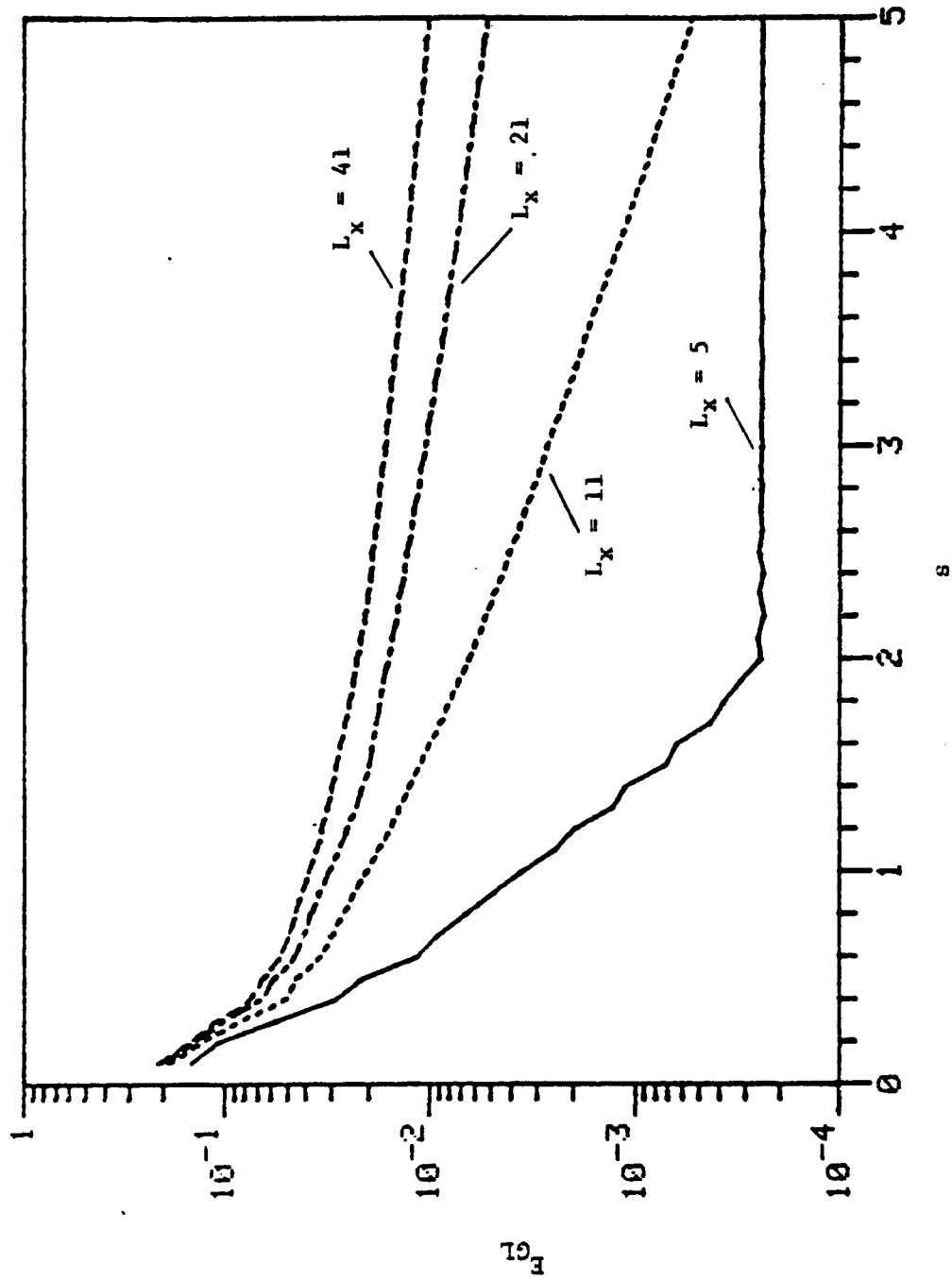


Fig. 13b Global error comparison with Prob 2: Tridiagonal

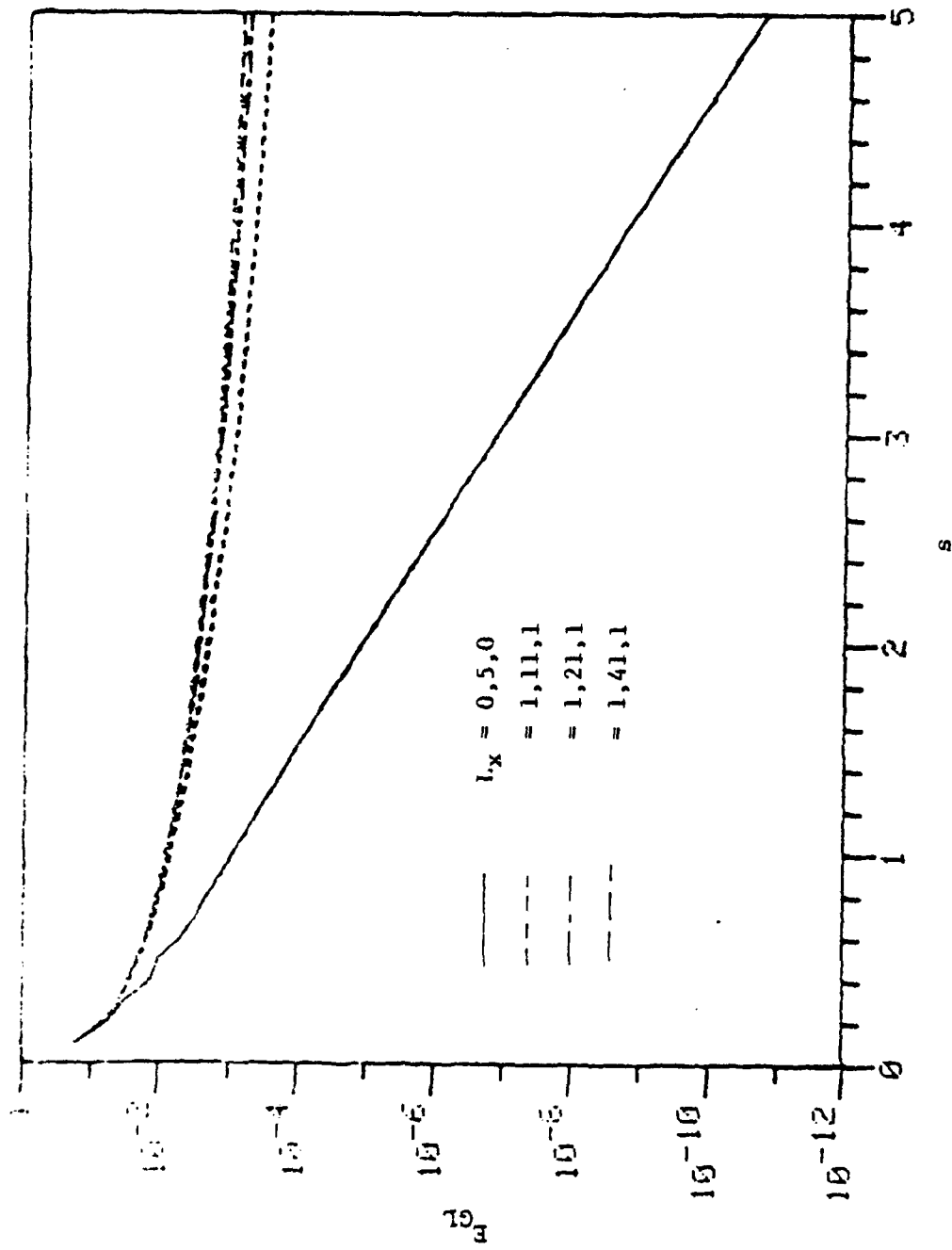


Fig. 13c Global error: Tridiagonal - Prob 2

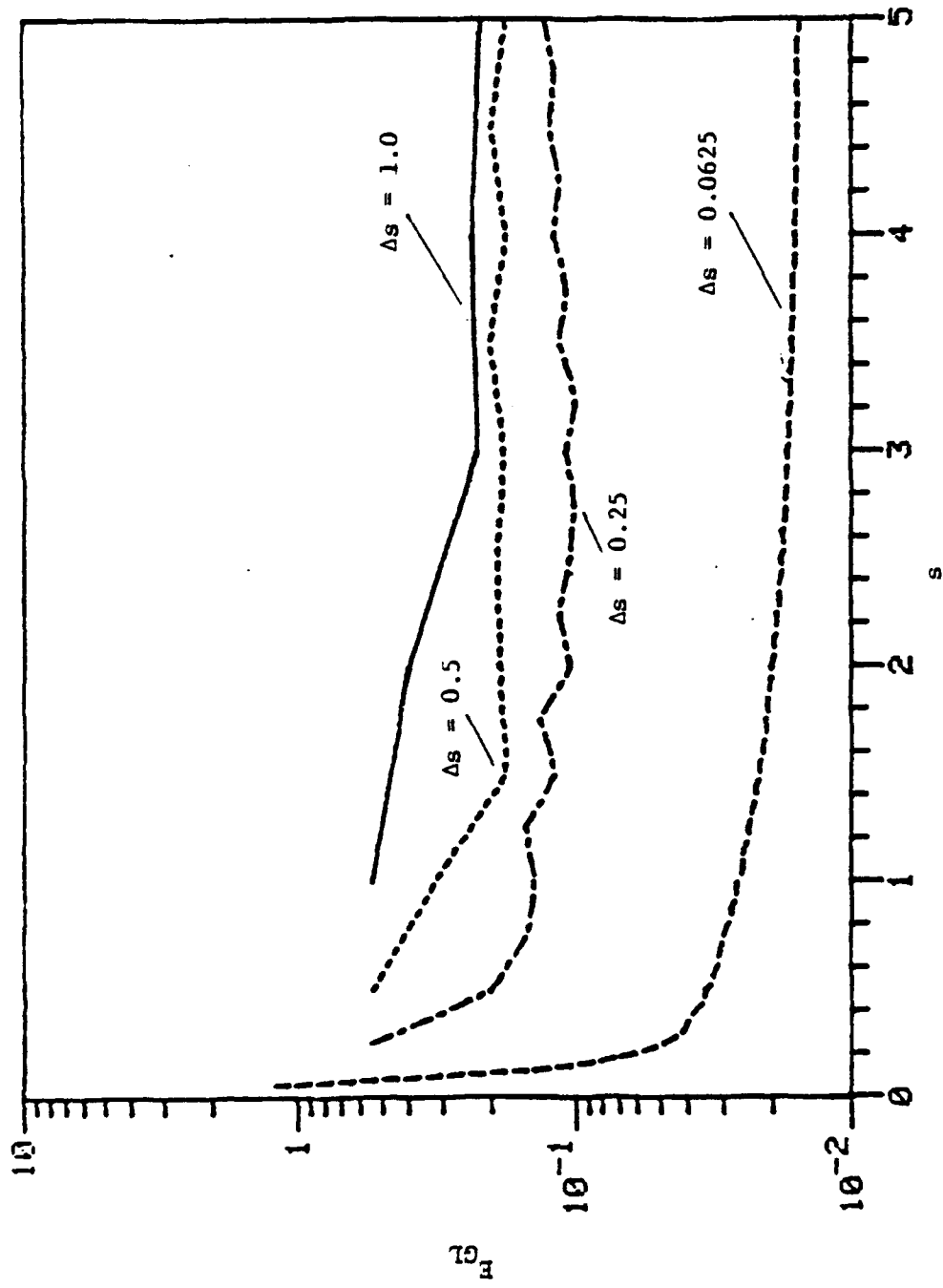


Fig. 14a Variation of Δs : Iteration - Prob 2

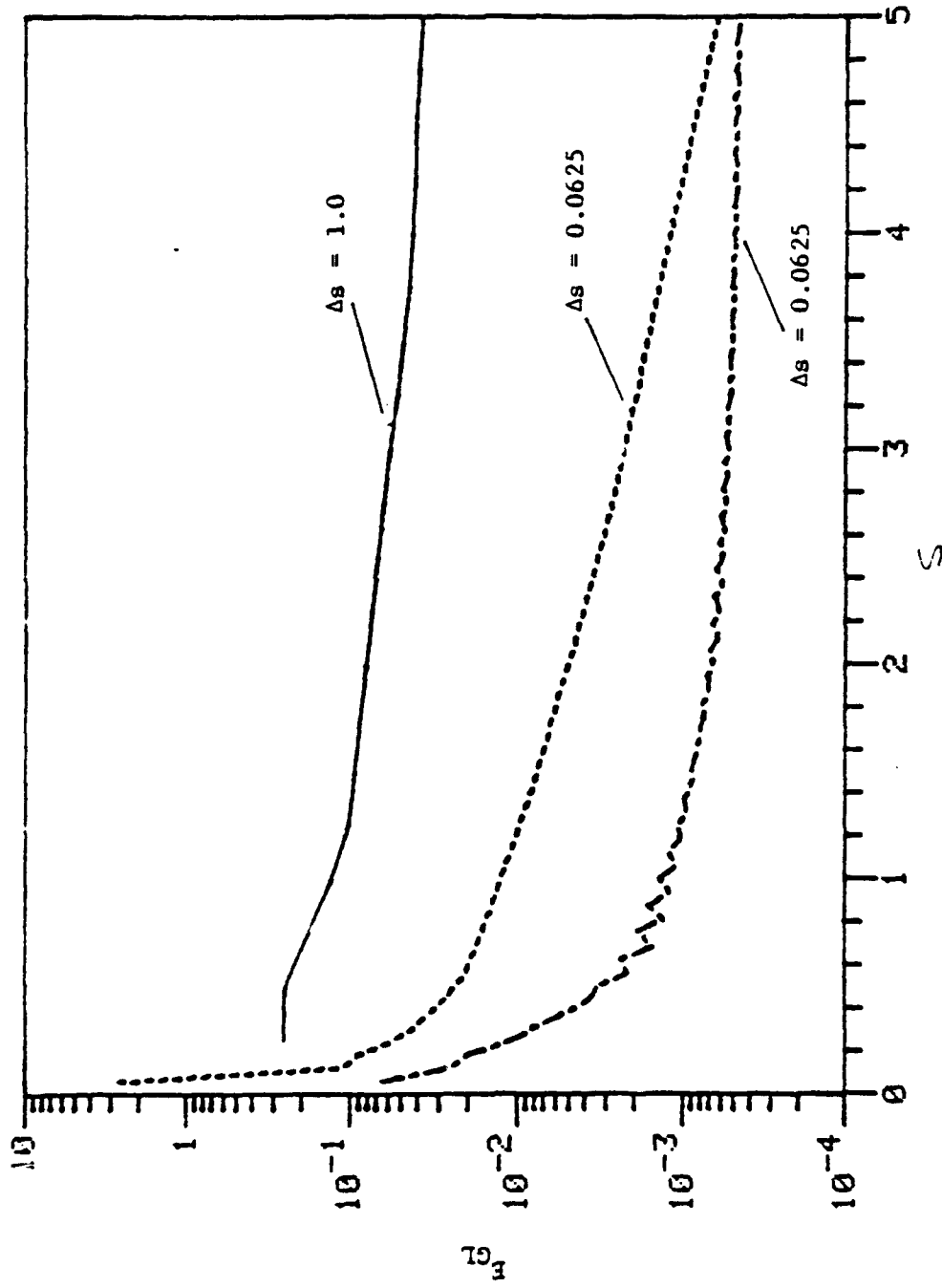


Fig. 14b Variation of Δs : Tridiagonal

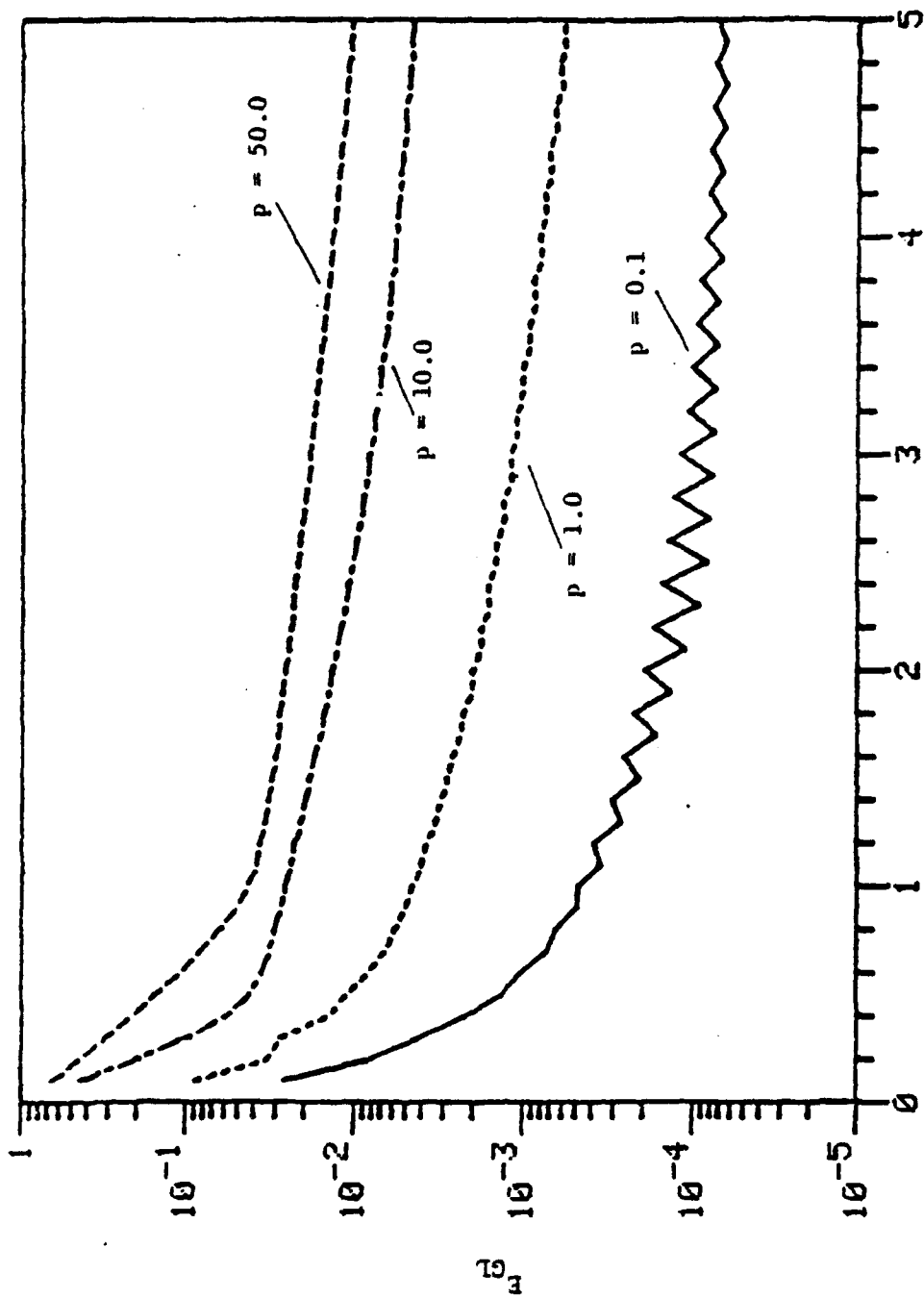


Fig. 15 Variation of diffusion coef: Tridiagonal - Prob 1

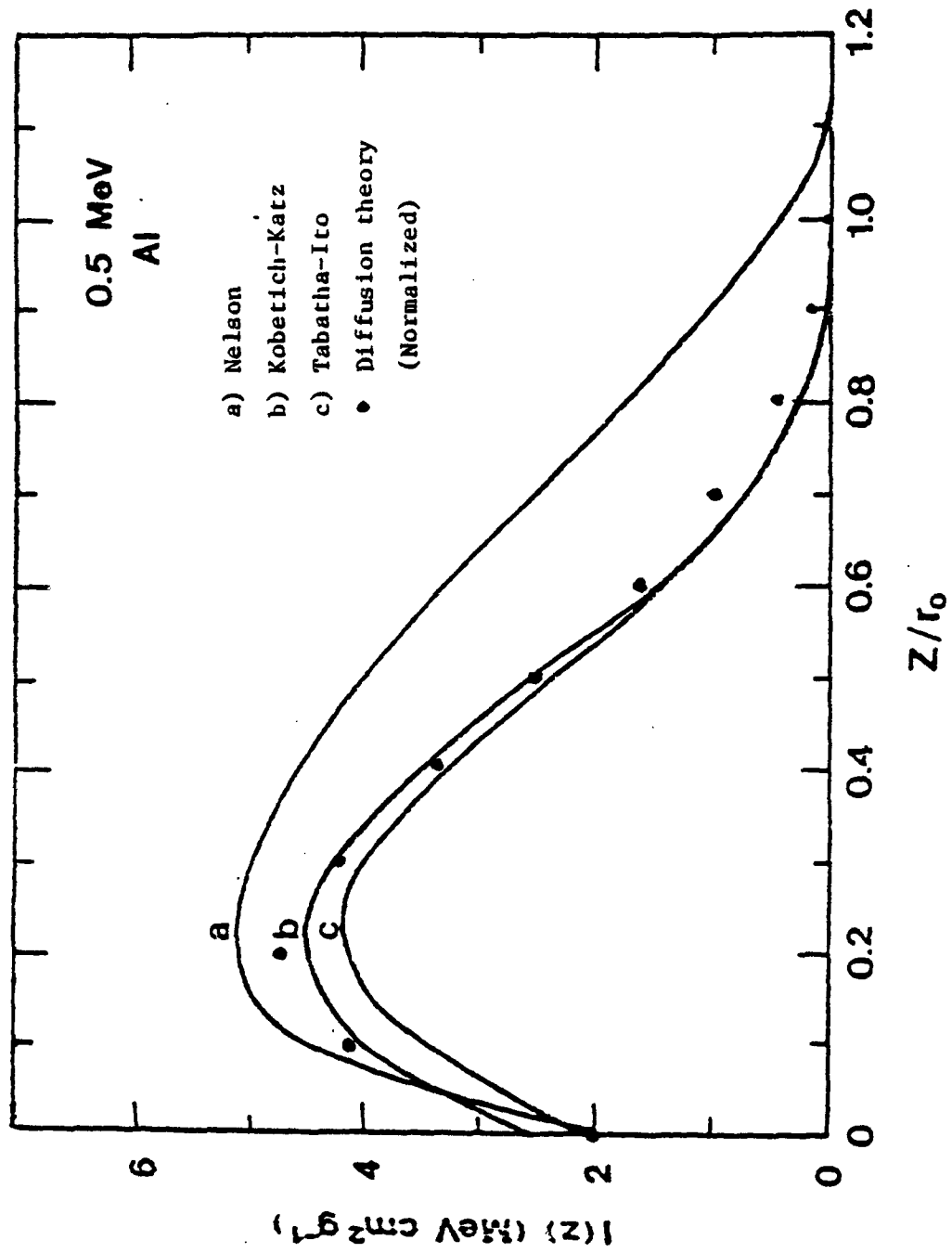


Fig. 16 Dose comparison in aluminum

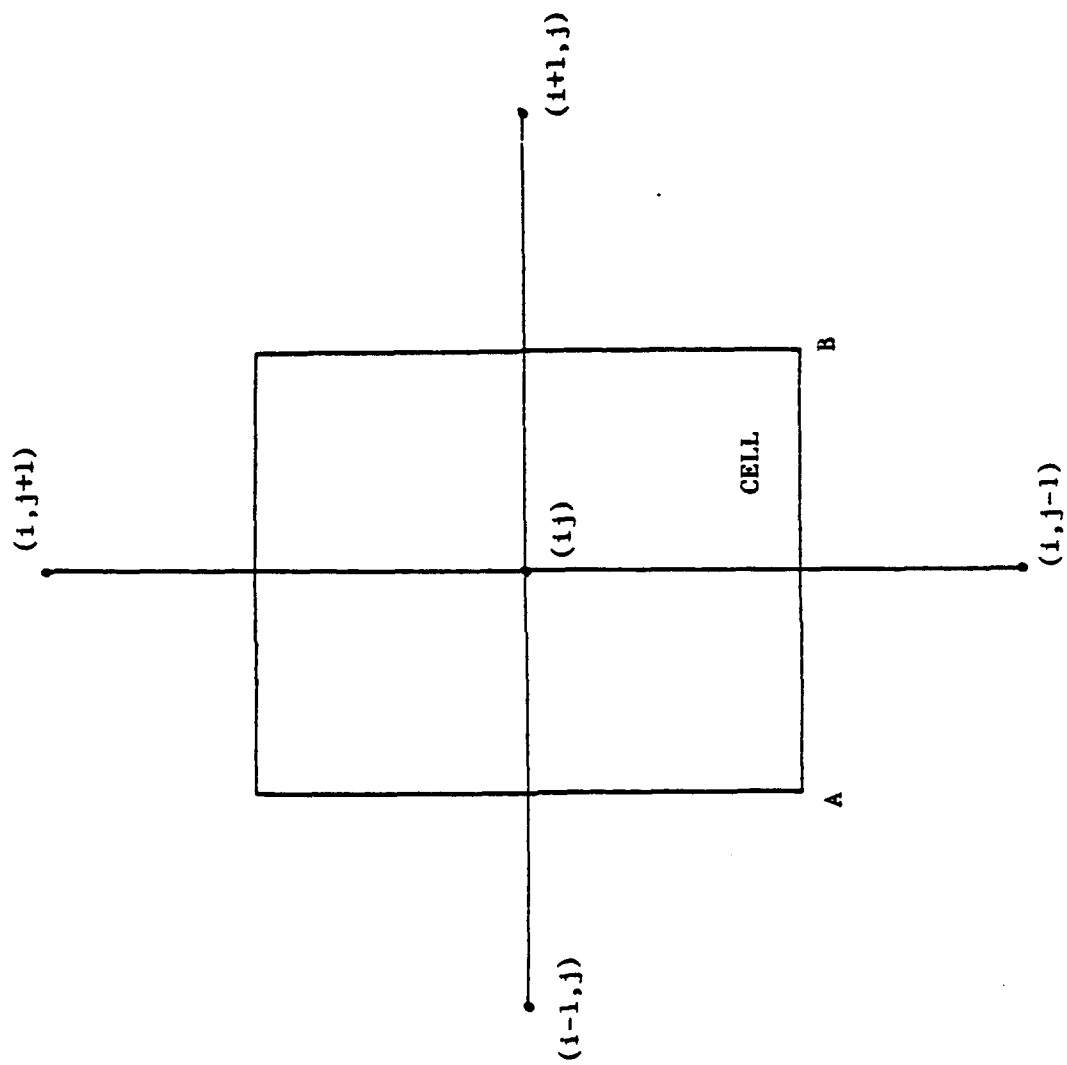


Fig. 17 2-D cell for point spatial finite difference scheme

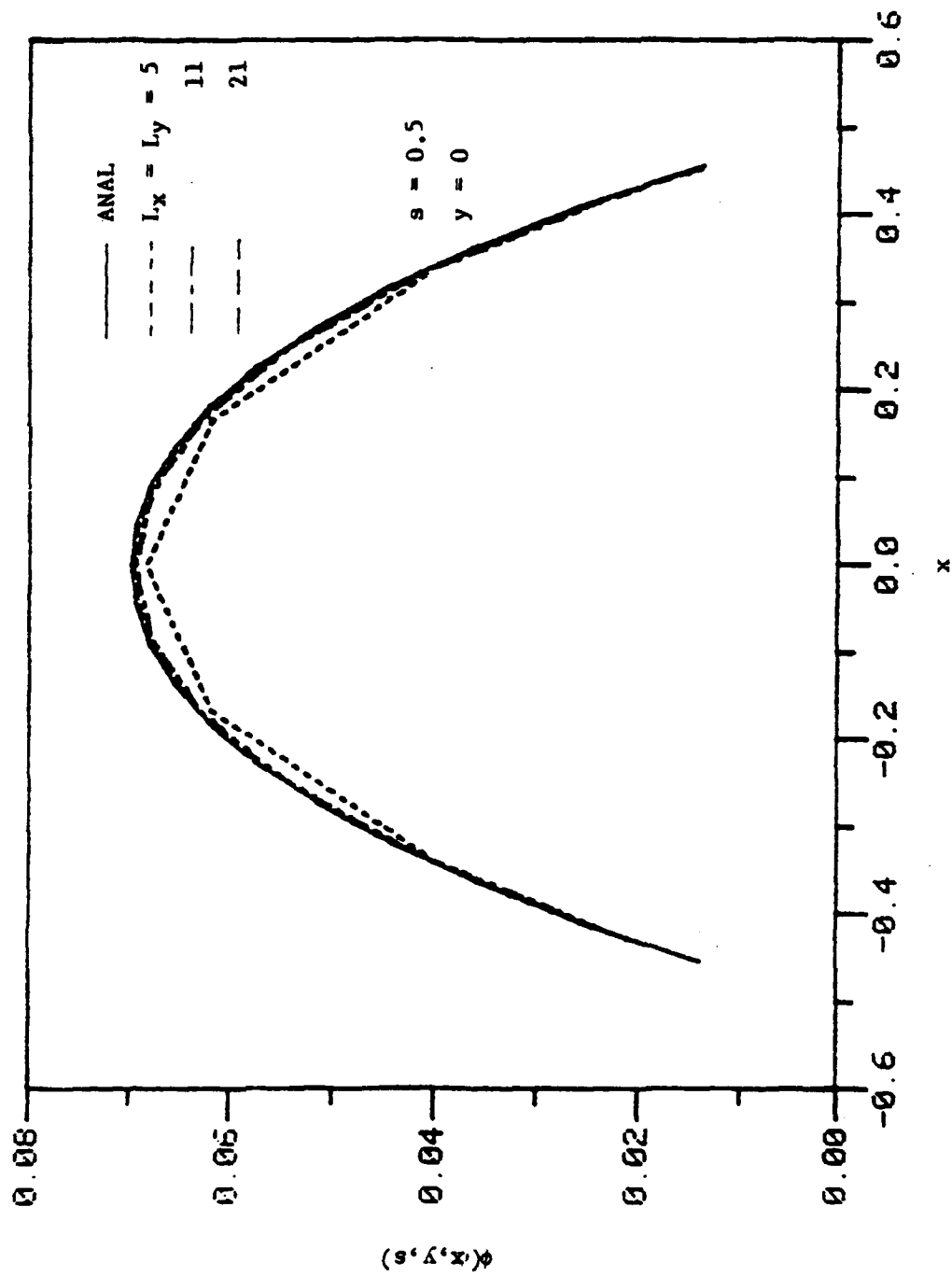


Fig. 18a Comparison with 2-D benchmark: $\Delta x, \Delta y$ sensitivity-ADI

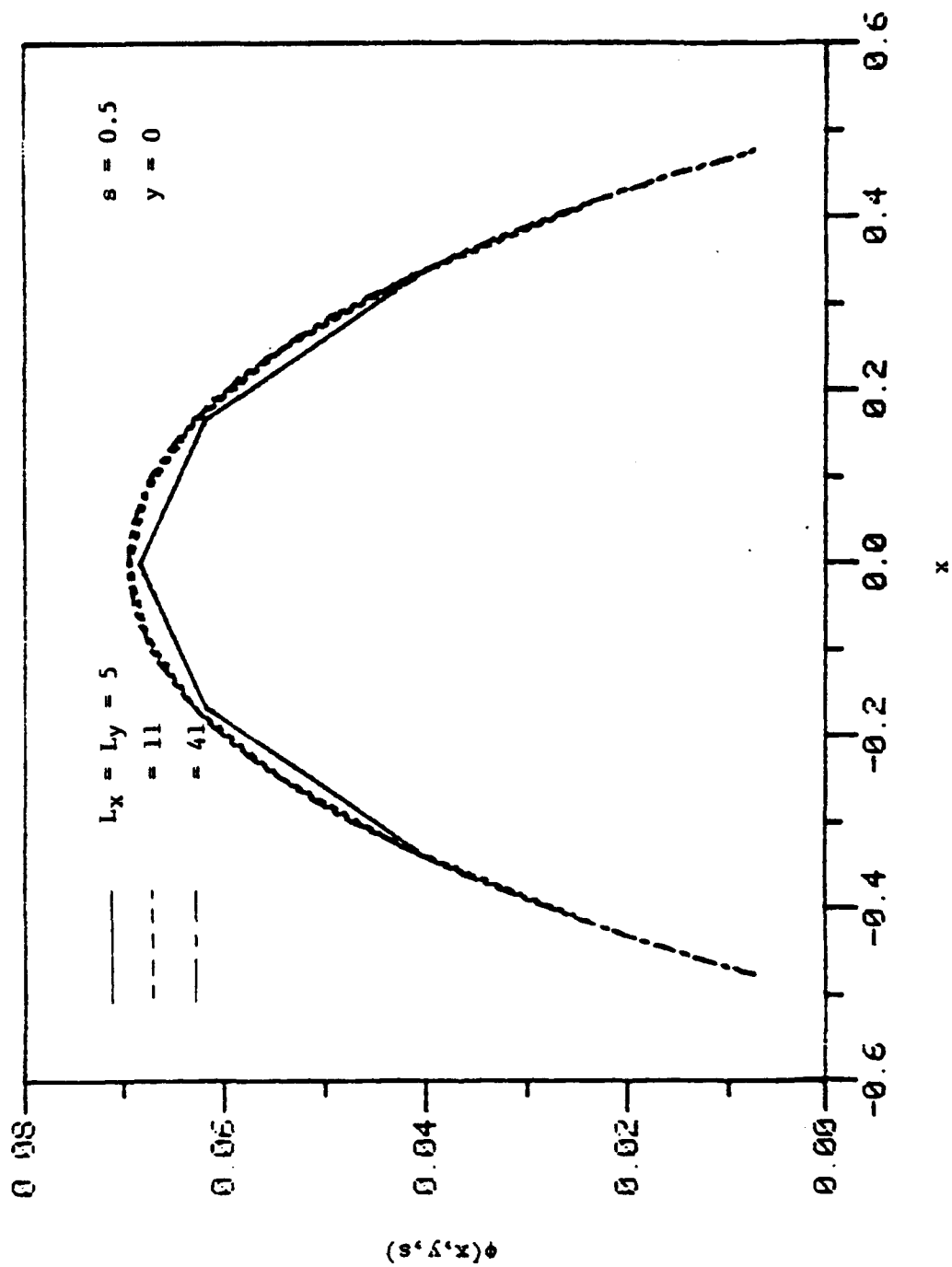


Fig. 18b $\Delta x, \Delta y$ sensitivity - LJ

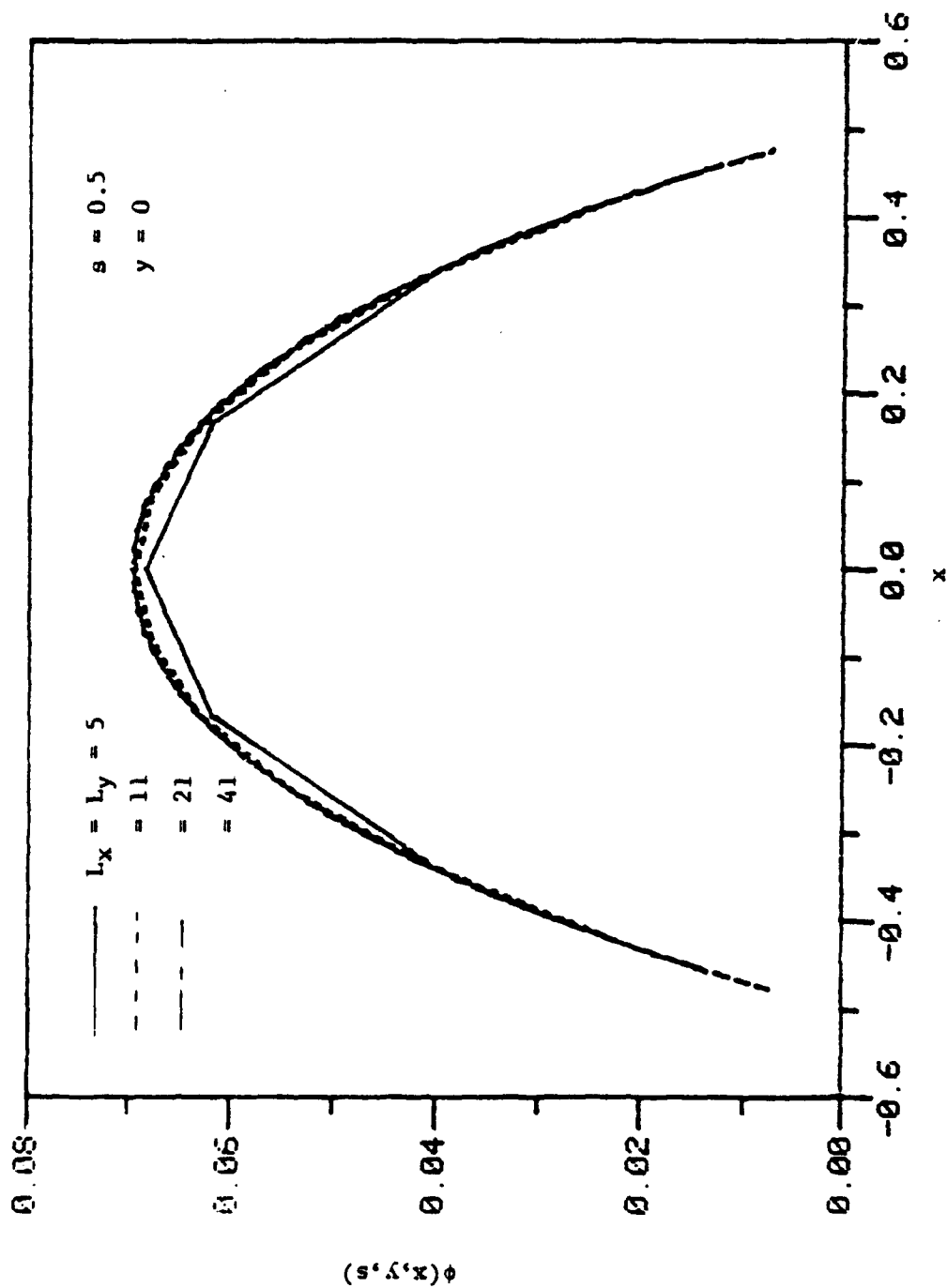


Fig. 18c $\Delta x, \Delta y$ sensitivity - SQR

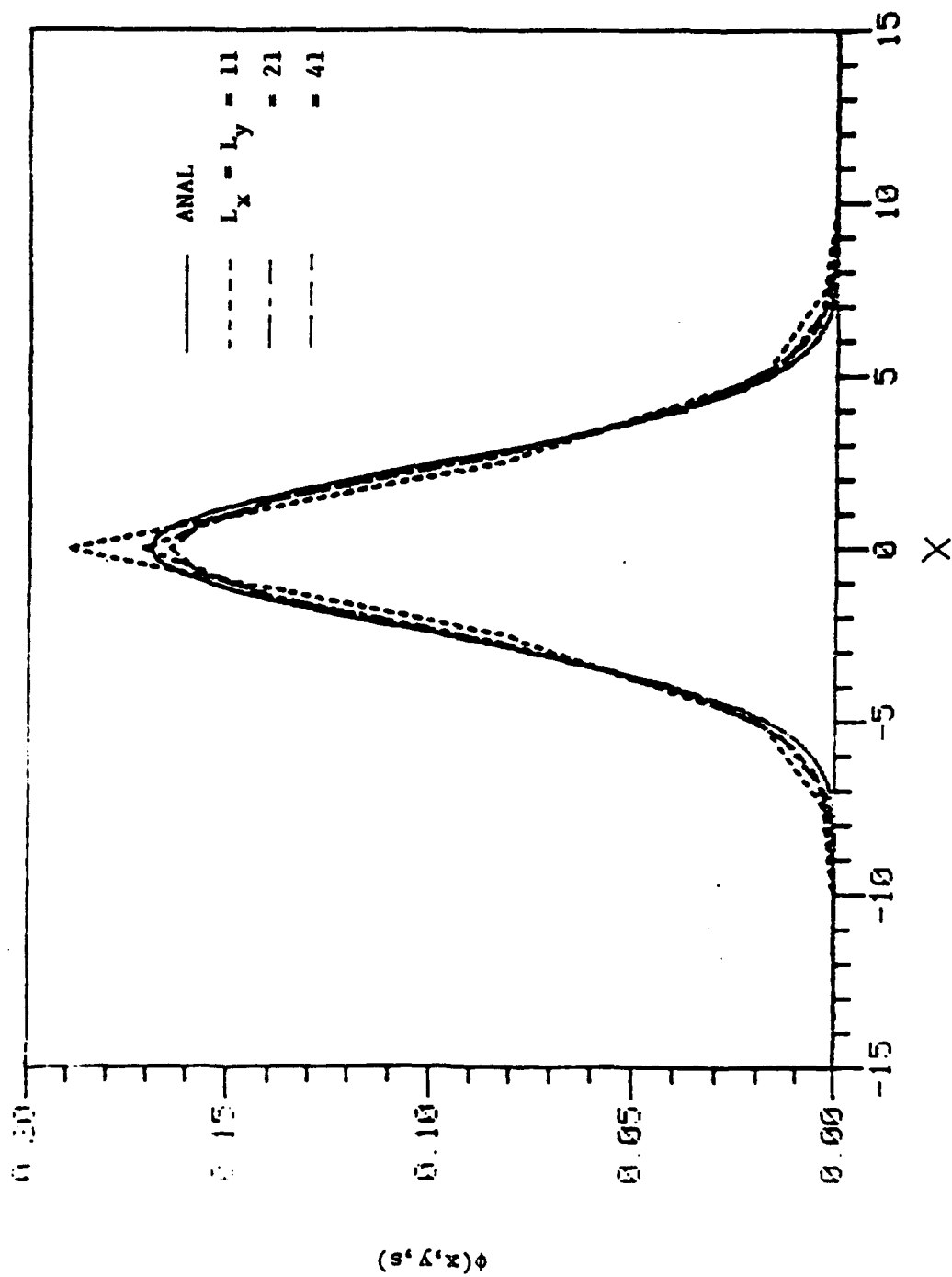


Fig. 19 2-D comparison of diffusion/transport coupling with transport theory

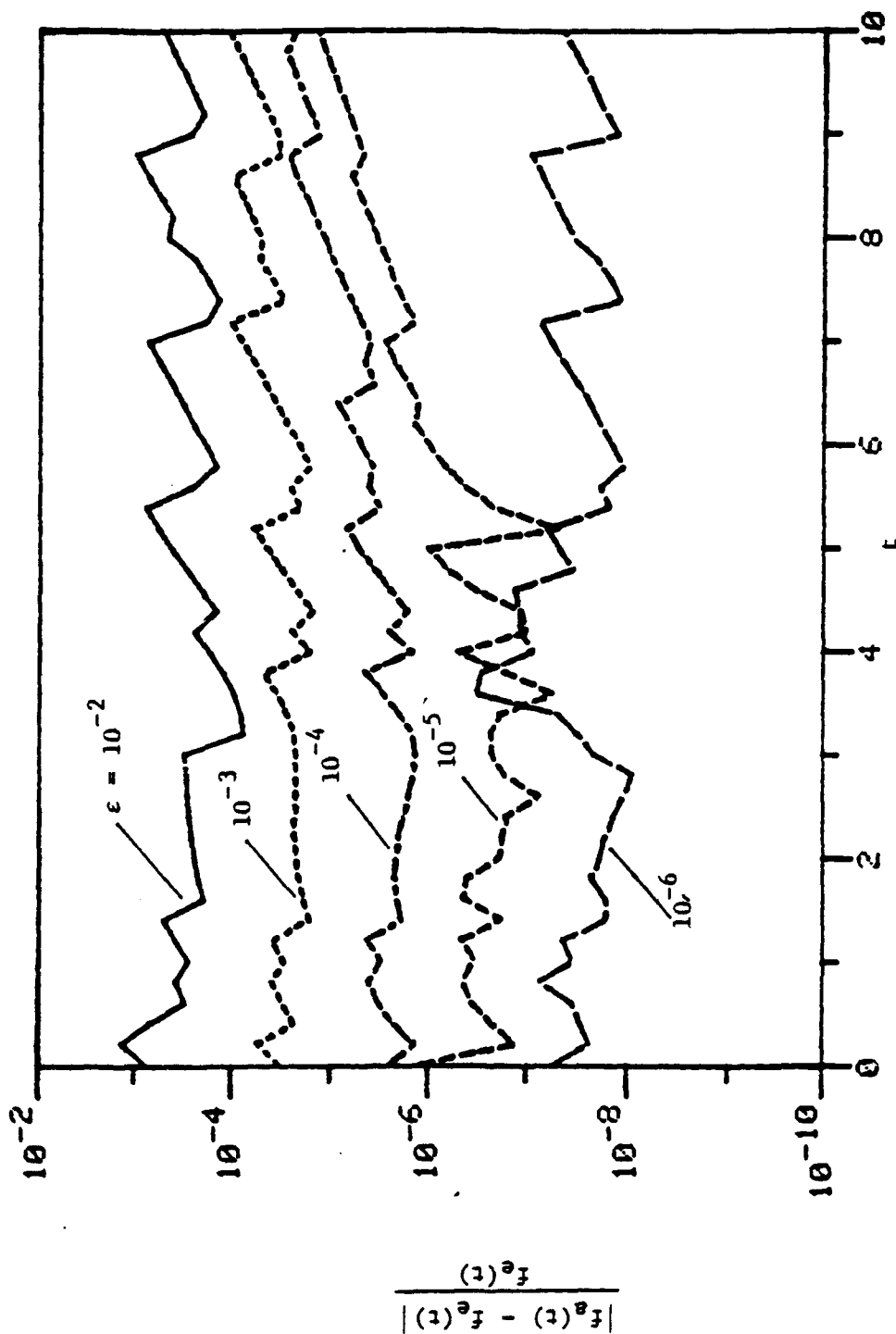


Fig. 20 Variation of ϵ : $\tilde{f}(s) = 1/(s+1)$, $f_e(t) = e^{-t}$

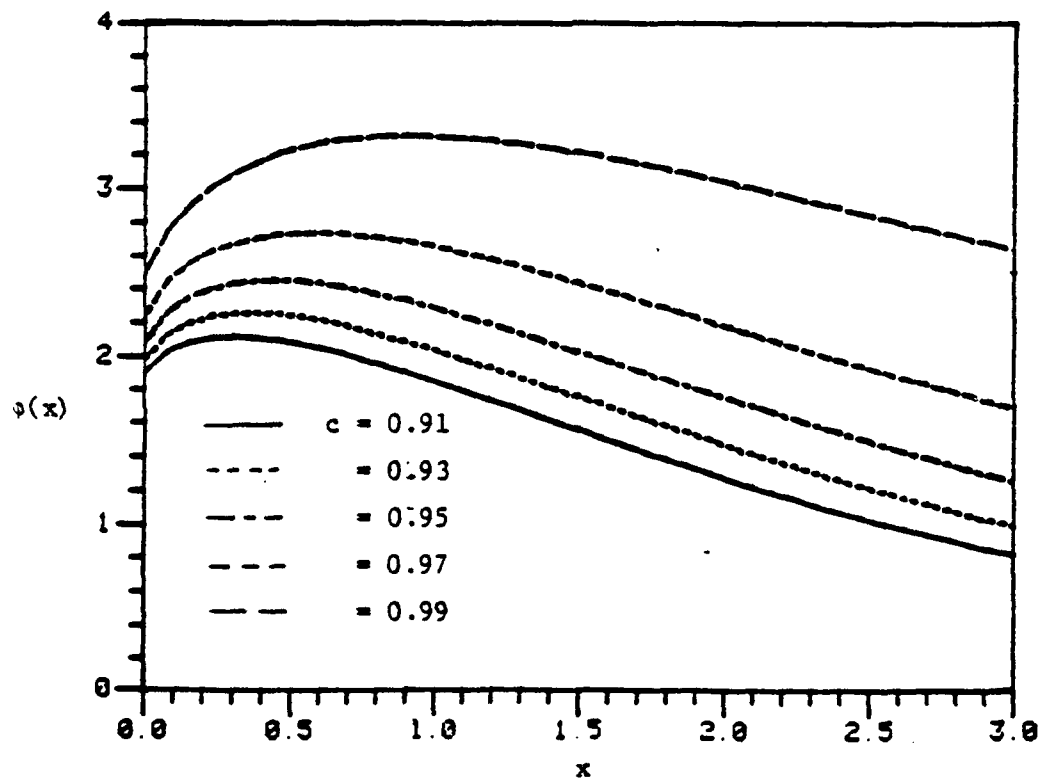
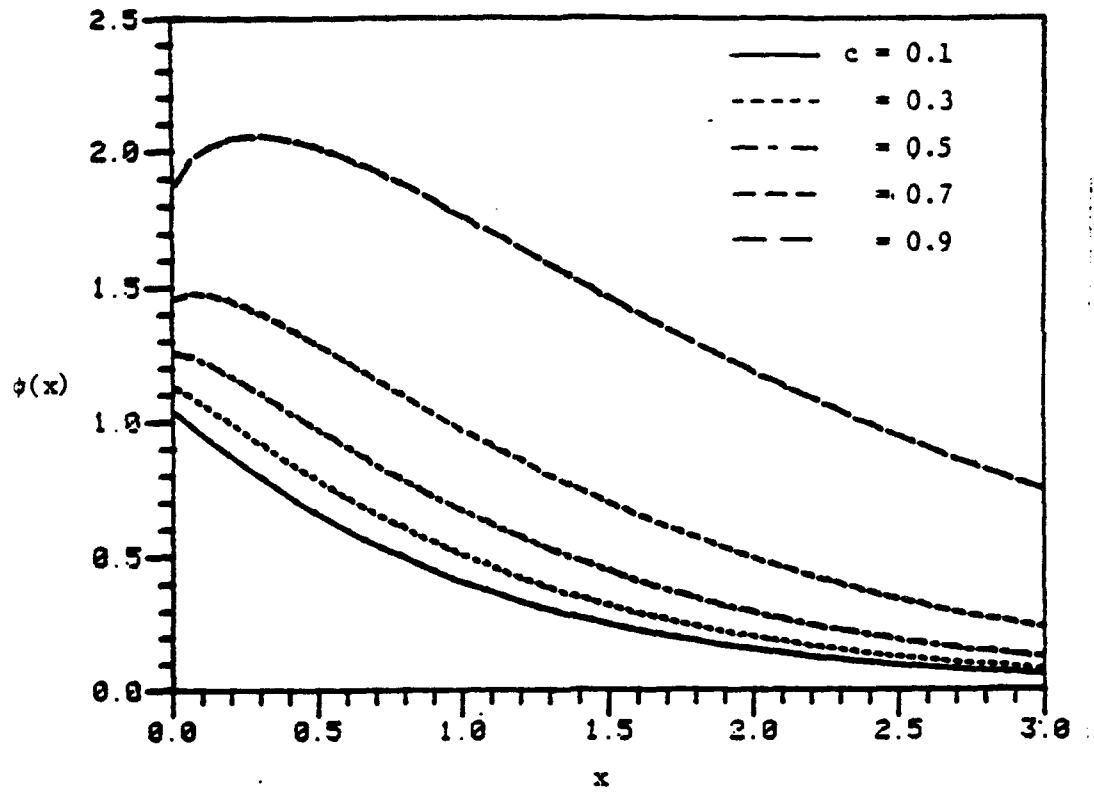


Fig. 21a Variation of c : Beam Source ($u_0 = 1$)

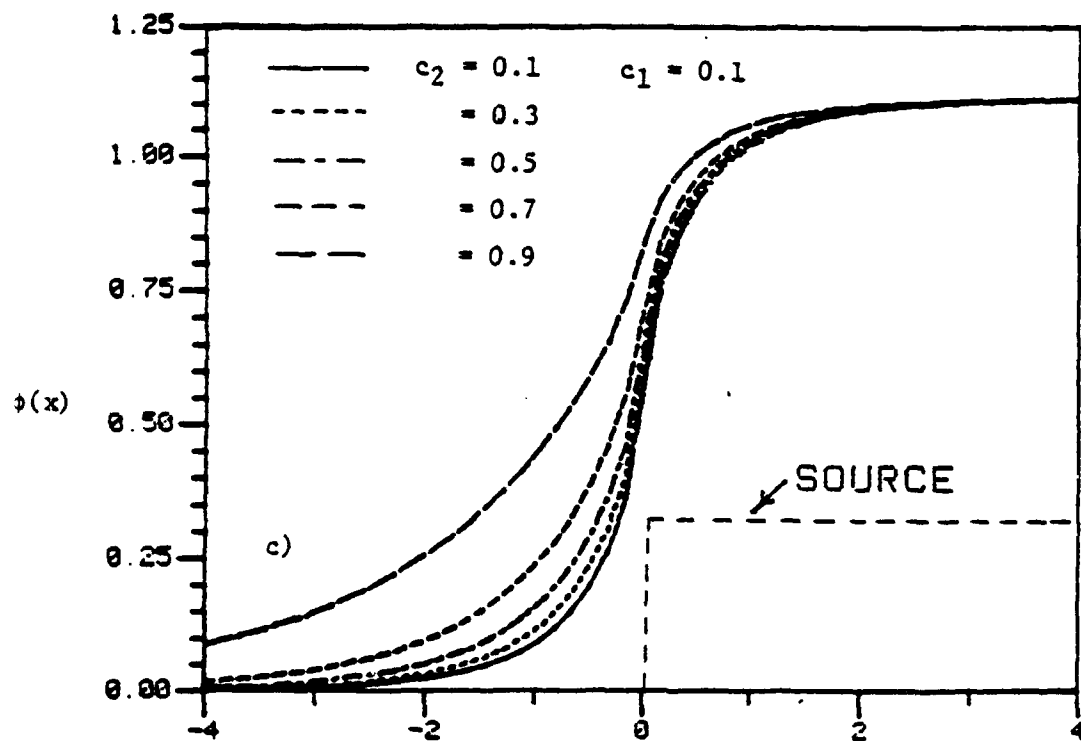
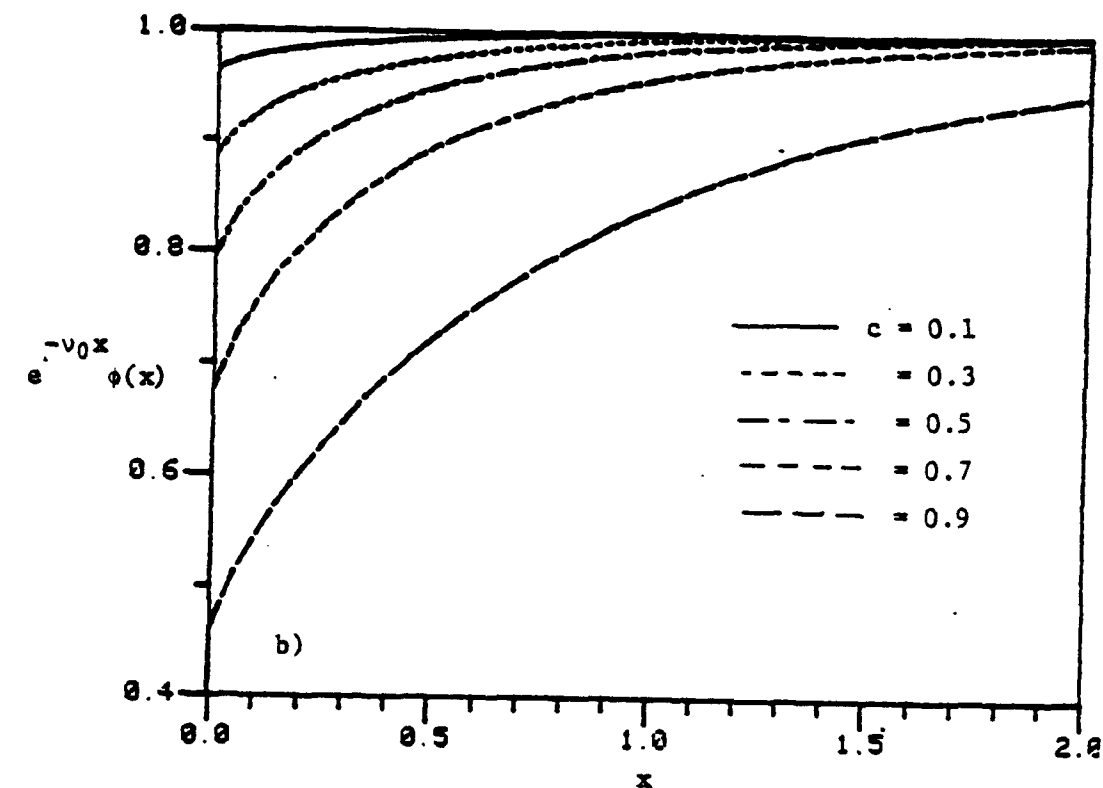


Fig. 21 b) single half space Milne
Problem c) 2 half-space Milne problem with source